

Magma transport along structure boundary in the upper crust: Insight from Broadband Magnetotelluric surveys in Unzen volcano

アグニス, トリアハディニ

<https://hdl.handle.net/2324/4495998>

出版情報 : Kyushu University, 2021, 博士 (理学), 課程博士
バージョン :
権利関係 :

Doctoral Thesis

**Magma transport along structure boundary in the upper crust: Insight from
broadband magnetotelluric surveys in Unzen volcano**

Agnis Triahadini

Department of Earth and Planetary Sciences
Graduate School of Science, Kyushu University

Abstract

Unzen volcano, located in Shimabara Peninsula, Nagasaki, Japan, is an active volcano that has been monitored intensively since before the most recent eruption in 1990-1995. Previous studies on sub-volcanic earthquakes and surface deformation have revealed that magma was transported obliquely from a magma reservoir located in beneath Tachibana bay, to the west of Shimabara Peninsula. Aiming to investigate crustal structure related to the magma migration, I conducted broad-band magnetotelluric (MT) surveys at 99 sites around the Shimabara Peninsula. A 3-D resistivity model constructed from MT data shows a broad zone of high resistivity beneath Shimabara Peninsula and zones of low resistivity to the west and east the peninsula. Unexpectedly, the high resistivity zone at 3 km to 15 km depth spatially correlates with the low-velocity zone (Miyano et al., submitted). Assuming that the melt is stored in a network of pores with good connectivity, a quantitative analysis indicates the high resistivity zone contains $< 5\%$ melt. Thus, the high-resistivity and low-velocity zone is inferred to be a highly crystallized mush zone that contains $< 5\%$ melt with low permeability. The hypocenters and pressure sources of the 1990-1995 eruption are distributed along the boundary between the high-resistivity and the low-resistivity zone located in the west of the peninsula. Thus, I concluded that the magma migrated along a structure boundary where the permeability is relatively high. Previous studies have suggested that eruptible magma is usually transported vertically upward through the center of the mush zone, whereas the present results reveal that magma can be transported along the upper boundary of a highly crystallized mush zone.

Keywords: magnetotelluric, high resistivity zone, Unzen volcano, highly crystallized mush zone, magma transport

CONTENTS

CHAPTER I: INTRODUCTION

1.1. Background of the Study	1
1.2. Magmatic System	
1.2.1. Magma definition	4
1.2.2. Magma chamber evolution	6
1.3. Geological Framework of Unzen Volcano	8
1.4. Magmatic System of Unzen volcano Inferred from Geophysical Survey	10
1.5. Previous Electromagnetic Surveys in Unzen Volcano	13

CHAPTER II: BASIC MAGNETOTELLURIC METHOD

2.1. Electric Conduction of Earth	18
2.2. Magnetotelluric Method	19
2.3. Geomagnetic Transfer Function	26
2.4. Phase Tensor	27
2.5. Magnetotelluric surveys for Active Volcanoes	29

CHAPTER III: MAGNETOTELLURIC SURVEY AND DATA MODELLING

3.1. Magnetotelluric Survey Layout	31
3.2. Broadband Magnetotelluric Observation in Shimabara Peninsula	32
3.3. Data Analysis	34
3.4 Three-Dimensional Inversion	34

CHAPTER IV: RESULT

CHAPTER V: DISCUSSION

5.1. High Resistivity Zone R1	45
5.2. Low Resistivity Zone in Shallow Level	52
5.2.1C1 and C2	53

CHAPTER VI: CONCLUSION

ACKNOWLEDGEMENT

REFERENCES

SUPPLEMENTARY MATERIAL

CHAPTER I

INTRODUCTION

1.1. Background of the Study

Unzen volcano is one of the active volcanoes located in Shimabara Peninsula, Japan, that erupted in 1990-1995 after 198 years of dormancy. During the eruption, lava domes were generated at the summit that was substantially collapsed, causing pyroclastic flows. Pyroclastic flows rolled down to Shimabara city and killed 43 people. In total, 0.2 km³ DRE materials were ejected during the eruption. The remaining lava dome emerges in the summit and is called Heisei-shinzan, which becomes the highest summit of the Unzen volcano (Nakada et al., 1999).

Unzen volcano attracts numerous researchers to study many aspects of this volcano, including the magmatic system. Petrological studies show the pieces of evidence of magma mixing between high-temperature low crystallinity andesitic magma with low temperature crystal-rich dacitic magma (e.g., Sugimoto et al., 2005; Nishimura et al., 2005; Botcharnikov et al., 2008). According to the seismicity and the deformation observations, the magma fed the 1990-1995 eruption migrated from beneath Tachibana bay in the west of Shimabara Peninsula. Before the eruption, the earthquakes initiated 15 km depth beneath Tachibana Bay 10 km west of Unzen volcano, while they markedly shifted eastward, approaching the summit before the first eruption in November 1990 (Figure 1.2). GPS and leveling monitoring detected pressure sources around 6 km west of the summit and beneath Tachibana bay. The pressure source locations coincided with the bottom boundary of the hypocenters (Umakoshi et al., 2001; Kohno et al., 2008). The observations during the 1990-1995 eruption indicated the western offset magma supplying system of Unzen volcano. Seismic tomography using local earthquakes attempted to image the magma

reservoir beneath Unzen volcano and its relationship with the last eruption (Miyano et al., submitted). The velocity model shows a broad low P-wave velocity (V_p) anomaly beneath Shimabara Peninsula but not beneath Tachibana bay. The pressure sources and earthquakes are located at the top of the low V_p zone. Therefore, Miyano et al. (submitted) suggested that the magma associated with the 1990-1995 eruptions migrated obliquely upward along the top of the low- V_p anomaly. A highly crystallized mush zone was considered to be the nature of the low- V_p anomaly. However, there was no low- V_p , low- V_s and High V_p/V_s beneath Tachibana bay at the depth of inferred magma chamber from the pressure source.

From geological and petrological perspectives, it is proposed that crystal mush zones dominate beneath a volcano. Crystal mush zones is a partially molten rock where crystals form a continuous network. The melt-rich regions/magma chambers occupy the center of vertically extensive crystal mush zones (Figure 1.1). The magma becomes more evolved in composition by decreasing depth, such as the upper crust. This system is known as the trans-crustal magmatic system (Cashman et al., 2017). When the crystal fraction in magma is between 0 and 50 %, the magma can flow. The growing crystals percentage will cause the formation of a rigid frame, and the melt cannot flow anymore (Bachman and Bergantz, 2008). The structure control, such as faults or crustal structure, can control the movement of magma and storage location (Edmonds et al., 2019; Sparks et al., 2019).

There is growing geophysical evidence to show small amounts of partial melt and crystal mush zone beneath active volcanoes. Magnetotelluric studies revealed sub-vertical low resistivity zones right beneath the volcanoes or few kilometers away from the main edifice that was associated with partial melt or magmatic fluids (e.g., Aizawa et al., 2014; Hill et al., 2015; Hata et al., 2016; Samrock et al., 2018; Cordell et al., 2018; Matsushima et al., 2020). Meanwhile, seismic

tomography conducted in other volcanoes also showed low-velocity zone that contains only a few percent melt fractions (e.g., Kukarina et al., 2017; Flinders and Shen, 2017; Yukutake et al., 2021). According to magnetotelluric results and other geophysical evidence of the Cascades magmatic arc, where Mt. Saint Helens is located, the inherited structures such as crustal faults and pluton control the orientation of magmatism and the ascent of magma from the lower crustal mush zone (Bedrosian et al., 2018). In another example, the magma does not have to move vertically, such as in Unzen volcano and Sakurajima and Sinabung (Hotta et al., 2016; 2019). Hence, the crustal structure could play important roles in the magma migration.

In the light of the previous geophysical observation of Unzen volcano and the previous studies that suggest structural control on the magma movement, I investigate the possibility of the structural controls on the magma migration of the 1990-1995 eruption. In this study, I deployed broadband magnetotelluric (MT) surveys in Unzen volcano and Shimabara Peninsula. The MT method is greatly capable of imaging low resistivity zones beneath volcanoes that are related to hydrothermal alteration/clay cap, magmatic fluids, and partial melt (e.g., Hill et al., 2015; Comeau et al., 2016; Cordell et al., 2018; Samrock et al., 2018; Matsushima et al., 2020; Gresse et al., 2021). Although the MT surveys have been conducted on the Shimabara Peninsula (Kagiyama et al., 1999; Srigutomo et al., 2008; Komori et al., 2013; Triahadini et al., 2019; Hashimoto et al., 2020), these works argue the shallow level of the volcano and do not focus on the deep structure that is related to the possible magma ascent route of the 1990-1995 eruption.

In order to interpret the estimated volcano structure, a combination of several geophysical data is valuable. Recent studies that compare electrical resistivity structure and seismic velocity structures have shown that the locations of the low-resistivity and low-velocity anomalies are sometimes not identical but shifted (e.g., Cordell et al., 2020; Bowles - Martinez et al., 2020). In

this study, I will show apparent discrepancies between high-resistivity and low-velocity anomalies beneath Unzen volcano from high-resolution data that previously has not been imaged beneath other volcanoes. By combining the high-resolution geophysical studies of Unzen volcano, I will suggest a new idea for the magma supplying system in the upper crust. The new insight from this study explains the oblique magma movement beneath Unzen volcano.

1.2. Magmatic System

1.2.1. Magma definition

According to Schminke (2004), magma is molten material composed by (Silicon (Si)) which is, apart from oxygen (O), the primary component of most minerals and rocks in the Earth's crust and mantle. Partial melting in the Earth's mantle and or in the lower crust in much smaller percentage are responsible in magma generation. The existence of solid particles (crystals) controls the magma behaviors in the reservoir. Magma which has 50 % of crystals or less, is relatively mobile and more eruptible. Meanwhile, as magma starts to solidify, it increases the amount or percentage of suspended crystals, says reaching 50-60% or more. Under this condition, the crystals start to form interconnected solid frame and can be called crystal mush zone. The relative viscosity of magma is significantly increased, then caused the magma to be immobile. Few percentage of melts are developed and distributed thoroughly at the interconnected crystal frame (Bachman and Bergantz, 2008). Magma chamber and mushes together form magma reservoir. The melt-rich regions/magma chambers occupy in the center of the vertically extensive crystal mush zone, and the magma becomes more evolved in composition by decreasing depth, such as upper crust. This system is known as trans-crustal magmatic system (Figure. 1.1) (Cashman et al., 2017).

The magma migration can be controlled by tectonic settings. It is transported to surface through brittle crust, planes of weakness existed in the host rock (e.g. faults) or along hydrofractures due to internal fluid pressure. Whether the melt is maintained at melt-rich phase or close to solidus, it is influenced by magma composition, input rates, local stress and heat transfer to the surroundings. Interestingly, most eruptions are fed from magma chambers at pressures of 1000-3000 bars (4-10 km depth) (Sparks et al., 2019; Edmonds et al., 2018).

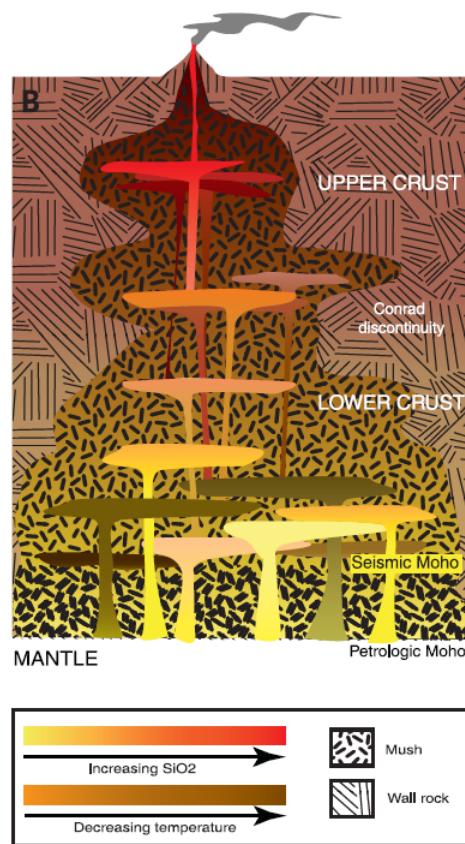


Figure 1.1. Transcrustal magmatic system, where melt processing in the deep crust produces melts that are transferred to mid- and finally upper crustal levels (Cashman et al., 2017).

On the broader scale, a magma plumbing system consists of interconnected magma conduits, whether vertical or inclined dyke, to connect magma from the source to surface; sills; and

reservoirs, which acts to store magma as it evolves into a crystal mush, ultimately fed from the partial melt at deeper zone (Magee et al., 2018). In the shallow plumbing system, several kilometers below volcanoes (upper crust), the plumbing system can go from a simple dyke complex or made of tens to thousands of parallel vertical dykes that link the magma chamber to the uppermost volcano conduit; or possibly can form a very complex intrusive plexus made of dykes, sills and inclined sheets, which make up the plumbing system of volcanoes (Tibaldi et al., 2015). Shallow large magma chambers are now considered ephemeral components of the magmatic system, associated with episodes of relatively high magma transfer from the hot zone into the crust (Blundy et al., 2021). Thus, the melt-rich, poor crystals, eruptible magma could be a short-lived or isolated body somewhere in smaller area in the crust, overshadowed by the more massive plumbing system (Figure 1.1). From incremental injection of new melt batches from deeper reservoirs, they accumulate as thin lenses and stack to build larger volume of magma plumbing system.

1.2.2. Magma chamber evolution

Bachmann and Bergantz (2008) explained microscale process that happens in a magma chamber. Magma is a complex, multicomponent, multiphase mixture. When thermodynamic conditions (eq. temperature or pressure) are changed, the different chemical components are redistributed into new phases (crystals, liquids, gases). Silicon and water form liquid portion of magma and are separated from higher density and less Si but rich of crystals. The upper part of the chamber is enriched by Si and H₂O which are brought by the ascended liquid portion of magma. The dense solid particles remain on the floor of the chamber. When stored magma contains < 45 vol. % crystals, convection currents stir the chamber, crystals are homogeneously distributed. However, when the crystals fraction > 65 vol%, crystal-liquid separation of crystals is driven by

compaction causing extremely slow process. Thus, the dacitic mush bodies can survive in the upper crust for > 100000 years due to limitation of migration distance and slow crystal-liquid separation.

The necessary condition for magma to cause eruption is pressurization of the chamber above critical value, allowing dike propagation in wall rocks. External triggers that contribute in the eruption is caused by tectonic stresses on the magma chamber. The more frequent mechanism can be important to drive eruption. Internal overpressurization is also a common driving force for eruption. Overpressurization is caused by saturation of the silicate liquid in gas and formation of bubbles or recharge by new injected magma. New magma batches are constantly generated in the mantle or deep crust. During ascent, they can encounter different compositional reservoirs and re-heat the intruded layer. It can result in some partial remelting of the crystal framework. The mush is turned to be liquidly, expand its volume and causing pressurization to some threshold rate that can cause failure of wall rocks. Then, the eruption occurs.

According to Edmonds et al (2018), the water content of melt exerts an important control on the architecture of magmatic systems. In water rich systems, magma injection will develop vertically extensive mush ultra-solidus reservoirs with compressible gas-rich caps and upper crustal lenses. Gas-rich region in arc volcanoes may form liquid lenses or present inside the mush. The gas may also trigger instabilities in the magmatic system, cause local mixing and even ignite eruption. Models of magma emplacement into mush show that complex layering and instabilities possibly occur on crustal scale, owing to the thermal and mechanical effects of the intrusion partial melting, cooling, convection, mixing, degassing and crystal settling. In addition, the timescales of this magmatic processes allowed a prolonged storage (10^3 to 10^6 years) in the crust, followed by

rapid remobilization and ascent. The remobilization may take place from upper crust layer or deep sills, or event near the Moho.

Therefore, it is concluded that a magma reservoir is composed by crystals, melt and volatiles (fluids/gas). The recent views of magma chamber models beneath active volcano no longer favors the classic long-lived, high temperature, extensive melt-rich/highly eruptible magma. The eruptible magma may form lenses, stacked sills, dykes and are distributed somewhere in various depths inside an extensive plumbing system. Instead, the new paradigm argues that magmatism occurs throughout the crust, with melt-rich eruptible magma chambers are stacked at the upper part of a much larger heterogenic trans-crustal magmatic system (e.g., Cashman et al., 2017). Geophysical surveys are expected to detect an anomaly due to the presence of molten material beneath active volcanoes, which has some distinctive physical properties than the surrounding/host rock.

1.3. Geological Framework of Unzen Volcano

Unzen volcano is a lava dome complex located in Shimabara Peninsula, Nagasaki, Kyushu Island, Japan (Figure 1.2). The volcano grows at the center of North-South extensional Unzen graben, the western end of extensive Beppu Shimabara Graben. This tectonic framework caused several normal faults in the East-West direction, which dissects the older peaks of the Unzen volcano. In 1990-1995, the eruption took place around Mt Fugen lava dome and later formed the Heisei-shinzan lava dome. The subduction-related earthquakes are not found beneath the Unzen volcano (Hoshizumi et al., 1999).

Between 4 Ma and 2 Ma, small scales of basaltic volcanisms (Pre-Unzen) occurred in the southern part of the Shimabara Peninsula. Then, the volcanism migrated to the west and center of the peninsula 500 Ka ago, and the Unzen stage was begun. To the present time, the volcano

products occupy roughly 20 km x 25 km region. Lava domes, thick lava flows, pyroclastic deposits that have andesitic to dacitic characteristics compose the volcano. The deposited volcanic products over Shimabara Peninsula indicate an eastward growing trend in which the western region is older than the eastern region where the active domes exist. The eroded peaks in the western region are called Older Unzen, composed of mainly thick lava flows with the approximated erupted volume of 120 km³. Meanwhile, the Younger Unzen has dacitic characteristics mainly composed of lava domes with 8 km³ total volume. To the east of Fugendake- Heisei-shinzan, an isolated dome called Mayuyama emerges. According to carbon dating conducted by Ozeki et al. (2005), Mayuyama eruption age is 4.6 cal. ka and shortly after this eruption, summit lava dome of Fugendake was formed. From historical times to the present, three eruptions from Unzen's summit that were generally occurred separately by hundred years' dormancy. The historical eruption of Unzen happened in 1663 and 1792 that centered in Fugendake. During the 1792 eruption, the Mayuyama dome collapsed and generated a gigantic tsunami. The tsunami hit the coastal area opposite Shimabara and caused 15000 fatalities (Hoshizumi et al., 1999; Sugimoto et al., 2005).

Extensive results from laboratory analysis of Unzen volcanic rocks are available. It was suggested that the magmatism of Unzen is originated from the injection of ocean-island type basalt that evolved and produced the high-temperature low crystallinity andesitic magma (Sugimoto et al., 2005). Due to fractional crystallization and crustal assimilation, a low-temperature phenocryst-rich dacitic chamber with high water content was formed (Nishimura et al., 2005). The erupted materials (e.g., lava and pyroclastic flows) show the mixing between the andesitic and dacitic chamber (Nakada and Motomura, 1999; Botcharnikov et al., 2008). Sato et al. (2017) proposed that convection heated the base of silicic mush reservoir from underlain mafic magma resulting in a high temperature aphyric andesitic magma. The continuous supply of basalt magmas might exist

beneath Shimabara Peninsula throughout the eruptive history of the Shimabara Peninsula (Sugimoto et al., 2005). The storage condition for the two magma chambers showed that the andesitic magma resides in higher pressure and higher temperature and dacitic magma takes place in lower temperatures and lower pressure (Botcharnikov et al., 2008, Nishimura et al., 2005). The continuous injection from parental magma probably exists and resulted in the differentiation of the magma chamber composition.

1.4.Magma System of Unzen Volcano Inferred from Geophysical Surveys

One of the importance of volcano deformation monitoring (inflation and deflation) volcanic surface is to detect injection of new magma or closing of magma reservoir respectively. When the significant deformity pattern emerges, crises management to measure forthcoming eruption status can be released. Thus, the measurement data provide critical insight of the spatial and temporal development of active plumbing systems. In the analysis of deformation signal (spatial or temporal pattern, height change amplitude, etc), the source that causing the change will be traced down. For example, the location and dimension of the source will be modelled based on numerical method. Simply, the depth origin of the ejected magma during eruption can be explored through GPS data. Among the available numerical analysis, one of the extensively used to volcanic deformation, is Mogi model (Mogi et al 1958). An increase of pressure is assumed occur in a small size, spherical shape within an elastic half-space body. The depth source of the fluctuation then can be estimated. Despite it is widely adopted through the helpfulness revealing source location based, it offers simplified model of the deformation source. Basically data from geodetic survey informs a localized part from larger magma plumbing systems that undergoes significant changes and do not intensively describe the full extent and state of the intrusion network (Magge et al, 2018). The real complexity of Earth's structure is far to be assessed only by Mogi model.

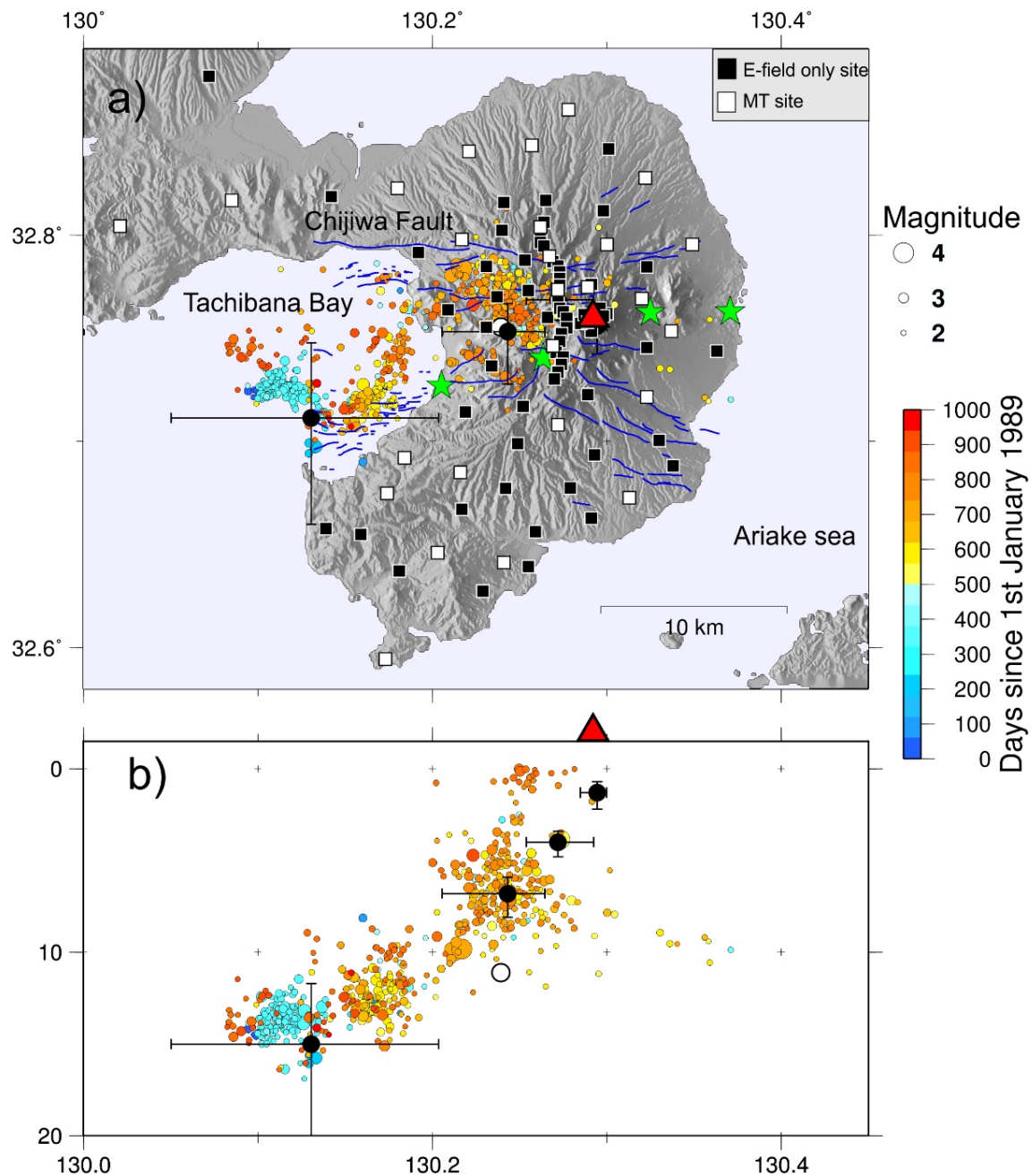


Figure 1.2. a) The MT sites distribution in Unzen volcano (red triangle), Shimabara Peninsula, Kyushu Island, Japan. b) Vertical view of pressure sources (Kohno et al., 2008) and seismicity (Umakoshi et al., 2001). Green star symbols indicate the hotspots located in the study area. Blue scattered lines represent the faults in Unzen Graben. Circles with corresponding colors show the hypocenter of 1990-1995 eruption (Umakoshi et al., 2001). Pressure sources are indicated by black circles (Kohno et al., 2008) with represented error bars and also white circle for single pressure source reported by Nishi (1999).

Here, the continual geodetic surveys around Unzen volcano and Shimabara area before and after eruption of 1991-1995 are listed. The surveys were repeatedly conducted to observe temporal change in the same routes, located along western coast of Shimabara peninsula and northern flank of Unzen. The GPS data were also obtained from same stations distributed over Shimabara area. Among the models proposed by Kohno et al (2008), four pressure sources were confirmed, namely A, B, C, D (from shallow to deep level, Figure 1.2). The authors used extensive data from before eruption until five years after eruption stopped. The most intensive deformed pressure sources were pressure source C which was located about 5-6 km west of Fugendake and pressure D which was located 15 km beneath Tachibana bay in western coast Shimabara Peninsula. Nishi et al (1999) inferred only a source, that the location is similar to C-source with deeper vertical position. All of pressure sources were topped by migrated seismicity hypocenters reported by Umakoshi et al (2001) (Figure 1.2). Thus the pressure sources were later proposed as magmatic zone since earthquake is likely to bypass molten body then isolated on the brittle layer. From the repeated measurement from 1986-2004, it was concluded that Shimabara peninsula receives continuous magma supply from the deep western side of the peninsula.

Recent seismic tomography using local earthquakes catalog exhibited a broad low P-wave velocity (V_p) zone beneath Shimabara peninsula (Miyano et al., in submission). The low V_p zone had a good resolution until depth < 16 km bsl but not for the S-wave velocity. At the depth level of low V_p zone, moderate low S-wave V_s zone was observed around < 5 km bsl and reduced > 6 km bsl. Earthquakes and pressure sources were distributed at the top of Low V_p zone. No Low V_p zone was detected at the depth level of magma reservoir beneath Tachibana bay although the resolution of that area was fair. The decrease of the moderate V_s to low V_s that accompanied low V_p led to fluid/melt rich in the region. So the result could not explain the existence of melt rich

region under Unzen. It was concluded that the low Vp zone represents highly crystallized mush zone beneath Shimabara Peninsula.

1.5. Previous Electromagnetic Studies in Unzen Volcano

Numerous electromagnetic surveys have been performed in Shimabara area. The surveys differ in terms of the sites distribution, targeted structures and the used frequency ranges (data acquisition techniques). Among those studies, only two studies (Triahadini et al., 2019; Hashimoto et al., 2020) that used broadband MT and 3-D modelling. The other studies used higher frequency ranges and 1-D modelling (Kagiyama et al., 1999; Srigutomo et al., 2008) and 2-D modelling (Komori et al., 2013). In the next paragraph, I summarize the available electromagnetic investigations in the vicinity of Unzen volcano.

First, Kagiyama et al (1999) reported the result from ULF, VLF-MT and ELF (frequency range: 30-300 Hz, 300 kHz-3kHz, 0.1 Hz-3 Hz respectively) investigations throughout Unzen volcano between 1991-1994. One dimensional model of each stations showed low resistivity layers beneath the sites, for example extremely low resistivity layer under Jigokuato-crater (before dome extrusion) at very shallow depth. Water saturated zone was the interpretation of the anomaly, while hydrothermal zone could be responsible for the anomaly under Jigukoato crater. The model also exhibited low resistivity layers at > 10km depth. The authors argued that magma could be located at this layer. However, due to limited frequency range and 1-D modelling made the low reliability for the deeper structure. The highlight of this study is that the interaction of volcanic gas and magma column with water rich layer caused explosive eruption of Unzen volcano in the initial eruptive period.

Srigutomo et al (2008) carried out Time Domain Electromagnetic (TDEM) surveys around Shimabara area during 2001 and 2002. TDEM observation relies on artificial electromagnetic

source injected to the ground. This method is effective for investigating structure in the area which have high artificial electromagnetic noise and performing ordinary EM method is difficult due to steep topography and stiff lava formation. 8 Hz, 32Hz and 128 Hz sampling rate of transient wave were used in the survey. The investigation aimed to image resistivity structure and assess magmatic volatile supply from deeper region to shallower level in Shimabara Peninsula. The pseudosection profiles from one dimensional resistivity models of each sites displayed the low resistivity anomaly that extended from west to east Shimabara Peninsula at approximately 300 m to 2 km below surface. At the top and beneath this anomaly, high resistivity layers were detected. The relatively low resistivity zones were detected adjacent to faults, such as Akamatsudani fault and Take fault. It was concluded that the low resistivity zone found in the shallow depth around Shimabara as water-saturated layer and hydrothermally altered rocks. The extremely low resistivity layer in several sites may indicate contribution of hot ionic gas or fluids (e.g. beneath Mayuyama). The contour conductance (product of integration of conductivity and depth) map outlined an elongated E-W high conductance that confirmed the E-W orientation of low resistivity anomaly. It was suggested that the release of volcanic gas through the fractures and eastward magma migration caused the E-W direction high-conductance to exist beneath Shimabara Peninsula that swarms in the vicinity of fractured zones arisen due to release of volcanic gas from magma.

Komori et al. (2013) conducted a north south two dimensional resistivity profile in the derived from eleven AMT and MT sites located in the summit area provides a high resolution resistivity structure under Unzen volcano (Mt. Fugen) and the correlation with the hydrothermal system. The AMT-MT survey used 1 Hz to 10kHz sampling frequency range. The result indicated an intermediate resistivity zone at few hundred meters below surface followed by lower resistivity zone around 1-2 km below sea level, with the lowest magnitude was less than $3\Omega\text{m}$ in certain part.

The low resistivity zone correlated with the decrease of resistivity values from 1000 Ωm to 10 Ωm derived from well logging data (USDP-4). The interpretation for the intermediate resistivity zone was the water/cold water saturated layer. Moreover, the very low 3 Ωm anomalies were suggested as low permeability clay acts as hydrothermal sealing zone, to maintain fluids circulation. The high temperature fluids were assumed to be maintained within deeper high resistivity zone. A pressure source detected > 1km beneath summit supports the shallowly-emplaced dykes that could maintain high temperature conditions. Because of limited frequency range used in the observation, the structure deeper than 1 km beneath sea level has generally low reliability. Moreover, the southern section has too sparse the distributed sites.

Broadband MT study along single profile line in N-S direction was conducted in the western flank, 2 km from Fugendake (Triahadini et al., 2019). The study aimed to determine the resistivity structure under Unzen graben and its relationship with the faults of the graben, magma and volatiles. In total, 27 MT stations were installed roughly every 300 meter along a 9 km line dissected the graben and EW trending faults in the vicinity area. The typical resistivity layers on volcanic area were resulted from 3D inversion. The moderate to low resistivity zone were located between upper part and lower part high resistive layers. The low resistivity zone was proposed as hydrothermal-fluid rich layer which also follows relatively more conductive near the faults area. Compared to all the previous works, the MT sites were closely space and the data was modelled by 3-D inversion by finer mesh which could provide a high resolution result.

Triahadini et al. (2019) showed that the significant low resistivity zone exists around Chijiwa Fault. This anomaly expanded 2 km horizontally to the south of the fault and 4 km vertically, and had resistivity value less than 10 Ωm . Due to lack of surface evidence, such as active geothermal manifestation in this area and discrepancies with the pressure sources and seismicity locations, so

the authors interpreted the low resistivity anomaly as fault conductive zone (FCZ) in which also acted as a pathway for fluids movement. FCZ can be resulted by brittle fracture creating interconnected pore where fluids may fill the space. Seismic reflection study conducted in the same profile line (Matsumoto et al., 2012) shows strong reflectors at the location of low resistivity anomaly. Thus, by also taking into account the strong reflectors and location of pressure sources, it was concluded that the low resistivity zone as network fractured generated by Chijiwa fault where magmatic volatiles from below pressure source were supplied into. The volatiles enhanced the conductivity and also reflector. Moreover, in the center of the survey line, the resistive body was found, called R1. They proposed this region as composed multi dykes that might act as magma pathway.

Hashimoto et al. (2020) conducted broadband MT surveys in Fugendake- Heisei shinzan area. Their goals were to estimate the mechanisms of implosive earthquakes occurred beneath the lava domes and the relationship with the resistivity structure. The total number of MT stations are 14. The result from 3-D inversion using fine mesh size in (100 meter horizontally and 50 meter vertically) showed a high resistivity layer beneath Fugendake and Heiseishinzan that extends from near surface to about sea level. This zone was interpreted as hydrothermal fluid sparse zone. Cold water or vapor might fill the pore space in this region. The authors speculated that the vapor filled voids may collapse and generate the implosive earthquake. The inversion model also indicated a low to moderate resistivity zone in the second layer, at approximately sea level to 2 km beneath sea level. Hydrothermal fluids and altered clay minerals were the possible explanation of the low resistivity zone.

To sum up, all of MT research imaged a low resistivity zone at 1-2 km depth in Shimabara Peninsula and Unzen. In general, the low resistivity zone in Shimabara peninsula highlighted the

contribution of hydrothermal system and water rich zone in inside fractured zone. Meanwhile, the near surface and deeper level high resistivity zone could be associated with water poor volcanic deposits and the basement rocks of Shimabara. However, there were limitation in the stations coverage and applied frequency range that lead to poor resolution for upper to mid-crustal structure where the magma is possibly emplaced.

CHAPTER II

BASIC MAGNETOTELLURIC METHOD

2.1. Electric conduction of the Earth

The Earth is composed of various types of rocks and materials that have various physical properties. Geophysical methods attempt to obtain physical properties of the Earth, for example, using Earth's electrical resistivity. The electrical resistivity (Ohm-meter, Ωm) is the bulk property of a material that shows the ability of material to allow electric currents flow through it. The reciprocal term of resistivity is called conductivity (Siemens/meter).

On the Earth, conduction of the materials arises via some mechanisms of charge carriers. The conduction mechanisms are electronic conduction (in metals), ionic conduction (in fluids and melts), or electron vacancies (in semiconductor materials). The materials can act as a conductor if they contain a large number of high mobility carriers. The semiconductors can carry currents by a smaller number of the mobile electrons while the insulator materials have ionic bonding, so the electrons cannot move freely. The resistivity of Earth rocks and minerals has a wide range of magnitudes compared to other physical properties, such as density or elastic wave velocity. The resistivity of Earth materials spans from $10^{-5} \Omega\text{m}$ for metallic materials (e.g., pyrrhotite) to $10^7 \Omega\text{m}$ for dry, close-grained rocks such as gabbro. The rocks and minerals are generally grouped based on their resistivity/conductivity into three categories (Telford et al., 1990; Simpson and Bahr, 2005; Chave and Jones, 2012):

- a. Conductors: $10^{-8} \Omega\text{m} - \sim 1 \Omega\text{m}$ (e.g., metals, graphite, sulfide)
- b. Semiconductors: $1 \Omega\text{m} - 10^7 \Omega\text{m}$ (e.g., mantle olivine).
- c. Insulators : $>10^7 \Omega\text{m}$ (e.g. dry basalt)

Most of the rocks on Earth have semiconductor properties. Temperature, pressure amount of fluids, salinity, and porosity control resistivity. Electromagnetic sounding methods images bulk resistivity (mixture of multiple phases) of the rock, which indicates that the rock holds some amount of various types of minerals and or fluids within the rock matrix. A few percentages of conductive minerals and or fluids within an interconnected porosity network will significantly decrease the bulk resistivity. However, if the conductive phase is stored in isolated pores, it will not reduce the bulk resistivity significantly. Therefore, the bulk resistivity is influenced primarily by the connectivity and the conductive phase inside the host rock (e.g., Waff, 1974; Glover et al., 2000).

2.2. Magnetotelluric method

The magnetotelluric method is a geophysical method that utilizes natural time-varying electromagnetic fields (E-field and B-field) to image the resistivity structure of the Earth. The MT method has advantage of detecting low resistivity zones from the near-surface down to the upper mantle. The electromagnetic wave is generated from two kinds of sources that are located outside of the Earth. It is assumed that the EM wave propagates to the Earth as a plane wave and has a variable frequency ranging from 10^{-5} to 10^{-4} Hz. The first source of EM wave is from the worldwide lightning activity, which will produce > 1 Hz EM signals. The second EM source comes from solar wind activity that interacts with Earth's magnetosphere and will generate EM signals below 1 Hz. The EM wave travels to the Earth and induces the internal Earth's electromagnetic field. The EM wave follows plane waveguide that normally incident on the surface of the conductive Earth. The E-field and B-field are mutually perpendicular to each other. MT sensors deployed on the ground will record the orthogonal E-field and B-field variations, and the recorded data contains information of magnitude and phase of the E-field and B-field (Tikhonov, 1950;

Cagniard, 1953). The full explanation of MT theory can be found in the published textbooks (e.g., Telford et al., 1990; Simpson and Bahr, 2005)

To understand the propagation of the EM wave, the basic explanation of relationship between E-field and B-field follows Maxwell's equations:

$$\nabla \times \mathbf{E} = -\frac{\partial \mathbf{B}}{\partial t} \quad (2.1)$$

$$\nabla \times \mathbf{H} = \mathbf{j}_f + \frac{\partial \mathbf{D}}{\partial t} \quad (2.2)$$

$$\nabla \cdot \mathbf{B} = 0 \quad (2.3)$$

$$\nabla \cdot \mathbf{D} = \eta_f \quad (2.4)$$

Where \mathbf{E} is the electric field (in V/m), \mathbf{B} is magnetic induction (in Tesla), \mathbf{H} is magnetic field (in A/m), \mathbf{D} is electric displacement in (C/m²), \mathbf{j}_f is the electric current density owing to free charges (in A/m²), and η_f is the electric charge density owing to free charges (C/m³)

Faraday's Law (2.1) shows that the time-varying magnetic field induces corresponding changes in the electric field flowing in a closed loop. Ampere's Law (2.2) shows that any electric field in the closed-loop will have a corresponding magnetic field that the magnitude is proportional to the total current flow.

Following a linear isotropic medium relationship and together with Ohm's law

$$\mathbf{B} = \mu \mathbf{H} \quad (2.5)$$

$$\mathbf{D} = \epsilon \mathbf{E} \quad (2.6)$$

$$\mathbf{j} = \sigma \mathbf{E} \quad (2.7)$$

Following the assumption of MT method, in regions of finite conductivity, charges do not accumulate to any extent during current flow. The EM wave is not attenuated when propagating through free space/air, but will be attenuated when traveling in a conductive medium. The frequencies of the used waves are also low. Thus, the time varying displacement currents are negligible compared with time-varying conduction currents. The variations of electrical permittivity ϵ and magnetic permeability μ of rocks are also insignificant compared with variations in bulk rock conductivities, then Maxwell's equations can be expressed in these forms

$$\nabla \times \mathbf{E} = -\frac{\partial \mathbf{B}}{\partial t} \quad (2.8)$$

$$\nabla \times \mathbf{B} = \mu_0 \sigma \mathbf{E} \quad (2.9)$$

$$\nabla \cdot \mathbf{B} = 0 \quad (2.10)$$

$$\nabla \cdot \mathbf{E} = \eta_f / \epsilon \quad (2.11)$$

With electrical permittivity and magnetic permeability in free space are $\epsilon_0 = 8.85 \times 10^{-12} \text{ Fm}^{-1}$ $\mu_0 = 1.2566 \times 10^{-6} \text{ Hm}^{-1}$.

Using the vector identity $\nabla \cdot \nabla \times \mathbf{A} = 0$, for time-varying fields will be

$$\nabla \cdot \nabla \times \mathbf{E} = -\nabla \cdot \frac{\partial \mathbf{B}}{\partial t} = -\frac{\partial}{\partial t} (\nabla \cdot \mathbf{B}) = 0 \quad (2.12)$$

That explains equation (2.3) $\nabla \cdot \mathbf{B} = 0$

Equation (2.3) indicates there is no free magnetic charges (monopole) exist. Similarly applied the vector identity to equation (2.2),

$$\nabla \cdot \mathbf{j} + \nabla \cdot \frac{\partial \mathbf{D}}{\partial t} = \nabla \cdot \mathbf{j} + \frac{\partial}{\partial t} (\nabla \cdot \mathbf{D}) = 0 \quad (2.13)$$

The divergence of current density is equivalent to the rate of accumulation of charge density, Q

$$\nabla \cdot \mathbf{j} = -\frac{\partial}{\partial t} (\nabla \cdot \mathbf{D}) = -\frac{\partial Q}{\partial t} \quad (2.14)$$

$$\text{Hence} \quad \nabla \cdot \mathbf{D} = Q \quad (2.14a)$$

Assuming that no current sources exist within the Earth and no charge accumulation

$$\nabla \cdot \mathbf{j} = \nabla \cdot (\sigma \mathbf{E}) = 0, \quad \nabla \cdot \mathbf{D} = \epsilon \epsilon_0 \nabla \cdot \mathbf{E} = 0 \quad (2.14b)$$

For the case of homogeneous half-space

$$\nabla \cdot (\sigma \mathbf{E}) = \sigma \nabla \cdot \mathbf{E} + \mathbf{E} \cdot \nabla \sigma = \sigma \nabla \cdot \mathbf{E}$$

However, for layered earth, there will be conductivity variation in the horizontal direction:

$$\mathbf{E} = (E_x, E_y, 0)$$

For a conductivity distribution that varies in the vertical direction and one horizontal electric fields:

$$\mathbf{E} = (E_x, 0, 0)$$

In the case that electric field perpendicular to a boundary, $\nabla \cdot \mathbf{E} \neq 0$, thus

$$\mathbf{E} = (0, E_y, 0)$$

For the case of the Earth, the time-varying external magnetic field induces an electric field (2.1), which in turn induces a secondary internal magnetic field (2.2). The curls of equations (2.1), equation (2.2) and assuming an Earth model with $\nabla \cdot \mathbf{E} = 0$, are

$$\nabla \times (\nabla \times \mathbf{E}) = \nabla (\nabla \cdot \mathbf{E}) - \nabla^2 \mathbf{E} = -\nabla \times \frac{\partial \mathbf{B}}{\partial t} = \mu_0 \sigma \frac{\partial \mathbf{E}}{\partial t} \quad (2.15)$$

In the plane wave, with a surface amplitude E_0 and the harmonic time dependence of the form $e^{-i\omega t}$, and assumption on the Earth model for which $\nabla \cdot \mathbf{E} = 0$, equation (2.15) can be rewritten as

$$\nabla^2 \mathbf{E} = i\omega\mu_0\sigma\mathbf{E} \quad (2.15a)$$

Similarly, for the magnetic field

$$\nabla^2 \mathbf{B} = \mu_0\sigma \frac{\partial \mathbf{B}}{\partial t} \quad (2.16)$$

$$\nabla^2 \mathbf{B} = i\omega\mu_0\sigma\mathbf{B} \quad (2.16b)$$

Equations (2.15b) and (2.16b) shows that EM fields propagate diffusively through the Earth and are exponentially attenuated.

For the plane electromagnetic waves, electric field and magnetic field with the original amplitude E_1 , angular frequency ω (period, $T = \frac{2\pi}{\omega}$) and wavelength $\lambda = \frac{2\pi}{|\mathbf{k}|}$, where \mathbf{k} is a wavenumber. The wave is assumed to propagate along the z -axis so that the XY -plane is the plane of polarization. XY -plane is the horizontal polarization, and z is positive downward.

The mathematical expressions are:

$$\mathbf{E} = \mathbf{E}_1 e^{i\omega t - kz} + \mathbf{E}_2 e^{i\omega t + kz} \quad (2.17)$$

Assuming that the Earth does not generate electromagnetic energy, \mathbf{E}_2 must be zero

$$\frac{\partial^2 \mathbf{E}}{\partial z^2} = k^2 \mathbf{E}_1 e^{i\omega t - kz} = k^2 \mathbf{E} \quad (2.18)$$

In the uniform half-space model, $\frac{\partial^2 \mathbf{E}}{\partial x^2} = \frac{\partial^2 \mathbf{E}}{\partial y^2} = 0$, thus

$$\nabla^2 \mathbf{E} = k^2 \mathbf{E} = i\omega\mu_0\sigma \mathbf{E} \quad (2.19)$$

$$k = \sqrt{i\omega\mu_0\sigma} = \sqrt{i}\sqrt{\omega\mu_0\sigma} = \frac{1+i}{\sqrt{2}}\sqrt{\omega\mu_0\sigma} = \sqrt{\omega\mu_0\sigma/2} + i\sqrt{\omega\mu_0\sigma/2} \quad (2.20)$$

The inverse of the real part of k is

$$p = \frac{1}{\text{Re}(k)} = \sqrt{2/\omega\mu_0\sigma} \quad (2.21)$$

Taking $\mu_0 = 4\pi \times 10^{-7}$, the equation (2.21) can be re-expressed as

$$p = \delta \approx 503\sqrt{\rho T} \quad (2.22)$$

Equation (2.22) is called the skin depth, the distance where the EM signal is attenuated by $1/e \approx 37\%$. The equation shows that the deep penetration of EM waves depends on the period or frequency of the signal and Earth's resistivity. Equation (2.22) also shows that a longer period is necessary to detect a deeper structure.

Taking derivative of $E_x = E_{1x}e^{i\omega t - kz}$ with respect to z , I get

$$\frac{\partial E_x}{\partial z} = -kE_x \quad (2.23)$$

Now, take the full notation of curl operator for equation (2.1)

$$\nabla \times \mathbf{E} = \left(\frac{\partial E_z}{\partial y} - \frac{\partial E_y}{\partial z}, \frac{\partial E_x}{\partial z} - \frac{\partial E_z}{\partial x}, \frac{\partial E_y}{\partial x} - \frac{\partial E_x}{\partial y} \right) \quad (2.24)$$

The B-field travels downward in the z -direction and the induced E-field does not have a z -component ($E_z = 0$). The B_z component is also zero in the inducing magnetic field due to the far distance from the source. Thus, the $\frac{\partial E_y}{\partial x}, \frac{\partial E_x}{\partial y}$ is also zero.

By comparing equation (2.24) to equation (2.1), I get

$$\frac{\partial E_x}{\partial z} = -\frac{\partial B_y}{\partial t} = -i\omega B_y = -kE_x \quad (2.25)$$

The transfer function in the Earth model describes a linear relationship between the measured physical properties in the field. The Schmucker-Weidelt transfer function, C is equal to the inverse of k .

$$C = \frac{1}{k} = \frac{E_x}{i\omega B_y}$$

$$\left| \frac{1}{\sqrt{i\omega\mu_0\sigma}} \right|^2 = \left| \frac{E_x}{i\omega B_y} \right|^2$$

$$\rho = \frac{1}{\sigma} = \frac{1}{\mu_0\omega} \left| \frac{E_x}{B_y} \right|^2 \quad (2.26)$$

Now, I see that from measuring the E-field and B-field in XY -plane and the frequency domain, the resistivity (ρ in Ωm) of the homogenous half-space can be calculated.

Z_{ij} is the second rank magnetotelluric impedance which shows the ratio between the orthogonal electric and magnetic field. The ij indicates the corresponding component's directions.

$$\mathbf{E} = \mathbf{Z} \cdot \mathbf{B} \quad (2.27)$$

$$\begin{pmatrix} E_x(\omega) \\ E_y(\omega) \end{pmatrix} = \begin{pmatrix} Z_{xx}(\omega) & Z_{xy}(\omega) \\ Z_{yx}(\omega) & Z_{yy}(\omega) \end{pmatrix} \begin{pmatrix} B_x(\omega)/\mu_0 \\ B_y(\omega)/\mu_0 \end{pmatrix} \quad (2.28)$$

$$\rho = \frac{1}{\mu_0\omega} |Z_{ij(\omega)}|^2 \quad (2.29)$$

Since $\mathbf{Z}_{ij(\omega)}$ in the frequency domain is a complex number, it has a phase that can be calculated by :

$$\phi_{ij} = \tan^{-1} \frac{\text{Im}(Z_{ij})}{\text{Re}(Z_{ij})} \quad (2.30)$$

In 1-D model of the Earth, the resistivity will vary only in the vertical direction. The magnitudes of off-diagonal components (Z_{xy}, Z_{yx}) are the same but have opposite signs. Meanwhile, the diagonal components (Z_{xx}, Z_{yy}) are zero.

$$\begin{pmatrix} E_{x(\omega)} \\ E_{y(\omega)} \end{pmatrix} = \begin{pmatrix} 0 & Z \\ -Z & 0 \end{pmatrix} \begin{pmatrix} B_{x(\omega)}/\mu_0 \\ B_{y(\omega)}/\mu_0 \end{pmatrix}$$

In a 2-D model, the resistivity is changed by one horizontal direction and also by vertical direction. The off diagonals components have different magnitudes. The x -direction and y -direction aligned along with electromagnetic strikes, so the diagonal components are zero.

$$\begin{pmatrix} E_{x(\omega)} \\ E_{y(\omega)} \end{pmatrix} = \begin{pmatrix} 0 & Z_{xy(\omega)} \\ Z_{yx(\omega)} & 0 \end{pmatrix} \begin{pmatrix} B_{x(\omega)}/\mu_0 \\ B_{y(\omega)}/\mu_0 \end{pmatrix}$$

For a 3-D Earth case, all components of the impedance tensor differ from each other. In the actual field, the Earth cannot be described only by one type of model. Instead, the impedance may show 1-D case in a short period, but as the sounding period increases, the impedance will have a 3-D model characteristic.

2.3. Geomagnetic transfer function

During data acquisition, horizontal electric field and magnetic field in xy -plane are measured as well as the vertical magnetic field. Lateral earth conductivity gradient will generate the vertical magnetic fields. The transfer function between the horizontal and vertical magnetic fields is called induction vector (*Tipper*), expressed in equation (2.30).

$$H_{z(\omega)} = (T_{zx(\omega)} \quad T_{zy(\omega)}) \begin{pmatrix} B_x/\mu_0 \\ B_y/\mu_0 \end{pmatrix} \quad (2.30)$$

$$B_z = T_{zx}B_x + T_{zy}B_y \quad (2.31)$$

The induction vector is represented as an arrow with its corresponding vector direction. The induction arrows represent lateral conductivity variations, with the tip of the arrows pointing towards the strong internal current concentrations (Parkinson criteria). If I use the Wiese criterion, the arrows will point away the current concentrations. Like $Z_{ij}(\omega)$, which has complex numbers, the tipper is composed of complex numbers. The induction arrows lengths (L) and direction (θ) can be calculated from the complex number components,

$$L = (ReT_{zx}^2 + ReT_{zy}^2)^{1/2} \quad (2.32)$$

$$\theta = \tan^{-1} \left(\frac{ReT_{zy}}{ReT_{zx}} \right) \quad (2.33)$$

For the Wiese criterion, the imaginary part is used in the calculation.

2.4. Phase tensor

The magnetotelluric impedance tensor \mathbf{Z} is composed of complex numbers (in each component) and contains phases as the relationship between the real and imaginary parts. This relationship is also described as frequency-dependent second-rank tensor (Caldwell et al., 2004). The phase tensor is graphically represented as an ellipse of the corresponding frequency (Chapter 4, Figure 4.). The major and minor axes of the ellipse indicate the principal axes of the tensor. The mathematical expression (equation 2.35) of the phase tensor shows that the tensor is free from distortion, affecting the impedance tensor.

The phase tensor is generalized as the ratio between the inverse of the real part of the impedance tensor \mathbf{X} and the imaginary part \mathbf{Y} . Given \mathbf{D} is frequency-independent distortion matrix,

\mathbf{X}_R and \mathbf{Y}_R are the real part and imaginary part of regional impedance tensor, the phase tensor can be described to be free from distortion as follow

$$\mathbf{Z} = \mathbf{X} + i\mathbf{Y} \quad (2.34)$$

$$\mathbf{\Phi} = \mathbf{X}^{-1}\mathbf{Y} \quad (2.35)$$

$$\mathbf{\Phi} = (\mathbf{D}\mathbf{X}_R)^{-1}(\mathbf{D}\mathbf{Y}_R) \quad (2.35a)$$

$$\mathbf{\Phi} = \mathbf{X}_R\mathbf{D}^{-1}\mathbf{D}\mathbf{Y}_R = \mathbf{X}_R^{-1}\mathbf{Y}_R \quad (2.35b)$$

$$\mathbf{\Phi} = \mathbf{\Phi}_R \quad (2.35c)$$

In the Cartesian coordinate (x_1, x_2) , the phase tensor is:

$$\mathbf{\Phi} = \begin{bmatrix} \Phi_{11} & \Phi_{12} \\ \Phi_{21} & \Phi_{22} \end{bmatrix} = \frac{1}{\det(\mathbf{X})} \begin{bmatrix} X_{22}Y_{11} - X_{12}Y_{21} & X_{22}Y_{12} - X_{12}Y_{22} \\ X_{11}Y_{21} - X_{21}Y_{11} & X_{11}Y_{22} - X_{21}Y_{12} \end{bmatrix} \quad (2.36)$$

The major and minor axes are calculated (equation 2.37 and 2.38) from

$$\Phi_1 = [\Phi_{11} + \Phi_{22}]/2 \quad (2.37)$$

$$\Phi_2 = [\det(\mathbf{\Phi})]^{1/2} \quad (2.38)$$

$$\Phi_3 = [\Phi_{12} - \Phi_{21}]/2 \quad (2.39)$$

$$\Phi_{max} = (\Phi_1^2 + \Phi_3^2)^{1/2} + (\Phi_1^2 + \Phi_3^2 - \Phi_2^2)^{1/2} \quad (2.40)$$

$$\Phi_{min} = (\Phi_1^2 + \Phi_3^2)^{1/2} - (\Phi_1^2 + \Phi_3^2 - \Phi_2^2)^{1/2} \quad (2.41)$$

The orientation of the axes is given as $\alpha - \beta$, in which

$$\alpha = \frac{1}{2} \tan^{-1} \left(\frac{\Phi_{12} - \Phi_{21}}{\Phi_{11} + \Phi_{22}} \right) \quad (2.42)$$

$$\beta = \frac{1}{2} \tan^{-1} \left(\frac{\Phi_{12} + \Phi_{21}}{\Phi_{11} - \Phi_{22}} \right) \quad (2.43)$$

2.5. Magnetotelluric surveys for active volcanoes

Recently, the number of investigation on volcanic structures using magnetotelluric method have been rising. The advantage of using this method for volcanic imaging are the sensitivity of MT method in detecting low resistivity zone. Hydrothermal fluids/alteration, magmatic fluids and partial melts have low resistivity magnitude than the surrounding rocks, making these area excellent target for MT studies. Since the growing number of MT studies in the volcanic field, similar low resistivity anomaly in various volcanoes were interpreted differently. In this section, a brief summary of MT studies in the volcanoes worldwide are presented.

A laterally extended cap like low resistivity zone are commonly detected at several hundred meters beneath the active volcanoes. The low resistivity anomalies have been imaged in several volcanoes such as: Aso caldera (Matsushima et al., 2020); Kirishima volcanic zone (Aizawa et al., 2014; Tsukamoto et al., 2018); Hakone volcano (Yoshimura et al., 2018); Krafla volcanic field (Lee et al., 2019) and Tulu Moye geothermal field (Samrock et al., 2018); Tongariro volcanic zone (Hill et al., 2015). The common interpretation for the thin low resistivity layer is hydrothermal alteration or clay cap, with the specific clay mineral type is smectite. Smectite is a common hydrothermal alteration mineral at temperature below 220° C (Ussher et al., 2000; Lee et al., 2020). The result from geothermal exploration drilling encountered clay mineral can support the interpretation. Beneath the layer, the increase of resistivity is caused by clay mineral transition from smectite to chlorite/epidote or propylitic which are stable at higher temperature and pose higher resistivity (Lee et al., 2020; Arnason et al., 2010). Due to low permeability, the clay cap

acts as a fluid barrier and to maintain the circulation of the underlying hydrothermal fluids. Another example, the low resistivity layer can be proposed as a combination of hydrothermal alteration and shallow aquifer layer, such as in Uturuncu Volcano (Comeau et al., 2016). Thus, it is commonly thought that low resistivity layer at shallow depth beneath active volcanoes are caused by hydrothermal alteration.

In a deeper region beneath volcano, a localized but huge low resistivity zone is detected. The general interpretation might be associated with fluids (hydrothermal or magmatic) and partial melt. However, it is noted that a single interpretation for one conductive body is difficult. Since both partial melt and hydrothermal fluids will have low resistivity magnitude due to high salinity content. The constraint from other methods such as seismic tomography or petrological analysis may convince the interpretation. For the quantitative interpretation of resistivity anomaly, several equations of bulk resistivity of a material can be used. For example, Hashin-Shtrikman upper and lower bounds, Archie's law and Waff's equation which will explain that the bulk resistivity anomaly is primarily controlled by the percentage of the constituent conductive materials and the pore connectivity (Archie, 1942; Hashin and Shtrikman, 1962; Waff, 1974;). Small amount of melt (e.g. < 20%) are the possible interpretation for the low resistivity anomaly. For example, in: Tongariro volcano (Hill et al., 2015); Uturuncu Volcano (Comeau et al., 2016); and Laguna del Maule (Cordell et al., 2018). If the subvertical conductor that span from 2-10 km bsl is imaged beneath the volcano, the possible interpretation is magmatic fluid/hydrothermal fluids. Judging whether partial melt is existed at the resistivity anomaly or not depends on the constraint of earthquakes location and constraint from other method, such as tomography of seismic, seismic attenuation etc. In the case unavailability of the constraints, the interpretation may refer to the combination between fluids and partial melt are better.

CHAPTER III

BROADBAND MAGNETOTELLURIC SURVEY

3.1. Magnetotelluric Survey Layout

The Magnetotelluric equipment is composed by 3 induction coils, 5 non polarizing electrodes, 12 V batteries, and a data logger (ADU-07 Metronix). The magnetic field is recorded using induction coil magnetometers type MFS07e which is developed by Metronix. The coil covers wide range of frequency, from 0.001 Hz – 50 kHz. To sample magnetic field in two horizontal direction North-South (H_x) and East-West (H_y) as well as vertical component (H_z), three induction coils are buried under surface. Compass and spirit level are necessary to adjust the placement of the induction coils in the ground. The electric field is measured in two horizontal orientations by using non polarizing Pb-PbCl₂ electrodes. Two dipoles are placed in two orthogonal directions. The directions are magnetic North-South and East-West direction representing E_x and E_y components then one electrode is buried as a common ground. The sensors are buried to avoid environmental disturbance, such as temperature variations, shifted sensor position due to wind or animals and also to maintain contact resistance. The induction coils are buried approximately 5 meter from the logger. One dipole of electrodes in a direction, for example North-South, should have a distance between each other approximately 10-30 meters. Longer distance will give a high signal to noise ratio (Simpson and Bahr, 2005). The installation layout of the MT equipment can be seen in Figure 3.1.

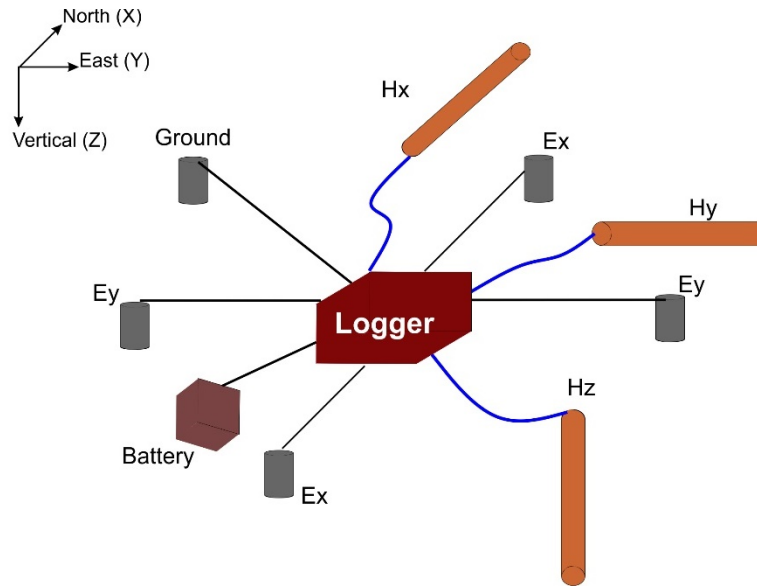


Figure 3.1 Magnetotelluric survey layout.

3.2. Broadband Magnetotelluric Observation in Shimabara Peninsula

Magnetotelluric survey in Shimabara Peninsula was conducted between 2017-2020 (four phases). In total, 99 magnetotelluric sites were installed within the survey period. Electric field (E-field) and magnetic field (B-field) were simultaneously recorded using ADU-07 equipment by Metronix geophysics at 27 sites. The magnetic field will not greatly vary in lateral direction of relatively local measurement (Munoz et al 2013), so for the efficiency the magnetic fields are not recorded at all sites. The rest 72 sites recorded only E-field using ELOG1K logger developed by NT System Design. To obtain response function the E-field only sites were paired to a close magnetic site which measured also B-field during the same period (e.g. Munoz et al 2013).

I installed the equipment in various places, such as forest, rice fields, or farms. The sites distribution is shown in Figure 1.2 (Chapter one). During the survey, I recorded the time series

data the for 5 days to 14 days at most sites, except certain ADU-07 sites 32Hz sampling frequency was used. I set sampling the sampling frequency 1024Hz for recording in midnight.

The initial phase of MT installation in Unzen volcano was begun during the end of April to middle of May 2017. In total, 27 observation points were installed which consists of 4 sites to record simultaneously E-field and B-field and 23 sites to only record E-field. All stations were distributed along nearly 9 km line in North-South direction. This line is situated about 2 km west of active summit of Unzen. The spatial distance of each sites is approximately 200-300m. The result of this survey has been published in Triahadini et al 2019.

The second phase was conducted in August 2018. In this period, 14 sites were deployed on the summit area around Myoken caldera, Fugendake and Heisei-Shinzan, and also eastern flank. Among 14 sites, two sites for recording E-field and B-field were installed in the eastern flank area considering accessibility. Meanwhile in the summit area, E-field only sites were installed. The result of this campaign is published by Hashimoto et al 2020, in which the several sites from this survey are used in this dissertation.

In December 2019, 23 stations were installed in southern part of Shimabara (Minamishimabara). Seven sites recorded E-field and B-field. Sixteen sites recorded only E-field. The sites were spatially distributed about 2-4 km. The recording period is about one week to 10 days at most sites, and 14 days for particular sites that these sites specially appointed as local reference for telluric sites.

The final MT survey in Shimabara was finished in December 2020. I deployed the equipment in northern part and eastern part of Shimabara Peninsula. Some area in southern part and western part that were not measured in previous surveys were also targeted. In total, 35 sites were installed

which consisted of 15 sites to record full component and 20 sites to record E-field only. The spatial distance of every sites was roughly same with the campaign in the previous year. The duration of recording was 10 days to three weeks.

3.3. Data Analysis

The recorded data is contaminated by noise, particularly for the frequencies at 60 Hz, 180 Hz, 300 Hz, and its overtone. I removed these noise by applying a notch filter (Aizawa et al., 2014). Then, I applied the remote reference technique to remove incoherence noise between the observation site and reference site, which simultaneously records data (Gamble et al., 1979). The remote reference geomagnetic sites for the frequency > 1 Hz sampling data are sites in Kirishima volcano complex and Kuju volcano complex, which are located more than 80 km from Shimabara Peninsula. For the frequency ≤ 1 Hz, I used geomagnetic data from Kakioka Geomagnetic observation operated by Japan Meteorological Agency. We processed the data using Bounded Influence Remote Reference code developed by Chave and Thomson (2004).

At each sites, I recorded data for several days, thus there are transfer function from each recording days for one site. For each sites, I implemented weighted average to the transfer functions from all recording days. The transfer functions (Z_{xx} , Z_{xy} , Z_{yx} , Z_{yy} , T_{zx} , T_{zy}) as the function of period were produced. Before I proceeded to inversion step, I sorted out outliers in the obtained transfer function by performing visual inspection.

3.4. Three-dimensional Inversion

In the inversion step, the calculation is performed to produce an Earth model which has minimum model norm with acceptable misfit between the observed data and the theoretical

responses. I used an inversion algorithm for 3-D model namely WSINV3DMT developed by Siripunvaraporn et al. (2005; 2009) that includes the topography. WSINV3DMT is based on data-space method for Occam's inversion. In the data-space method, the computational costs and required arrays rely primarily on the dimension of independent data N , rather than model parameters M . The inversion requires small number of iterations to achieve a reasonable model. In this inversion, the model is estimated by seeking a model with minimum norm that has appropriate fit to the data residual and smoothing parameter. The inversion can be achieved by finding stationary points of an unconstrained functional $U(\mathbf{m}, \lambda)$:

$$U(\mathbf{m}, \lambda) = (\mathbf{m} - \mathbf{m}_0)\mathbf{C}_m^{-1}(\mathbf{m} - \mathbf{m}_0) + \lambda^{-1}\{(\mathbf{d} - \mathbf{F}[\mathbf{m}])^T\mathbf{C}_d^{-1}(\mathbf{d} - \mathbf{F}[\mathbf{m}])\}$$

Here \mathbf{m} is the resistivity model, \mathbf{m}_0 is the prior model, \mathbf{C}_m the model covariance matrix which defines the model norm, \mathbf{d} the observed data, $\mathbf{F}[\mathbf{m}]$ the model response, \mathbf{C}_d the data covariance matrix, and λ^{-1} a Lagrange multiplier. The inversion requires iterative approach to overcome non-linearity in the inverse problem. There are two stage to reach the goal of inversion (Phase I and Phase II). The targeted normalize root mean square (RMS) misfit to the data is defined as $\|\mathbf{C}_d^{-1}(\mathbf{d} - \mathbf{F}[\mathbf{m}])\|/N$. During Phase I, the inversion finds the minimum norm model subject to this RMS by iterative approach.

After reaching the target misfit, the next stage keeps the misfit at the desired level while varying λ to achieve the model with smallest norm (Phase II) and the targeted misfit. Reducing the model norm is performed by $\|(\mathbf{m} - \mathbf{m}_0)\mathbf{C}_m^{-1}(\mathbf{m} - \mathbf{m}_0)\|$.

The inversion primarily depends on forward modeling for computing model responses and sensitivities. The observed data used in the inversion is the full impedance tensor including both real and imaginary parts and vertical magnetic transfer function, *tipper*. The forward model steps

solve the second order Maxwell's equations for the electric field (equation 2.15, Chapter 2) with a staggered grid finite difference numerical approach. The magnetic field components are then computed from Faraday's law $\nabla \times \mathbf{E} = i\omega\mu\mathbf{H}$ and then interpolated to the observation locations. The response impedance tensor is calculated from the combination of horizontal electric field and magnetic field. The tipper data is computed as for the horizontal magnetic components by taking curl of the electric field in Faraday's law then the result is interpolated to observation locations (cell centers). The model covariance matrix \mathbf{C}_m defines the estimated magnitude and smoothness of resistive variation relative to the base model. The 1-D diffusion equations is calculated. The decorrelation scale for the diffusion equation in all directions changed by space with length scale proportional to $\sqrt{(4\delta\tau)}$ of the local grid resolution. δ is a real number between 0 and 1 and τ is an integer number that indicates time step. Both numbers show the smoothing parameters of the model length scale. Large number of δ and τ yield a smoother model but requires more CPU time. Both parameters are user defined parameters and control the characteristic of model covariance (\mathbf{C}_m).

I set a minimum mesh in the center calculated as 800 meters for horizontal direction and 30 meters for vertical direction (at sea level until 150 meter bsl only). The highest point in the vertical direction is 1400 meter above sea level that was by divided by vertical mesh with size of 100 meter until the altitude 900 meter above sea level. Then the mesh size is changed to 50 meters in the lower altitude area, 30 meters at sea level and gradually increases size to accommodate a deeper level. The total calculated area is 600 km x 600 km x 116 km. The total number of cells is 68 x 68 x 65 in the XYZ direction (Figure 3.2). For the initial half-space resistivity, I set 100 Ωm for land, 0.25 Ωm for sea and $10^8 \Omega\text{m}$ for air.

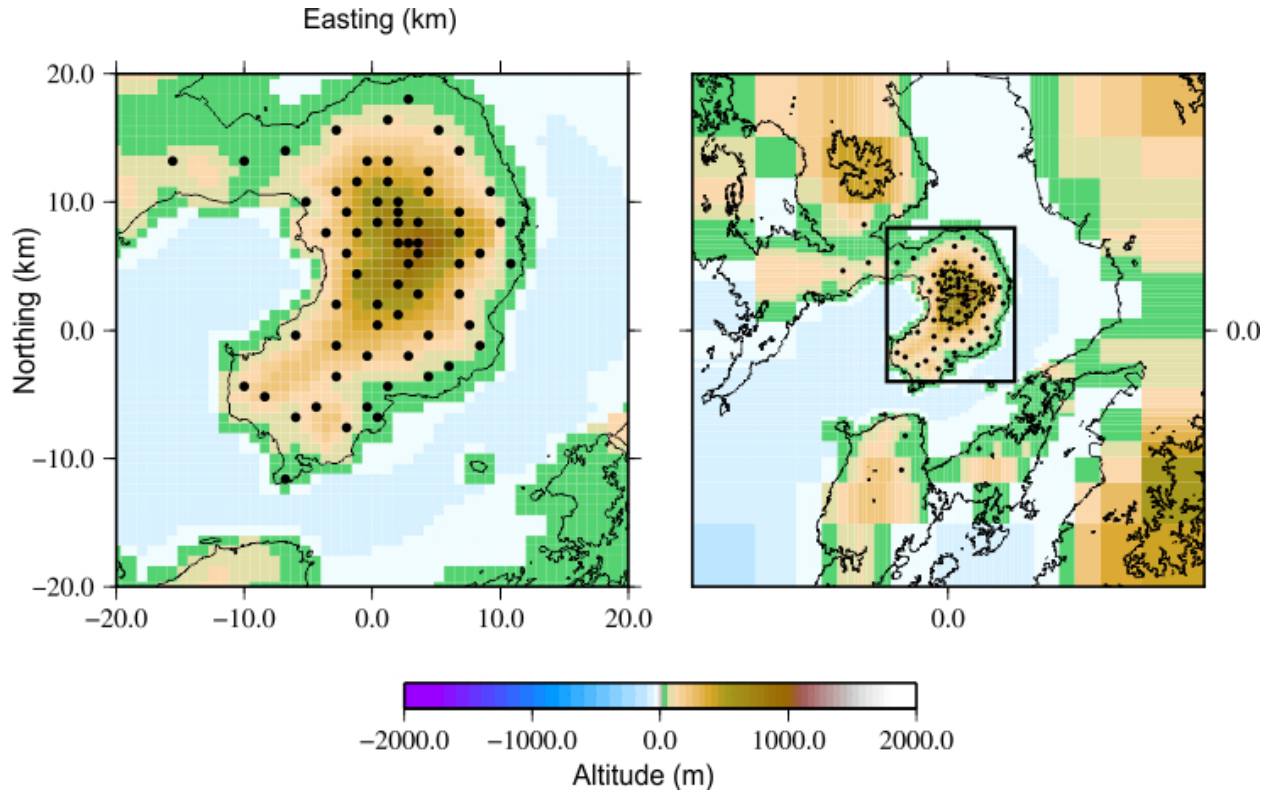


Figure 3.2. The mesh configuration and sites for 3-D inversion in this study. The sites are marked as solid black circles. I used 70 MT sites that included sites installed by Triahadini et al. (2019) and Hashimoto et al. (2020) and also Amakusa island sites.

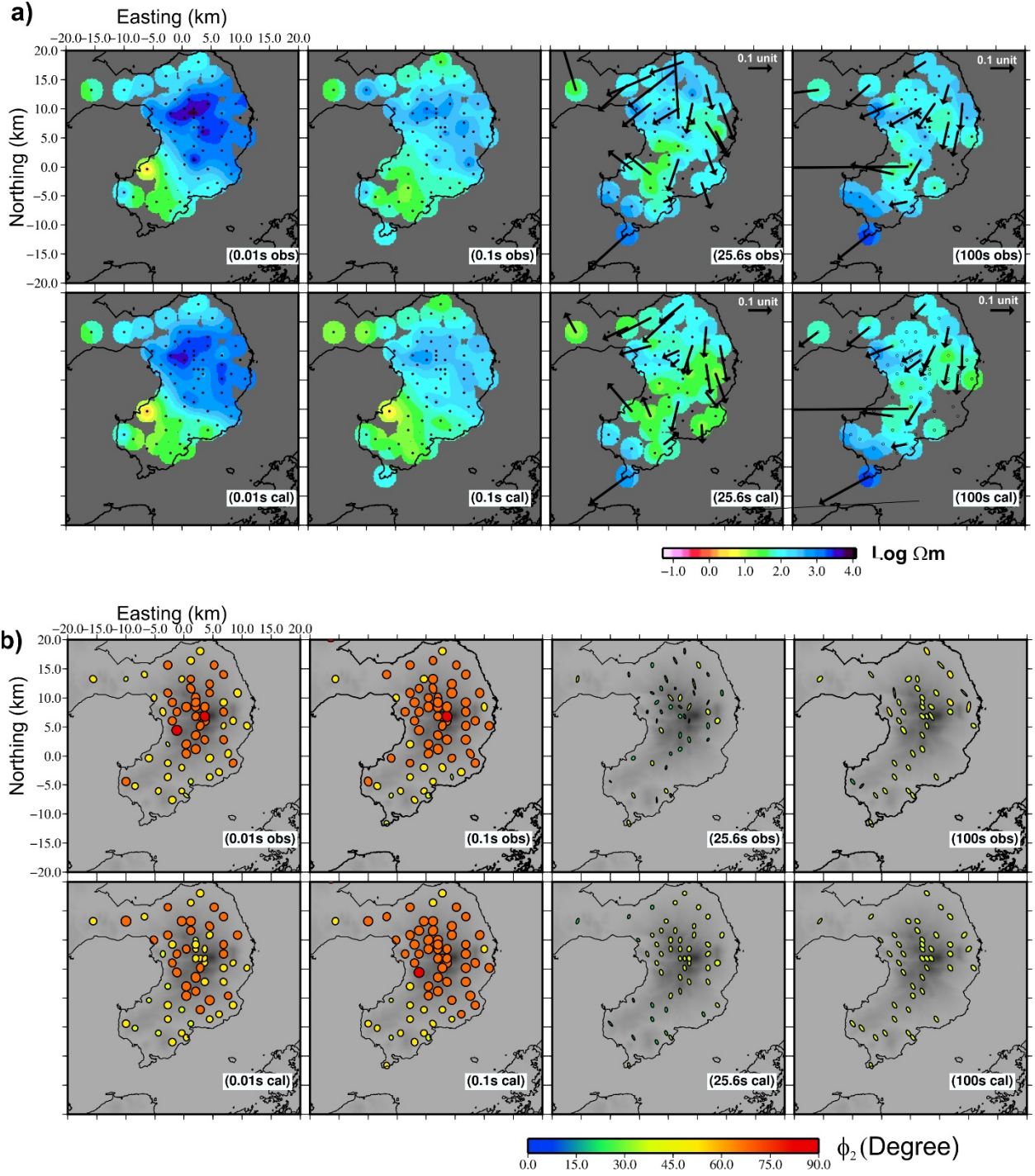
In addition to the survey sites in 2019-2020, I also used eight sites from the densely spaced MT stations in the western flank of Unzen volcano (Triahadini et al., 2019), four sites around the Heisei-shinzan and the Fugendake (Hashimoto et al., 2020), and three sites in Amakusa island. In total, I used 70 sites for the inversion. I inverted full impedance and tipper of 15 periods (0.01 – 3276 s). I excluded the diagonal component of impedance and tipper data for the period < 0.4 s. Since the inversion model inherits a non-uniqueness problem, I performed the inversions with varying parameters. The varying parameters are the initial resistivity for land, smoothing parameters τ , and error floor for the impedance tensor and tipper. On the next chapter, I show the 3-D resistivity model obtained from $\tau = 10$, $\delta x = 0.1$, $\delta y = 0.1$, $\delta z = 0.1$ with error floor 10 % for

impedance and tipper. The optimal resistivity model was obtained after 8 iterations and had RMS 1.50 from initial RMS 5.22. I confirmed that the main features of the resistivity structures discussed in the next sections were common among the models I tested.

CHAPTER IV

RESULT

The sounding curves of apparent resistivity and phases of observed data and calculated responses generally show that the inverted response can explain the observed data (Figure S2 Supplementary materials). The apparent resistivity calculated from sum of square of impedance (Rung-Arunwan et al., 2016) of observed data and calculated responses are presented in Figure 4.1a and also show good consistency between inversion response to observed data. In the phase tensor map, the colors represent the magnitude (in degree) of Φ_2 ($\sqrt{\Phi_{max}\Phi_{min}}$) which is a geometric mean of principal axes of phase tensor. It is an indicator of resistivity changes with depth (e.g. Hill et al., 2009). If $\Phi_2 > 45^\circ$ (red color), it represents that the resistivity increases with depth and vice versa (Figure 4.1b). The directions of response induction vectors generally show consistencies with observed induction vector (Figure 4.1a). The directions of induction vectors in the period 25.6 s are varied that indicate the absence of high conduction with particular geoelectric strikes. As the period increased, the vectors tend to point to the WSW direction (direction to Tachibana bay). In addition, the Φ_2 in the shorter periods are generally larger than 45° , with almost circular shapes ($\Phi_{max} \cong \Phi_{min}$) at most sites (Figure 4.1b). These are the signature of low resistivity zone is widespread in the shallow level. In the longer periods, the Φ_2 magnitudes are below 45° and deviate from the circular shape ($\Phi_{max} > \Phi_{min}$) at most sites. These features are an indication of resistivity increase with the depth and the presence of 3-D structures.



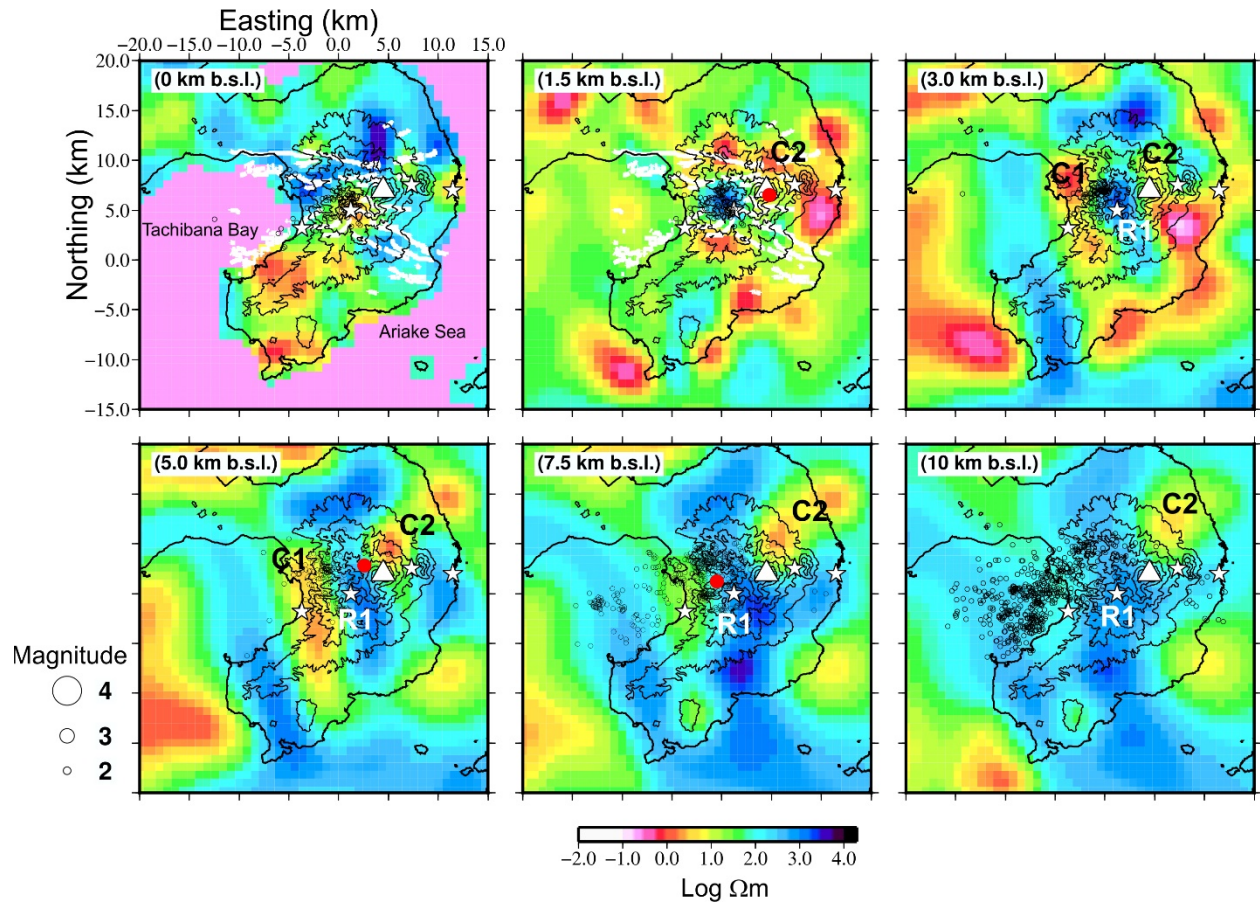


Figure 4.2 Horizontal view of resistivity structures beneath Shimabara Peninsula. Each figure corresponds to specific depth. Earthquakes (Umakoshi et al., 2001) in depth range are plotted as dots. The location of hot springs are denoted as white stars while Fugendake is represented by white triangle. The faults in Shimabara Peninsula are plotted as white lines at the two top-left figures. Three resistivity anomalies are written as C1, C2, and R1. Pressure sources of Kohno et al (2008) are marked as red circles.

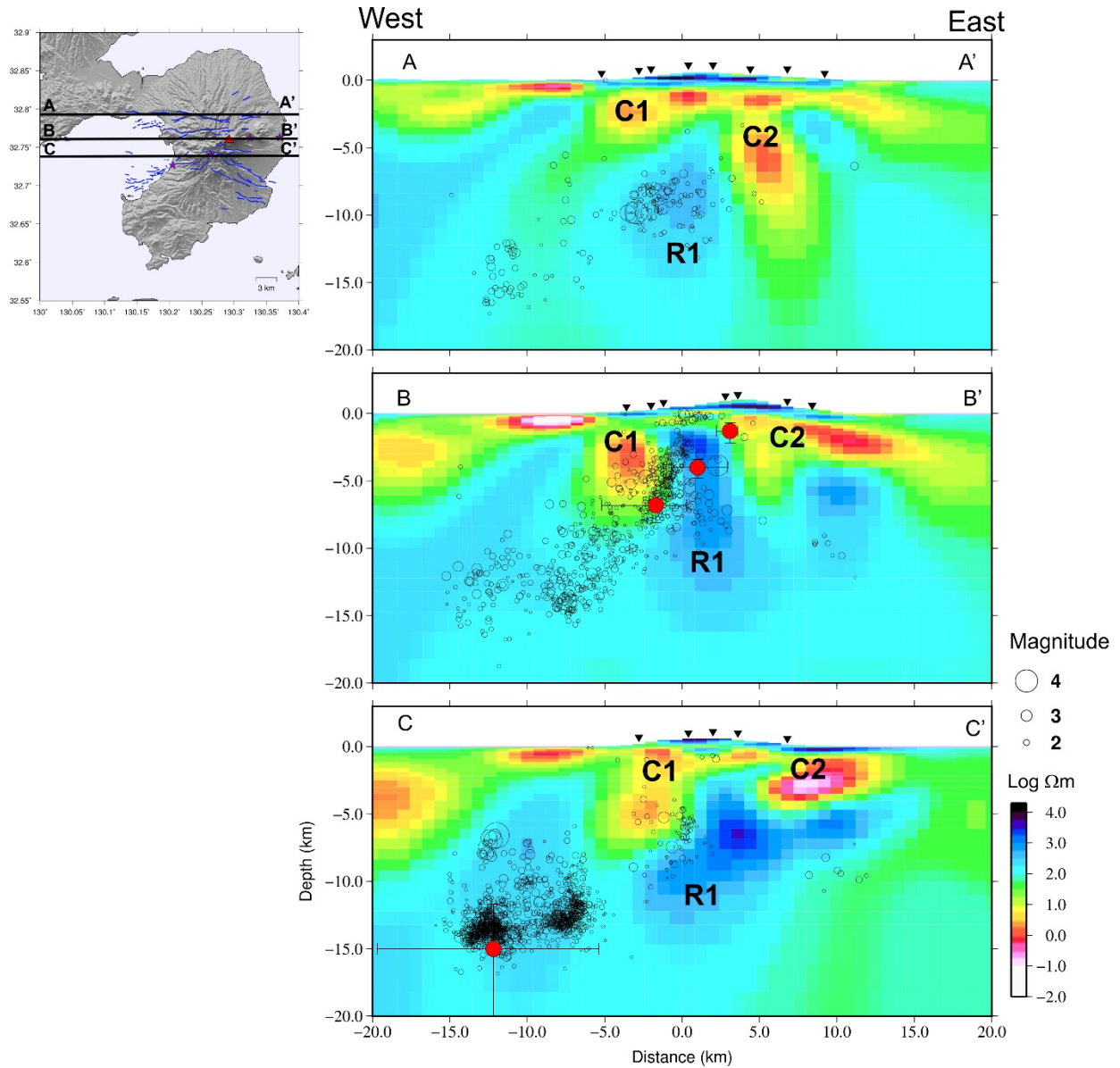


Figure 4.3. Vertical profiles of resistivity model in EW direction. A-A' : along Chijiwa Fault, B-B' : across summit Fugendake, C-C' : along southern boundary of Unzen graben. Hypocenters from the 1990-1995 eruption (Umakoshi et al., 2001) are plotted as black circles. Pressure sources (Kohno et al., 2008) are marked as red circles.

Figures 4.2 and 4.3 shows the horizontal and vertical slices of the optimal resistivity structure. Around the depth of 1-3 km b.s.l, the low resistivity zones are mostly concentrated near faults region (Figure 4.2). Especially in the northern (Chijiwa Fault) and southern boundary of Unzen

graben. The low resistivity anomaly beneath Chijiwa fault was previously detected by Triahadini et al. (2019), and was confirmed also in the new model. The low resistivity zones extend in particular places in Shimabara Peninsula which are not detected by previous MT observations. To the western coast of Shimabara Peninsula, the low resistivity zone extends into > 5 km bsl dipping to WSW, this zone is called C1. Beneath Fugendake, the low resistivity is detected until 5 km below sea level and extended to ENE of Shimabara City. I call this zone C2, and it dips into > 5 km beneath sea level beneath Ariake sea in the NE direction. Beneath the conductive zones, the high resistivity zone starts from 1.5 km in the center of Shimabara peninsula and expands to wider region in the deeper part. This zone is called R1.

I confirmed the robustness of the three anomalies by performing a sensitivity test. C1 and C2 were replaced by blocks with resistivity range 100-1000 Ωm (Figure S4, S5). Meanwhile, in the R1 region, the resistivity was modified to range 1-50 Ωm (Figure S3). Replacing those regions and running forward modeling increased the RMS of modified models. It indicates that the model needs C1-C2 and R1 as low resistivity and high resistivity zones. The details of the various sensitivity tests are shown in the Supplementary material. I also applied forward calculation for deducing the possible range of R1. When R1 was replaced by resistivity 300-10000 Ωm , the RMS was not increased, indicated that R1 can explain the resistivity values of 300-10000 Ωm . Assessing the resistivity range for C1 and C2 by the same procedures inferred that a single resistivity value could not explain C1–C2 (e.g., 10 Ωm in the whole area). The inversions with varying parameters (smoothing parameters, error floor, initial resistivity of half-space) also generally produced similar C1, C2, and R1 structures. The dimensions of C1, C2, and R1 from the inversions with various parameters differ due to the smoothing of structures but support that the three anomalies are robust. The optimal model was selected based on the model that has smoother structures, minimum

artefacts and stable RMS changes after forth iteration. Thus, the following discussion part in general is suitable for the shape differences in the anomalies. The detail of varying inversion, sensitivity tests, and forward modeling is explained in the supplementary materials.

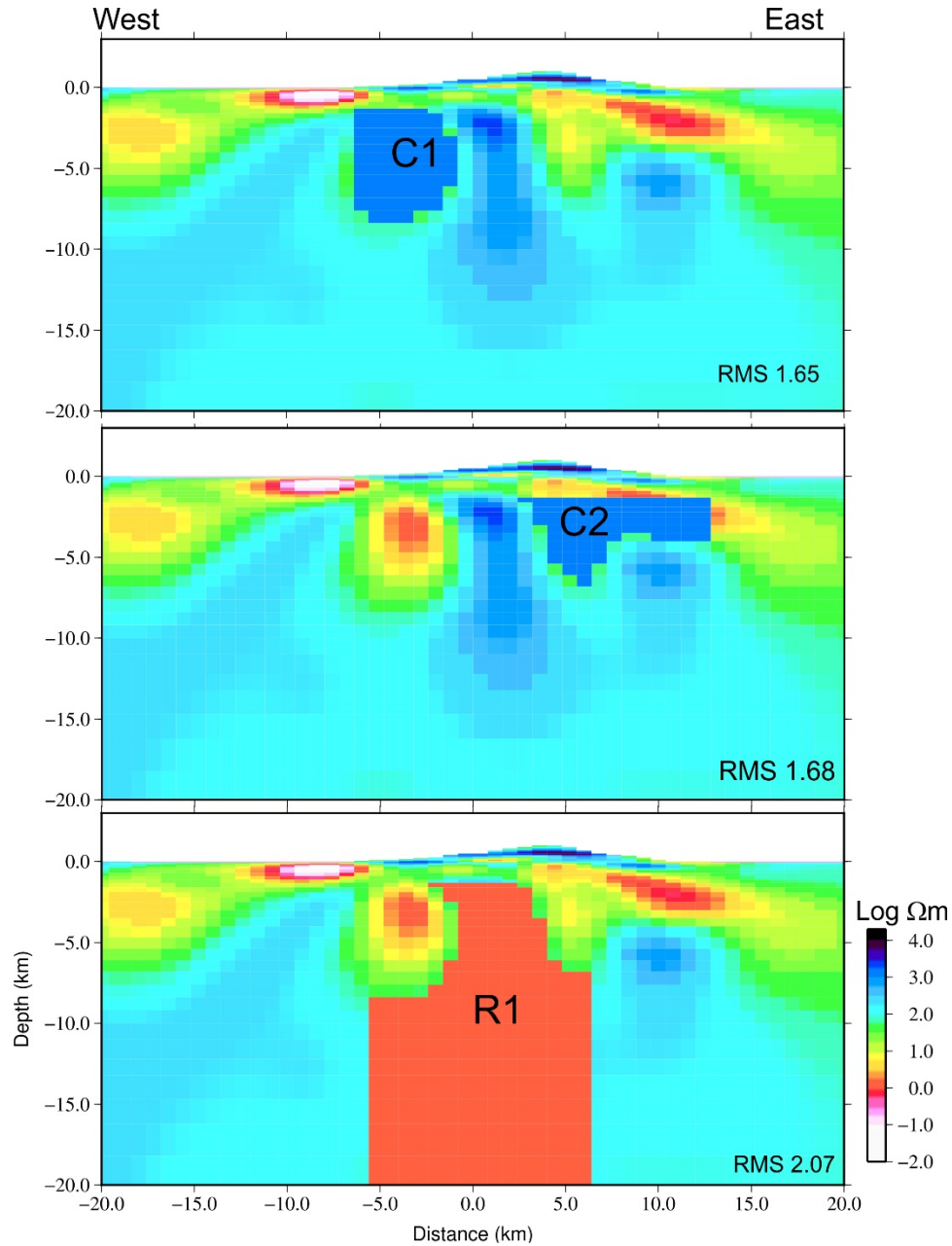


Figure 4.4 Sensitivity test in C1 (upper part) by modifying the resistivity as $1000 \Omega m$, C2 (middle part) by modifying the resistivity as $1000 \Omega m$ and R1 (lower part) by modifying the resistivity as $1 \Omega m$. The forward modeling for the three structures raised the RMS compared to the original model.

CHAPTER V

DISCUSSION

In this section, I would like to focus in the interpretation of > 1 km below sea level of Shimabara Peninsula. Details for structure in near surface level and beneath Fugendake and Heisei-shinzan lava domes are not included in the discussion.

5.1. High Resistive zone R1

The resistivity model shows a high resistive zone about 3 km west of Fugendake, at a depth around 1.5 km b.s.l (top of R1). The top of R1 spatially correlates with the location of several eroded peaks from the Older Unzen stage (> 200 ka) (Hoshizumi et al., 1999). It was thought that a high resistive zone is interpreted as solidified magma (e.g., Aizawa et al., 2014; Bedrosian et al., 2018; Matsushima et al., 2020). The top of R1 coincides with the high-velocity zone reported by Nishi (2002) and Miyano et al. (submitted) (Figure 5.1, dashed black line in Figure 5.3). Thus, I propose this zone as solidified magma intrusion from the Older Unzen stage.

R1 continues into the deeper part and broader area of the Shimabara Peninsula (Figure 4.2, 4.3, 5.1, 5.3). Figs. 5.1 and 5.3 shows the comparison between resistivity structure of this work and V_p structure (Miyano et al., submitted). At this depth, a low P-wave velocity zone (low V_p zone) exists beneath the central part of the Shimabara Peninsula at a depth > 3 km bsl (Miyano et al., submitted) (Fig. 5.1 and 5.3). Miyano et al. (submitted) interpreted LVZ beneath Shimabara Peninsula as a highly crystallized mush zone. In contrast, Yuasa et al. (2020) indicated that the southern part of the Shimabara Peninsula is a low seismicity zone that is possibly explained by the high-strength plutonic rock. In this study case, I argue that the broad high resistivity zone, R1,

cannot be solely interpreted as solidified magma or plutonic rock. We suggest that crystal mush zone with few percent of the melt can exist. In many cases, a low-velocity zone beneath volcanoes is interpreted as a high-temperature zone that may contain few percent of partial melt (e.g., Koulakov et al., 2016; Flinders and Shen, 2017; Widiyantoro et al., 2018; Wespestad et al., 2019; Yukutake et al., 2021). Quantitative melt fraction determination from velocity anomaly will suggest a few percent of melt beneath the volcano. However, in the Unzen tomography, the melt fraction of LVZ is yet calculated.

In the region containing melt or fluids, low resistivity and low-velocity zone are expected to be detected (Hyndman et al., 1993; Vanyan et al., 2001). However, recent high resolution image resistivity and velocity structure show that the locations of low resistivity and low velocity are not perfectly overlapped. For example, in Laguna del Maule, LVZ partially coincides with a broad low resistivity zone, which the latter is explained by existence of a larger melt fraction than what expected from LVZ (e.g., Cordell et al., 2020). In addition, the LVZ in Newberry volcano correlated with low resistivity zone (Bowllez-Martinez and Schlutz, 2019). The result of this study unexpectedly image broad resistive zone that correlates with broad LVZ beneath Shimabara Peninsula that was interpreted as highly crystallized mush zone (Miyano et al., submitted). Thus, I attempted to test the interpretation of highly crystallized mush zone provided by LVZ (Figure 5.1 and 5.3).

First, I calculated the possible amount of melt in R1 from the result of this work to testify the interpretation of the low-velocity zone (Figure 5.2). Mafic enclaves analysis of Unzen eruptive products and melt inclusions from 1990-1995 eruption suggest that andesitic magma was stored in a low crystallinity region before eruption with an initial temperature 945 ± 30 °C at pressure 400

MPa and water content 4%. The temperature then increased to 1010 ± 35 °C as the water content dropped to 2 % wt (Botcharnikov et al., 2008). The andesite magma mixed with more felsic magma with an estimated temperature of 730-765°C, water content 5.1-7.2% wt at pressure condition 250 and 140 MPa that indicated shallower storage condition (Nishimura et al., 2005). The dacite magma of Unzen contains a rhyolite melt composition (Nakada and Motomura, 1999). Hence, I used empirical equations (Guo et al., 2016; Guo et al., 2017) to calculate andesitic melt and rhyolite melt resistivity as function of water content, pressure, and temperature, with water content, strongly affects decreasing resistivity. The conductivity calculated from these equations are 0.18 S/m (5.55 Ωm) for andesitic melt and 0.74 S/m (1.35Ωm) for rhyolite melt. The higher percentage of water causes the lower resistivity for rhyolite melt. Since resistivity structure imaged by MT represents the bulk resistivity rather than a single phase, thus I assumed that the melts here act as the conductive phase stored in the solid host rock.

I adopted Waff (1974) equation (equation 5.1) that relates bulk conductivity as a function of the porosity and the resistivity of the conductive phase stored in a good porosity network.

$$\sigma_{bulk} = \frac{\sigma_C + (\sigma_S - \sigma_C)(1 - \frac{2}{3}F)}{1 + (\frac{F}{3})(\frac{\sigma_S}{\sigma_C} - 1)} \quad (5.1)$$

σ_C is conductivity of melt (S/m), σ_S is conductivity of crystal/solid matrix (S/m) and F is melt fraction. Then, I considered the possible range of resistivity for the R1 region, which is 300-10000 Ωm. I selected 10000 Ωm as the resistivity of the igneous host rock which serves as the solid matrix. The estimated melt fraction < 5% for andesitic melt and < 2 % for rhyolitic melt are possible to explain the bulk resistivity of R1 (Figure 5.2). Calculation of melt fraction from the velocity of Miyano et al. (submitted) yields ≤ 4 % melt fraction in the low velocity region (see Supplementary material section). However, this value is a rough estimation considering some

uncertainties in the velocity structure. Such a few melt fractions, especially for rhyolitic composition, imply that a highly crystallized mush zone is located beneath Shimabara Peninsula (Figure 5.3, Figure 5.4)

At the depth 3-6 km bsl, the tomography model shows low V_p zone and moderate V_s that Miyano et al. (submitted) interpreted this area as a volatile-rich/gas-rich zone (Figure 5.3). The volatile component is gas species contained in silicate melt. By progressing crystallization, the amount of released volatiles may increase (Shinohara, 2007). In agreement with an explanation of velocity, I propose R1 at the depth 3-6 km as a volatile-rich zone with a high amount of gas.

In the trans-crustal magma system, the evolved magma chamber will be located at the upper level of the mush zone (Cashman et al., 2017). Three of four pressure sources reported by Kohno et al. (2008) are located at the margin of R1. Pressure sources may indicate volume changes in the active magma chamber and degassing-related events (Pritchard and Simons, 2004; Segall, 2018). Regarding to the interpretation of highly crystallized mush, the positions of the pressure sources show that the active chamber (relatively mobile and rich in the melt) is located at the upper part of the mush zone. The magma movement in the trans-crustal magma system was generalized to move vertically from the center of mush region. From the result, I remark that the pathway magma from the 1990-1995 eruption shows preferred oblique movement at the upper boundary of highly crystallized mush zone (Figure 5.4).

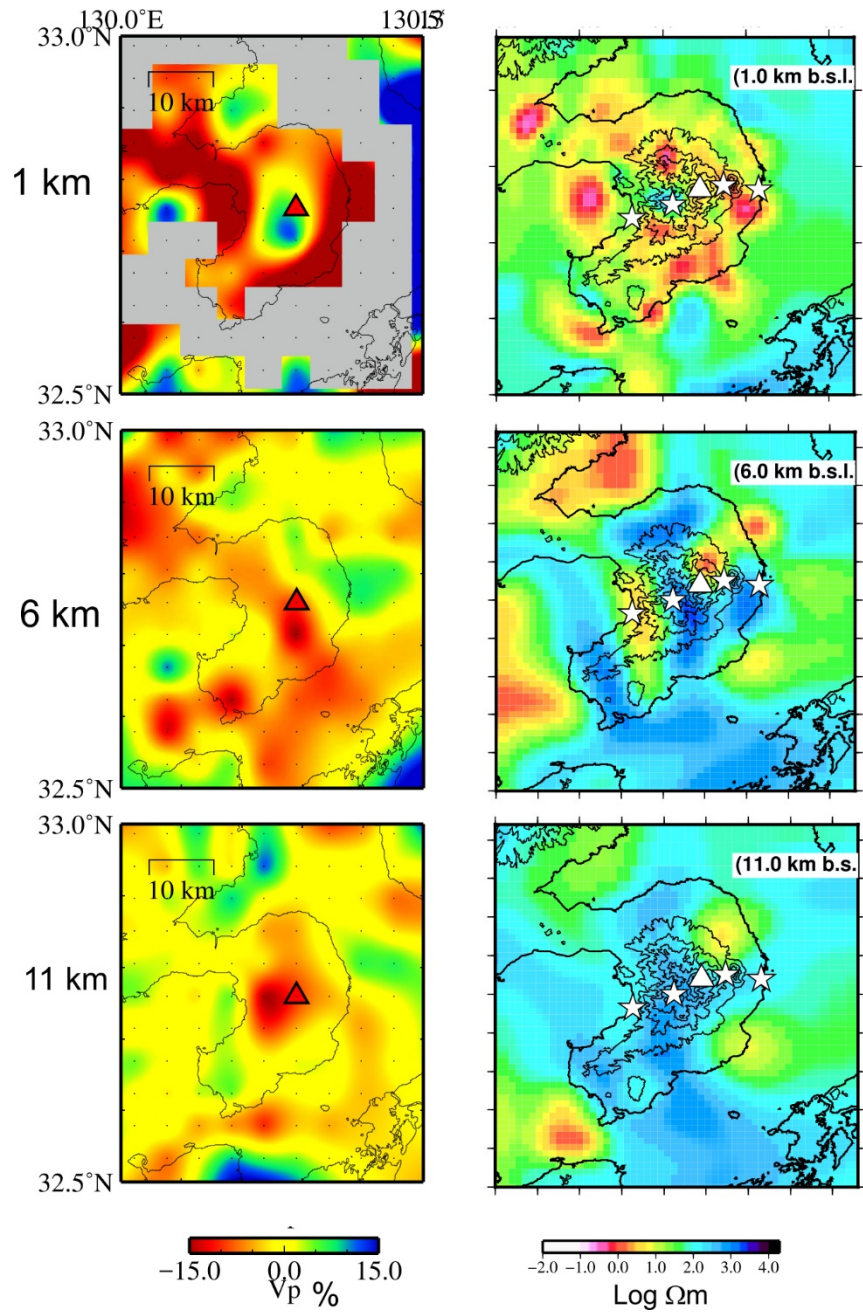


Figure 5.1. Comparison between seismic P-wave velocity of tomography (Miyano et al., submitted) and resistivity structure in horizontal view for depth 1 km bsl, 6 km bsl and 11 km bsl beneath Shimabara Peninsula.

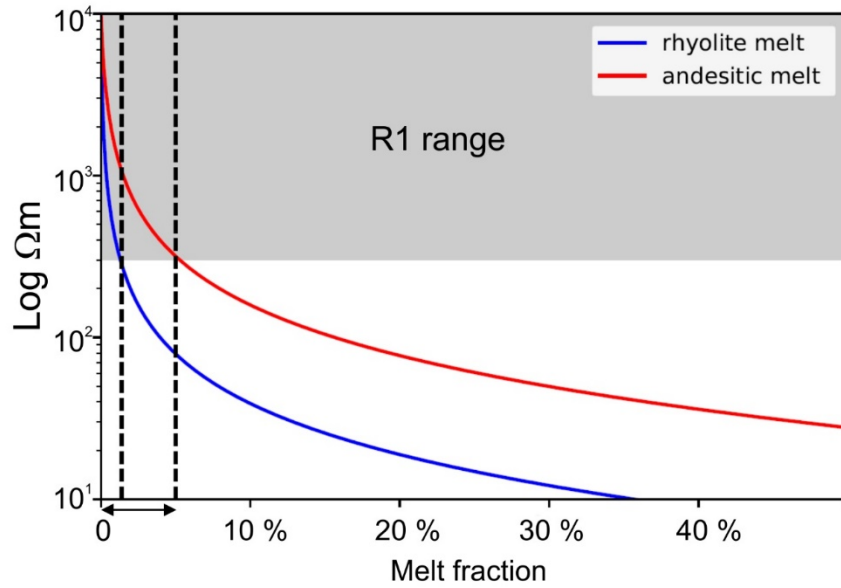


Figure 5.2. Melt fraction estimation (Waff, 1974) in R1 using melt inclusion data (Nishimura et al., 2005; Botcharnikov et al., 2008). The possible range for melt fraction in R1 for andesitic and rhyolite melt is below 5 % and it is denoted by arrow at below the curve.

The small size melt-rich magma chamber at the depth of pressure sources was not detected by the MT data. Laboratory analysis of Unzen erupted samples presented that the magma chamber remains active from 1663, 1792, and later incorporated into the last 1990-1995 eruption (Nakamura, 1995). In addition, Sugimoto et al. (2005) proposed a continuous plumbing system beneath Shimabara Peninsula throughout the formation of the Unzen volcano based on mafic inclusions and whole rock elements analysis of Unzen volcanic rocks. However, my finding demonstrates that beneath the Unzen volcano, a highly crystallized mush zone exists with a small amount $< 5\%$ of melt fraction. If the mobile/eruptive magma chamber exists at a depth of pressure sources, the size might be too small to be detected by MT method since MT cannot detect 1 km^3 magma chamber at 5 km depth.

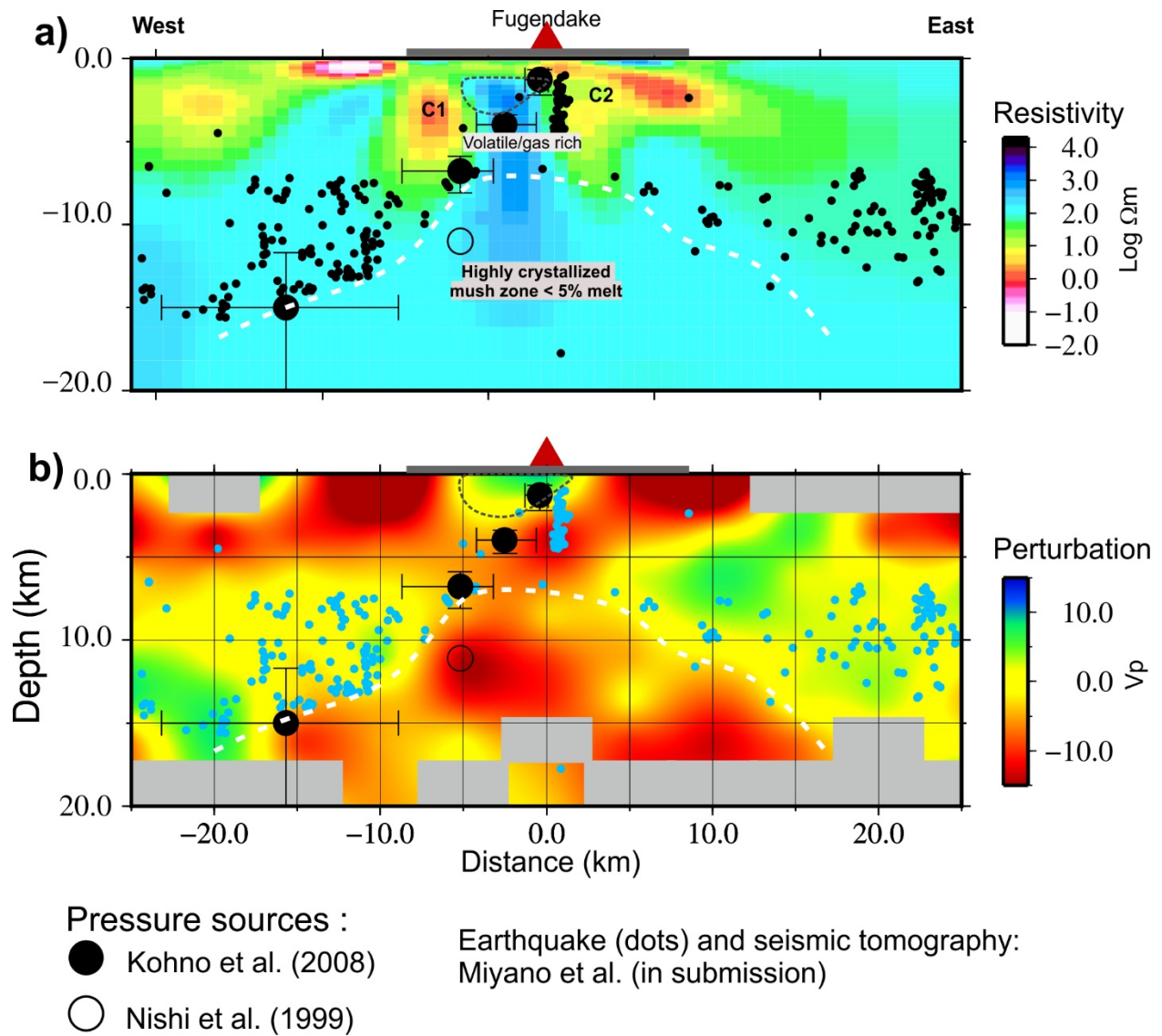


Figure 5.3. Comparison of a resistivity profile and P-wave velocity perturbations based on the seismic tomography of Miyano et al. (submitted) across the summit Fugendake (red triangle). Pressure sources are from Kohno et al. (2008) and Nishi et al. (1999). Dots indicate earthquakes used in the seismic tomography inversion. The location of Shimabara Peninsula is indicated by the horizontal gray line at the top center of each profile. Dashed black lines indicate areas of high resistivity and high velocity, interpreted as solidified magma. White dashed lines mark the boundary between a volatile/gas-rich zone and a highly crystallized mush zone.

5.2. Low resistivity zone at shallow level

A relatively thin 1-2 km low resistivity zone spreading in the shallow level of Shimabara Peninsula can be interpreted as a fluid-rich and hydrothermal alteration/clay cap zone. Smectite is a conductive clay mineral that is only stable below 200° C and above that temperature, the mineral can be changed to a less conductive clay mineral (Ussher et al., 2000). Smectite is thought to exist beneath active volcanoes in Japan, and it is associated with low resistivity zone (e.g., Tsukamoto et al., 2018; Yoshimura et al., 2018; Tseng et al. 2020; Gresse et al., 2021). I agree with the possibility that the smectite clay layer exists in the 1-2 km beneath Shimabara Peninsula. It is supported by the drilling USDP4 that encountered conduit zone that was cooled rapidly to < 200° C due to hydrothermal fluids circulation, suggesting that alteration and cooling occurred shortly after magma injection and eruption, respectively (Nakada et al., 2005; Sakuma et al., 2008; Tretner et al., 2008). The conclusion for hydrothermal clay cap and fluids rich zone agrees with previous MT detection of low resistivity zones in the near-surface level to 2 km beneath Shimabara Peninsula. The interpretation of these low resistivity zones is an aquifer, hydrothermal fluids rich layer, or hydrothermal alteration/clay (Kagiyama et al., 1999; Srigutomo et al., 2008; Komori et al., 2013; Triahadini et al., 2019; Hashimoto et al., 2020).

5.2.1 C1 and C2

It is common that deep low resistivity zones beneath the volcanoes were explained by magmatic/hydrothermal fluids or partial melt. The pathway for the magma migration was also imaged as a low resistivity zone (e.g., Aizawa et al., 2014; Hill et al., 2015; Hata et al., 2016; Comeau et al., 2016; Cordell et al., 2018; Matsushima et al., 2020). These low resistivity zones could partially overlap with low velocity zones. The interpretation of low resistivity zone as magmatic fluid/melt was also supported by deformation sources and/or the earthquakes clustered in the upper edge of the low resistivity zones (e.g. Aizawa et al., 2014; Hata et al., 2016; Comeau

et al., 2016). The increasing pore pressure due to escaped volatiles or fluids and failure of rock wall by magma injection can induce earthquakes. However, the earthquakes and pressure sources of the 1990-1995 eruption (Umakoshi et al., 2001) are not located at the top of C1 or C2, but located at the bottom of C1 and C2 (Figure 4.3). Melt inclusions analysis from erupted samples estimated the storage locations of andesitic and dacitic magma roughly at the depth range of pressure source beneath Tachibana bay ~15 km bsl and western Shimabara at 6-7 km bsl, respectively. These depth ranges are below C1 (Nishimura et al., 2005; Botcharnikov et al., 2008) and at the upper part of R1. Because of the discrepancies of depth between the suggested magma chambers and the low resistivity zones, I excluded partial melt as the candidate for interpretation of C1 and C2. Several candidates for C1 and C2, such as saline fluid/brine and graphite, are considered.

I noted that in the central parts of C1 and C2 are low seismicity which is possibly due to high temperature $> 400^{\circ}\text{C}$ or ductile/plastic zone (Fournier, 1999). The deformation sources and seismicity of the 1990-1995 eruption that marked magma migration are located at the boundary between C1 and R1. These facts imply that the boundary between C1 and R1 has relatively higher permeability than the center. Thus, I think it is possible that brine with a temperature higher than 400°C causes low resistivity of C1 and C2 (Figure 5.3).

I argue that brine in interconnected pores with temperature above 400°C probably exists in the C1. From low resistivity zones detected in several volcanoes, Afanasyev et al. (2018) performed numerical modelling to assess the evaluation of H_2O - NaCl fluids system under volcanoes. Fluids discharged from a cooling magma body into overlying rocks via permeable pathway likely form a brine lens in any magmatic system that composed of water saturated igneous rocks with temperature $\sim 670^{\circ}\text{C}$ or above and with high content of salinity. The brine lenses can

persist for more than 250 kyr after degassing ceased hence low resistivity zones ($< 1 \Omega\text{m}$) can be imaged under dormant volcanoes. Moreover, crustal fluids are commonly conductive due to the enrichment of chloride and bicarbonate salts (Nesbitt, 1993, Sinmyo and Keppler, 2016). Sinmyo and Keppler (2017) predicted that not more than 1 % wt aqueous fluids with 5 % NaCl in continuous films/pores will produce resistivity by $< 1 \Omega\text{m}$ at temperature $\leq 400^\circ\text{C}$. This scenario seems applicable in Unzen since crystallization process in the mush region might release saline fluids. The released volatiles with high salinity are then incorporated into the crustal fluids causing sodium enrichment.

On Figure 4.2, it is seen that the hotspots in Shimabara Peninsula (Obama, Unzen, Shimabara, and one buried hot springs) are not directly above the low resistivity zone but in the edge the low resistivity zone. The hot springs is thought to receive fluids supply from high permeability low resistivity zone (e.g., Tsukamoto et al., 2018; Matsushima et al., 2020). However, judging from the fact that hot springs in Shimabara Peninsula that are situated on the edge of low resistivity zones, it indicates that the high permeability path is not equally distributed in all parts of low resistivity zone but concentrated on in the edge of the low resistivity zone. This permeability distribution concept has been proposed by Aizawa et al. (2021) to explain the distribution of low resistivity zone in Kujū Volcanoes. It is worth noting that although Shimabara Hotspring has the lowest temperature than the other hot springs in Shimabara, however the ratio of $^3\text{He}/^4\text{He}$ (an indicator of magmatic gas incorporation) is the highest (Kita et al., 1993; Morikawa et al., 2008). The location of the Shimabara hotspring at the perimeter of C2 may indicate brine influence from C2.

Graphite is the reduced form of carbon, and it is a highly conductive material (10^{-4} - $10^{-5} \Omega\text{m}$ at 500°C) that a small amount ($< 0.1\%$) of graphite will drastically reduce bulk resistivity (Duba

and Shankland, 1992; Hyndman et al., 1993). Graphite can also become the fault lubricant leading to faults creeping (Oohashi et al., 2012; Kuo et al., 2018). To form graphitization in a volcanic setting requires unusually high carbon content of magmas and the absence of degassing (Luque et al., 2012), which are unlikely for the Unzen case where the magma was highly degassed. Luque et al. (2012) also mentioned that dissolved carbon-bearing aqueous fluids could induce graphitization. Considering the highly crystallized mush zone mentioned in the previous section, it is possible that the cooling or solidification process of magma intrusion beneath Shimabara Peninsula could release carbon-bearing material that induced graphitization. Bedrosian et al. (2018) proposed a low resistivity zone enclosing batholith as the metasedimentary rocks contain graphite where a small batch of magma is occasionally transported through the low resistivity zone.

Fluids and graphite filling interconnected porosity networks can co-exist and cause a low resistivity zone (Figure 5.4). I calculated brine and/or graphite percentage that can co-exist in the interconnected pores in C1 and C2 by using the same equation for melt calculation in R1 (Waff, 1974). Assuming resistivity of pure brine is $0.01 \Omega\text{m}$ (Nesbitt, 1993) and $10^{-4} \Omega\text{m}$ for graphite that are stored in the $10^4 \Omega\text{m}$ solid host rock, it is resulted that minimum 3% of brine is necessary for bulk resistivity $1 \Omega\text{m}$ and more percentage of brine for lower resistivity. Graphite $\sim 0.1 \%$ adequately explains bulk resistivity $< 1 \Omega\text{m}$. Although there are no outcrops or evidence of graphite found in the vicinity of Shimabara Peninsula, I cannot deny a possibility that very few percent of graphite will exist at C1 and C2. Thick deposits of volcanic materials are likely to cover the evidence of graphite.

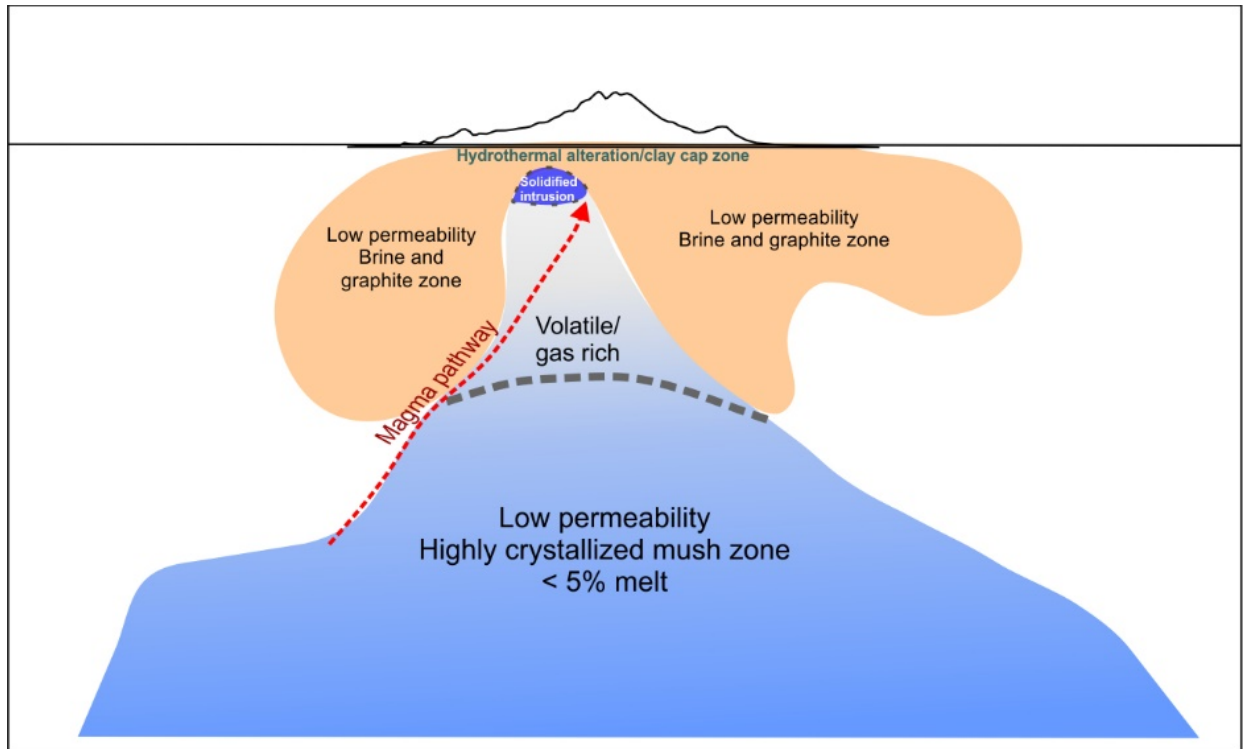


Figure 5.4 Conceptual model of magma transport and subsurface structure beneath Unzen volcano, Shimabara Peninsula. At the top of volatile/gas rich zone, solidified intrusion is modeled. The boundary between volatile/gas rich zone and highly crystallized mush zone is marked as grey dashed line.

CHAPTER VI

CONCLUSION

I successfully imaged, for the first 3-D resistivity structures to a depth of 20 km beneath Unzen volcano and Shimabara Peninsula based on broadband Magnetotelluric observations. The model developed from this study shows a thin near-surface low resistivity zone near the faults zone of Unzen graben and beneath Unzen volcano. The low resistivity zone is inferred to reflect hydrothermal fluids/alteration and/or clay-rich cap zone. The other low resistivity zones are extended into 7.5 km beneath the western end of Shimabara Peninsula and 7.5 km beneath the Unzen volcano to 10 km to the east, under the Ariake sea. Given that the low-resistivity zone do not coincide with deformation sources and earthquakes location related to magma movement of the most recent eruption, I argue that the low-resistivity zone does not reflect the presence of partial melt. However, the zone might be characterized by brine/saline fluids-rich zone and/or minor graphitization.

The model also shows a broad high resistivity zone ($> 100 \Omega\text{m}$) beneath most of the part of Shimabara Peninsula that surprisingly coincides with a zone of low P-wave velocities at depths of 3 km-6 km depth (Miyano et al., submitted). It is estimated that the high-resistivity zone contains $< 5 \%$ melt. Consequently, the upper part of the resistive zone is interpreted as a gas/volatile-rich zone and the lower part as a highly crystallized mush zone containing $< 5 \%$ melt. Given the absence of a low resistivity zone in the inferred location of the magma chamber, I argue that the active magma chambers are of a smaller dimension than the MT resolution. The earthquakes and deformation sources relating to the most recent eruption in 1990-1995 (Umakoshi et al., 2001; Kohno et al., 2008) are located along the boundary between the low-resistivity anomaly in the western end of Shimabara and the deep high-resistivity body. It is proposed that during the last

eruption the magma along this boundary, where fracturing has created a high permeability zone. The present results provide evidence of magma movement along the upper boundary of the highly crystallized mush zone.

ACKNOWLEDGEMENTS

On this opportunity, I would like to express my gratitude to Associate Professor Koki Aizawa as my supervisor and who provide guidance and supports throughout my study time and research activities at Kyushu University. I would like to thank Professor Hiroshi Shimizu, Professor Satoshi Matsumoto, and Associate Professor Takeshi Matsushima for all discussion and constructive comments to improve my research. Also thanks to Professor Takeshi Hashimoto for the comments on my dissertation manuscript and Professor Kodo Umakoshi for providing hypocenters data. Special appreciation for the laboratory members, Technical Staff Kazunari Uchida and Yoshiko Teguri, Dr. Keita Chiba, and students for their efforts for the Magnetotelluric surveys from 2017 to 2020s. I also would like to thank to Dan Muramatsu, Kanta Miyano, and Shiho Fujimura, for all of the friendships and assistance in my daily life in Japan.

I express my greatest thanks to my parents and my sisters for all of their love and prayers. I am also grateful to meet Indonesian students in Kyushu University: Indranova Suhendro, Gabriela N.R. Bunga Naen, Selvia Novianti, Rezkia Dewi Anjani, Saefudin Juhri, Fakhri Akbar and Arisha Livia Satari; former Kyushu University Students: Dr. Rizki Reza Fauzi, Dr. Patmawati Wahyudin, Aluthsyah Luthfian, and Syuaibatul Islamiyah for all of their supportive friendships.

I am honored and owe great thanks to all foundations/organizations that funded my study at Kyushu University from 2016 to the present. LPDP by the Ministry of Finance Republic of Indonesia that supported my master study, Fukuoka City International Center, Kyushu University Graduate School research support, and Kyushu University's volcano project-special scholarship for the funding I received for my Doctoral course.

Lastly, I and all the members that working for this MT project are greatly indebted to the landowners for their permission to conduct MT field campaigns. The geomagnetic data used in the remote reference processing were provided partly by the Kakioka Geomagnetic Observatory of JMA. MT equipment was used under the Joint Usage Program of the Earthquake Research Institute, The University of Tokyo. The inversion step and part of figure creation were performed under Earthquake Research Institute Computer System (EIC), The University of Tokyo. This work is also supported by the Ministry of Education, Culture, Sports, Science and Technology (MEXT) under its Earthquake and Volcano Hazards Observation and Research Program).

REFERENCES

- Afanasyev, A., Blundy, J., Melnik, O., & Sparks, S. (2018). Formation of magmatic brine lenses via focussed fluid-flow beneath volcanoes. *Earth and Planetary Science Letters*, 486, 119–128. <https://doi.org/10.1016/j.epsl.2018.01.013>
- Aizawa, K., Koyama, T., Hase, H., Uyeshima, M., Kanda, W., Utsugi, M., Yoshimura, R., Yamaya, Y., Hashimoto, T., Yamazaki, K., Komatsu, S., Watanabe, A., Miyakawa, K., & Ogawa, Y. (2014). Three-dimensional resistivity structure and magma plumbing system of the Kirishima Volcanoes as inferred from broadband magneto-telluric data. *Journal of Geophysical Research: Solid Earth*, 119, 198–215, doi:10.1002/2013JB010682.
- Aizawa, K., Takakura, S., Asaue, H., Koike, K., Yoshimura, R., Yamazaki, K., Komatsu, S., Utsugi, M., Inoue, H., Tsukamoto, K., Uyeshima, M., Koyama, T., Kanda, W., Yoshinaga, T., Matsushima, N., Uchida, K., Tsukashima, Y., Matsushima, T., Ichihara, H., Shimizu, H. (2021). Electrical conductive fluid-rich zones and their influence on the earthquake initiation, growth, and arrest processes: observations from the 2016 Kumamoto earthquake sequence, Kyushu Island, Japan. *Earth, Planets and Space*, 73(1). <https://doi.org/10.1186/s40623-020-01340-w>.
- Aizawa, K., Utsugi, M., Kitamura, K., Koyama, T., Uyeshima, M., Matsushima, N., Takakura, S., Inagaki, H., Saito, H., & Fujimitsu, Y. (2021). Magmatic fluid pathways in the upper crust: Insights from dense magnetotelluric observations around the Kuju Volcanoes, Japan, *Geophysical Journal International*, in press.
- Archie, G. E. (1942). The electrical resistivity log as an aid to determining some reservoir characteristics. *Trans. A.I.M.E.* 145: 389–409.
- Árnason, K., Eysteinnsson, H., & Hersir, G. P. (2010). Joint 1D inversion of TEM and MT data and 3D inversion of MT data in the Hengill area, SW Iceland. *Geothermics*, 39(1), 13–34. <https://doi.org/10.1016/j.geothermics.2010.01.002>.
- Bachmann, O., & Bergantz, G. (2008). The magma reservoirs that feed supereruptions. *Elements*, 4(1), 17–21. <https://doi.org/10.2113/GSELEMENTS.4.1.17>.
- Bedrosian, P. A., Peacock, J. R., Bowles-Martinez, E., Schultz, A., & Hill, G. J. (2018). Crustal inheritance and a top-down control on arc magmatism at Mount St Helens. *Nature Geoscience*, 11(11), 865–870. <https://doi.org/10.1038/s41561-018-0217-2>.
- Botcharnikov, R. E., Holtz, F., Almeev, R. R., Sato, H., & Behrens, H. (2008). Storage conditions and evolution of andesitic magma prior to the 1991–95 eruption of Unzen volcano: Constraints from natural samples and phase equilibria experiments. *Journal of Volcanology and Geothermal Research*, 175(1–2), 168–180. <https://doi.org/10.1016/j.jvolgeores.2008.03.026>.

- Bowles-Martinez, E., & Schultz, A. (2020). Composition of Magma and Characteristics of the Hydrothermal System of Newberry Volcano, Oregon, From Magnetotellurics. *Geochemistry, Geophysics, Geosystems*, 21(3), 1–18. <https://doi.org/10.1029/2019GC008831>.
- Blundy, J., Afanasyev, A., Tattitch, B., Sparks, S., Melnik, O., Utkin, I., & Rust, A. (2021). The economic potential of metalliferous sub-volcanic brines. *Royal Society Open Science*, 8(6), 202192. <https://doi.org/10.1098/rsos.202192>
- Cagniard, L. (1953). Basic theory of the magnetotelluric method of geophysical prospecting. *Geophysics*. 15: 31-36.
- Caldwell, T. G., Bibby, H. M., & Brown, C. (2004). The magnetotelluric phase tensor. *Geophysical Journal International*, 158(2), 457–469. <https://doi.org/10.1111/j.1365-246X.2004.02281.x>.
- Cashman, K. V., Sparks, R. S. J., & Blundy, J. D. (2017). Vertically extensive and unstable magmatic systems: A unified view of igneous processes. *Science*, 355(6331). <https://doi.org/10.1126/science.aag3055>.
- Chave, A.D. & Jones, A.G. (2012). The Magnetotelluric Method: Theory and Practice. *Cambridge University Press*.
- Chave, A.D., Thomson, D.J. (2004). Bounded influence magnetotelluric response function estimation. *Geophysics Journal International*, 157(3):988–1006. <https://doi.org/10.1111/j.1365-246X.2004.02203.x>.
- Comeau, M. J., Unsworth, M. J., & Cordell, D. (2016). New constraints on the magma distribution and composition beneath Volcan Uturuncu and the southern Bolivian Altiplano from magnetotelluric data. *Geosphere*, 12(5), 1391–1421. <https://doi.org/10.1130/GES01277.1>
- Cordell, D., Unsworth, M. J., & Díaz, D. (2018). Imaging the Laguna del Maule Volcanic Field, central Chile using magnetotellurics: Evidence for crustal melt regions laterally-offset from surface vents and lava flows. *Earth and Planetary Science Letters*, 488, 168–180. <https://doi.org/10.1016/j.epsl.2018.01.007>.
- Duba, A.G. and Shankland, T.J. (1982). Free carbon and electrical conductivity in the Earth's mantle. *Geophysical Research Letters*, Vol. 9, No.11, 1271-1274.
- Edmonds, M., Cashman, K.V., Holness, M., & Jackson, M. (2019). Architecture and dynamics of magma reservoirs. *Philosophical Transactions Royal Society A*, 377: 20180298. <http://dx.doi.org/10.1098/rsta.2018.0298>.
- Flinders, A. F., & Shen, Y. (2017). Seismic evidence for a possible deep crustal hot zone beneath Southwest Washington. *Scientific Reports*, 7(1), 1–10. <https://doi.org/10.1038/s41598-017-07123-w>.

- Gamble, T. D., Goubau, W. M., & Clarke, J. (1979). Magnetotellurics with a remote magnetic reference. *Geophysics*, 44(1), 53–68. <https://doi.org/10.1190/1.1440923>.
- Gresse, M., Uyeshima, M., Koyama, T., Hase, H., Aizawa, K., Yamaya, Y., Morita, Y., Weller, D., Rung-Arunwan, T., Kaneko, T., Sasai, Y., Zlotnicki, J., Ishido, T., Ueda, H., & Hata, M. (2021). Hydrothermal and magmatic system of a volcanic island inferred from magnetotellurics, seismicity, self-potential, and thermal image: an example of Miyakejima (Japan). *Journal of Geophysical Research: Solid Earth*. <https://doi.org/10.1029/2021jb022034>.
- Glover, P. J., Hole, M. J., & Pous, J. (2000). A modified Archie's law for two conducting phases. *Earth and Planetary Science Letters*, 180, 369–383. [https://doi.org/10.1016/S0012-821X\(00\)00168-0](https://doi.org/10.1016/S0012-821X(00)00168-0)
- Guo, X., Zhang, L., Behrens, H., & Ni, H. (2016). Probing the status of felsic magma reservoirs: Constraints from the P-T-H₂O dependences of electrical conductivity of rhyolitic melt. *Earth and Planetary Science Letters*, 433(January 2020), 54–62. <https://doi.org/10.1016/j.epsl.2015.10.036>.
- Guo, X., Li, B., Ni, H., & Mao, Z. (2017). Electrical conductivity of hydrous andesitic melts pertinent to subduction zones. *Journal of Geophysical Research: Solid Earth*, 122(3), 1777–1788. <https://doi.org/10.1002/2016JB013524>.
- Hashimoto, T. M., Aizawa, K., Hayashida, Y., Yuasa, Y., Matsushima, T., Yamamoto, Y., Tsukamoto, K., Miyano, K., Matsumoto, S., & Shimizu, H. (2020). Joint seismological – magnetotelluric investigation of shallow and implosive non-DC and DC earthquakes beneath the gravitationally unstable Heisei-Shinzan Lava Dome, Unzen Volcano, Japan. *Journal of Volcanology and Geothermal Research*, 406, 107066. <https://doi.org/10.1016/j.jvolgeores.2020.107066>.
- Hashin, Z. and Shtrikman, S. (1962). A variational approach to the theory of the effective magnetic permeability of multiphase materials. *Journal of Applied Physics*. 33: 3125–3131
- Hata, M., Takakura, S., Matsushima, N., Hashimoto, T., & Utsugi, M. (2016). Crustal magma pathway beneath Aso caldera inferred from three-dimensional electrical resistivity structure. *Geophysical Research Letters*, 43(20), 10,720–10,727. <https://doi.org/10.1002/2016GL070315>.
- Hill, G. J., Bibby, H. M., Ogawa, Y., Wallin, E. L., Bennie, S. L., Caldwell, T. G., Keys, H., Bertrand, E. A., & Heise, W. (2015). Structure of the Tongariro Volcanic system: Insights from magnetotelluric imaging. *Earth and Planetary Science Letters*, 432, 115–125. <https://doi.org/10.1016/j.epsl.2015.10.003>.
- Hata, M., Takakura, S., Matsushima, N., Hashimoto, T., & Utsugi, M. (2016). Crustal magma pathway beneath Aso caldera inferred from three-dimensional electrical resistivity structure.

- Hotta, K., Iguchi, M., Ohkura, T., Hendrasto, M., Gunawan, H., Rosadi, U., & Kriswati, E. (2019). Magma intrusion and effusion at Sinabung volcano, Indonesia, from 2013 to 2016, as revealed by continuous GPS observation. *Journal of Volcanology and Geothermal Research*, 382, 173–183. <https://doi.org/10.1016/j.jvolgeores.2017.12.015>.
- Hotta, K., Iguchi, M., & Tameguri, T. (2016). Rapid dike intrusion into Sakurajima volcano on August 15, 2015, as detected by multi-parameter ground deformation observations. *Earth, Planets and Space*, 68(1). <https://doi.org/10.1186/s40623-016-0450-0>.
- Hyndman, R. D., Vanyan, L. L., Marquis, G., & Law, L. K. (1993). The origin of electrically conductive lower continental crust: saline water or graphite? *Physics of the Earth and Planetary Interiors*, 81(1–4), 325–345. [https://doi.org/10.1016/0031-9201\(93\)90139-Z](https://doi.org/10.1016/0031-9201(93)90139-Z).
- Kagiyama, T., Utada, H., & Yamamoto, T. (1999). Magma ascent beneath Unzen Volcano, SW Japan, deduced from the electrical resistivity structure. *Journal of Volcanology and Geothermal Research*, 89(1–4), 35–42. [https://doi.org/10.1016/S0377-0273\(98\)00120-6](https://doi.org/10.1016/S0377-0273(98)00120-6).
- Kita, I., Nagao, K., Taguchi, S., & Hasegawa, H. (1993). Emission of magmatic He with different $^3\text{He}/^4\text{He}$ ratios from the Unzen volcanic area, Japan. *Geochemical Journal*, 27, 251–259. <https://doi.org/10.2343/geochemj.27.251>.
- Kohno, Y., Matsushima, T., & Shimizu, H. (2008). Pressure sources beneath Unzen Volcano inferred from leveling and GPS data. *Journal of Volcanology and Geothermal Research*, 175(1–2), 100–109. <https://doi.org/10.1016/j.jvolgeores.2008.03.022>.
- Komori, S., Kagiyama, T., Utsugi, M., Inoue, H., & Azuhata, I. (2013). Two-dimensional resistivity structure of Unzen Volcano revealed by AMT and MT surveys. *Earth, Planets and Space*, 65(7), 759–766. <https://doi.org/10.5047/eps.2012.10.005>.
- Koulakov, I., Kasatkina, E., Shapiro, N. M., Jaupart, C., Vasilevsky, A., El Khrepy, S., Al-Arifi, N., & Smirnov, S. (2016). The feeder system of the Toba supervolcano from the slab to the shallow reservoir. *Nature Communications*, 7. <https://doi.org/10.1038/ncomms12228>.
- Kukarina, E., West, M., Keyson, L. H., Koulakov, I., Tsibizov, L., & Smirnov, S. (2017). Focused magmatism beneath Uturuncu volcano, Bolivia: Insights from seismic tomography and deformation modeling. *Geosphere*, 13(6), 1855–1866. <https://doi.org/10.1130/GES01403.1>.
- Kuo, L. W., Huang, J. R., Fang, J. N., Si, J., Li, H., & Song, S. R. (2018). Carbonaceous materials in the fault zone of the longmenshan fault belt: 1. Signatures within the deep wenchuan earthquake fault zone and their implications. *Minerals*, 8(9). <https://doi.org/10.3390/min8090385>.

- Lee, B., Unsworth, M., Árnason, K., & Cordell, D. (2020). Imaging the magmatic system beneath the Krafla geothermal field, Iceland: A new 3-D electrical resistivity model from inversion of magnetotelluric data. *Geophysical Journal International*, 220(1), 541–567. <https://doi.org/10.1093/gji/ggz427>.
- Luque, F. J., Ortega, L., Barrenechea, J. F., Huizenga, J. M., & Millward, D. (2012). Key factors controlling massive graphite deposition in volcanic settings: An example of a self-organized critical system. *Journal of the Geological Society*, 169(3), 269–277. <https://doi.org/10.1144/0016-76492011-069>.
- Magee, C., Stevenson, C. T. E., Ebmeier, S. K., Keir, D., Hammond, J. O. S., Gottsmann, J. H., Whaler, K. A., Schofield, N., Jackson, C. A. L., Petronis, M. S., O'Driscoll, B., Morgan, J., Cruden, A., Vollgger, S. A., Dering, G., Micklethwaite, S., & Jackson, M. D. (2018). Magma plumbing systems: A geophysical perspective. *Journal of Petrology*, 59(6), 1217–1251. <https://doi.org/10.1093/petrology/egy064>.
- Matsumoto, S., Shimizu, H., Onishi, M., & Uehira, K. (2012). Seismic reflection survey of the crustal structure beneath Unzen volcano, Kyushu, Japan. *Earth, Planets and Space*, 64(5), 405–414. <https://doi.org/10.5047/eps.2011.11.006>.
- Miyano, K., Aizawa, K., Matsushima, T., Shito, A., & Shimizu, H. (2021). Seismic velocity structure of the Unzen volcano, Japan, and its relationship to the magma ascent route for the 1990-1995 eruptions. *submitted to Scientific Reports (in revision)*.
- Mogi, K. (1958). Relations between the eruptions of various volcanoes and the deformations of the ground surface around them, *Bull. Earthquake Res. Inst. Univ. Tokyo*, 36, 99–134.
- Munoz, G., & Ritter, O. (2013). Pseudo-remote reference processing of magnetotelluric data : a fast and efficient data acquisition scheme for local arrays. *Geophysical Prospecting* 61, 300–316. <https://doi.org/10.1111/1365-2478.12012>
- Morikawa, N., Kazahaya, K., Fourre, E., Takahashi, H. A., Jean-Baptiste, P., Ohwada, M., LeGuern, F. J., & Nakama, A. (2008). Magmatic He distribution around Unzen volcano inferred from intensive investigation of helium isotopes in groundwater. *Journal of Volcanology and Geothermal Research*, 175(1–2), 218–230. <https://doi.org/10.1016/j.jvolgeores.2008.03.038>.
- Nakada, S., Shimizu, H., & Ohta, K. (1999). Overview of the 1990-1995 eruption at Unzen Volcano. *Journal of Volcanology and Geothermal Research*, 89(1–4), 1–22. [https://doi.org/10.1016/S0377-0273\(98\)00118-8](https://doi.org/10.1016/S0377-0273(98)00118-8)
- Nakada, S., & Motomura, Y. (1999). Petrology of the 1991-1995 eruption at Unzen: Effusion pulsation and groundmass crystallization. *Journal of Volcanology and Geothermal Research*, 89(1–4), 173–196. [https://doi.org/10.1016/S0377-0273\(98\)00131-0](https://doi.org/10.1016/S0377-0273(98)00131-0)

- Nakada, S., Uto, K., Sakuma, S., Eichelberger, J. C., & Shimizu, H. (2005). Scientific Results of Conduit Drilling in the Unzen Scientific Drilling Project (USDP). *Scientific Drilling*, 1(October 2014), 18–22. <https://doi.org/10.5194/sd-1-18-2005>.
- Nesbitt, B. E. (1993). Resistivities of Crustal Fluids. *Journal of Geophysical Research: Solid Earth*, 98(9), 4301–4310.
- Nishi, K. (2002). Three-dimensional Seismic Velocity Structure beneath Unzen Volcano, Kyushu, Japan Inferred by Tomography from Experimental Explosion Data. *Bulletin of the Volcanological Society of Japan*, 47(4), 227–241. https://doi.org/10.18940/kazan.47.4_227
- Nishimura, K., Kawamoto, T., Kobayashi, T., Sugimoto, T., & Yamashita, S. (2005). Melt inclusion analysis of the Unzen 1991-1995 dacite: Implications for crystallization processes of dacite magma. *Bulletin of Volcanology*, 67(7), 648–662. <https://doi.org/10.1007/s00445-004-0400-8>.
- Oohashi, K., Hirose, T., Kobayashi, K., & Shimamoto, T. (2012). The occurrence of graphite-bearing fault rocks in the Atotsugawa fault system, Japan: Origins and implications for fault creep. *Journal of Structural Geology*, 38, 39–50. <https://doi.org/10.1016/j.jsg.2011.10.011>.
- Ozeki, N., Okuno, M., & Kobayashi, T. (2005). Growth History of Mayuyama, Unzen Volcano, Kyushu, Southwest Japan. 火山. 441-454. 10.18940/kazan.50.6_441. In Japanese with English abstract
- Pritchard, M. E., & Simons, M. (2004). An InSAR-based survey of volcanic deformation in the central Andes. *Geochemistry, Geophysics, Geosystems*, 5(2), 1–42. <https://doi.org/10.1029/2003GC000610>.
- Lundstrom, C. C., & Glazner, A. F. (2016). Silicic magmatism and the volcanic-plutonic connection. *Elements*, 12(2), 91–96. <https://doi.org/10.2113/gselements.12.2.91>
- Luque, F. J., Huizenga, J. M., Crespo-Feo, E., Wada, H., Ortega, L., & Barrenechea, J. F. (2014). Vein graphite deposits: Geological settings, origin, and economic significance. *Mineralium Deposita*, 49(2), 261–277. <https://doi.org/10.1007/s00126-013-0489-9>.
- Rung-arunwan, T., Siripunvaraporn, W., & Utada, H. (2016). On the Berdichevsky average. *Physics of the Earth And Planetary Interiors*, 253, 1–4. <https://doi.org/10.1016/j.pepi.2016.01.006>
- Sakuma, S., Kajiwar, T., Nakada, S., Uto, K., & Shimizu, H. (2008). Drilling and logging results of USDP-4 - Penetration into the volcanic conduit of Unzen Volcano, Japan. *Journal of Volcanology and Geothermal Research*, 175(1–2), 1–12. <https://doi.org/10.1016/j.jvolgeores.2008.03.039>.
- Samrock, F., Grayver, A. V., Eysteinnsson, H., & Saar, M. O. (2018). Magnetotelluric Image of Transcrustal Magmatic System Beneath the Tulu Moye Geothermal Prospect in the Ethiopian

- Rift. *Geophysical Research Letters*, 45(23), 12,847-12,855. <https://doi.org/10.1029/2018GL080333>.
- Sato, H., Holtz, F., Botcharnikov, R. E., & Nakada, S. (2017). Intermittent generation of mafic enclaves in the 1991–1995 dacite of Unzen Volcano recorded in mineral chemistry. *Contributions to Mineralogy and Petrology*, 172(4), 1–19. <https://doi.org/10.1007/s00410-017-1335-3>.
- Schmincke, H.U. (2004). *Volcanism*. Springer: Berlin.
- Segall, P. (2019). Magma chambers: What we can, and cannot, learn from volcano geodesy. *Philosophical Transactions of the Royal Society A: Mathematical, Physical and Engineering Sciences*, 377(2139). <https://doi.org/10.1098/rsta.2018.0158>.
- Shinohara, H. (2007). Excess degassing from volcanoes and its role on eruptive and intrusive activity. *Reviews of Geophysics*, 46(4), 1–31. <https://doi.org/10.1029/2007RG000244>.
- Simpson, F. & Bahr, K. (2005). *Practical Magnetotellurics*. Cambridge University Press.
- Siripunvaraporn, W., Egbert, G., & Uyeshima, M. (2005). Interpretation of two-dimensional magnetotelluric profile data with three-dimensional inversion: Synthetic examples. *Geophysical Journal International*, 160(3), 804–814. <https://doi.org/10.1111/j.1365-246X.2005.02527.x>.
- Siripunvaraporn, W., & Egbert, G. (2009). WSINV3DMT: Vertical magnetic field transfer function inversion and parallel implementation. *Physics of the Earth and Planetary Interiors*, 173(3–4), 317–329. <https://doi.org/10.1016/j.pepi.2009.01.013>.
- Sparks, R. S. J., Annen, C., Blundy, J. D., Cashman, K. V., Rust, A. C., & Jackson, M. D. (2019). Formation and dynamics of magma reservoirs. *Philosophical Transactions of the Royal Society A: Mathematical, Physical and Engineering Sciences*, 377(2139). <https://doi.org/10.1098/rsta.2018.0019>.
- Srigitomo, W., Kagiya, T., Kanda, W., Munekane, H., Hashimoto, T., Tanaka, Y., Utada, H., & Utsugi, M. (2008). Resistivity structure of Unzen Volcano derived from time domain electromagnetic (TDEM) survey. *Journal of Volcanology and Geothermal Research*, 175(1–2), 231–240. <https://doi.org/10.1016/j.jvolgeores.2008.03.033>.
- Sugimoto, T., Ishibashi, H., Wakamatsu, S., & Yanagi, T. (2005). Petrologic evolution of Pre-Unzen and Unzen magma chambers beneath the Shimabara Peninsula, Kyushu, Japan: Evidence from petrography and bulk rock chemistry. *Geochemical Journal*, 39(3), 241–256. <https://doi.org/10.2343/geochemj.39.241>.
- Takei, Y. (2002). Effect of pore geometry on V_P / V_S : From equilibrium geometry to crack. *Journal of Geophysical Research*, 107(B2). <https://doi.org/10.1029/2001jb000522>

- Telford, W.M., Geldart, L.P., Sherrif, R.E. (1990). *Applied Geophysics: Second Edition. Cambridge University Press.*
- Tibaldi, A., Bonali, F. L., & Corazzato, C. (2017). Structural control on volcanoes and magma paths from local- to orogen-scale: The central Andes case. *Tectonophysics*, 699, 16–41. <https://doi.org/10.1016/j.tecto.2017.01.005>
- Tikhonov, A.N. (1950). The determination of the electrical properties of deep layers of the Earth's crust. *Doklady*, 73(2): 295-297.
- Tretner, A., Zimmer, M., Erzinger, J., Nakada, S., & Saito, M. (2008). Real-time drill mud gas logging at the USDP-4 drilling, Unzen volcano, Japan. *Journal of Volcanology and Geothermal Research*, 175(1–2), 28–34. <https://doi.org/10.1016/j.jvolgeores.2008.03.031>
- Triahadini, A., Aizawa, K., Teguri, Y., Koyama, T., Tsukamoto, K., Muramatsu, D., Chiba, K., & Uyeshima, M. (2019). Magnetotelluric transect of Unzen graben, Japan: conductors associated with normal faults. *Earth, Planets and Space*, 71(1). <https://doi.org/10.1186/s40623-019-1004-z>.
- Tseng, K. H., Ogawa, Y., Nurhasan, Tank, S. B., Ujihara, N., Honkura, Y., Terada, A., Usui, Y., & Kanda, W. (2020). Anatomy of active volcanic edifice at the Kusatsu–Shirane volcano, Japan, by magnetotellurics: hydrothermal implications for volcanic unrests. *Earth, Planets and Space*, 72(1). <https://doi.org/10.1186/s40623-020-01283-2>
- Tsukamoto, K., Aizawa, K., Chiba, K., Kanda, W., Uyeshima, M., Koyama, T., Utsugi, M., Seki, K., & Kishita, T. (2018). Three-Dimensional Resistivity Structure of Iwo-Yama Volcano, Kirishima Volcanic Complex, Japan: Relationship to Shallow Seismicity, Surface Uplift, and a Small Phreatic Eruption. *Geophysical Research Letters*, 45(23), 12,821-12,828. <https://doi.org/10.1029/2018GL080202>
- Umakoshi, K., Shimizu, H., & Matsuwo, N. (2001). Volcano-tectonic seismicity at Unzen Volcano. *Journal of Volcanology and Geothermal Research*, 112, 117–131.
- Ussher, G., Harvey, C., Johnstone, R., Anderson, E., & Zealand, N. (2000). Understanding the resistivities observed in geothermal systems. *Proceedings World Geothermal Congress*, 1915–1920.
- Vanyan, L., Tezkan, B., & Palshin, N. (2001). Low electrical resistivity and seismic velocity at the base of the upper crust as indicator of rheologically weak layer. *Surveys in Geophysics*, 22(2), 131–154. <https://doi.org/10.1023/A:1012937410685>.
- Waff, H.S. (1974). Theoretical considerations of electrical conductivity in a partially molten mantle and implications for geothermometry. *Journal of Geophysical Research*, 79 : 4003-4010.
- Wespestad, C. E., Thurber, C. H., Andersen, N. L., Singer, B. S., Cardona, C., Zeng, X., Bennington, N. L., Keranen, K., Peterson, D. E., Cordell, D., Unsworth, M., Miller, C., &

- Williams-Jones, G. (2019). Magma Reservoir Below Laguna del Maule Volcanic Field, Chile, Imaged with Surface-Wave Tomography. *Journal of Geophysical Research: Solid Earth*, 124(3), 2858–2872. <https://doi.org/10.1029/2018JB016485>.
- Widiyantoro, S., Ramdhan, M., Métaxian, J. P., Cummins, P. R., Martel, C., Erdmann, S., Nugraha, A. D., Budi-Santoso, A., Laurin, A., & Fahmi, A. A. (2018). Seismic imaging and petrology explain highly explosive eruptions of Merapi Volcano, Indonesia. *Scientific Reports*, 8(1), 1–7. <https://doi.org/10.1038/s41598-018-31293-w>.
- Yoshimura, R., Ogawa, Y., Yukutake, Y., Kanda, W., Komori, S., Hase, H., Goto, T. nori, Honda, R., Harada, M., Yamazaki, T., Kamo, M., Kawasaki, S., Higa, T., Suzuki, T., Yasuda, Y., Tani, M., & Usui, Y. (2018). Resistivity characterisation of Hakone volcano, Central Japan, by three-dimensional magnetotelluric inversion. *Earth, Planets and Space*, 70(1), 1–10. <https://doi.org/10.1186/s40623-018-0848-y>.
- Yuasa, Y., Matsumoto, S., Nakao, S., Matsushima, T., & Ohkura, T. (2020). Inelastic strain rate and stress fields in and around an aseismic zone of Kyushu Island, Japan, inferred from seismic and GNSS data. *Geophysical Journal International*, 221(1), 289–304. <https://doi.org/10.1093/gji/ggaa008>.
- Yukutake, Y., Abe, Y., Honda, R., & Sakai, S. (2021). Magma Reservoir and Magmatic Feeding System Beneath Hakone Volcano, Central Japan, Revealed by Highly Resolved Velocity Structure. *Journal of Geophysical Research: Solid Earth*, 126(4), 1–18. <https://doi.org/10.1029/2020JB021236>.

Supplementary Materials

A. Sounding curves of the sites

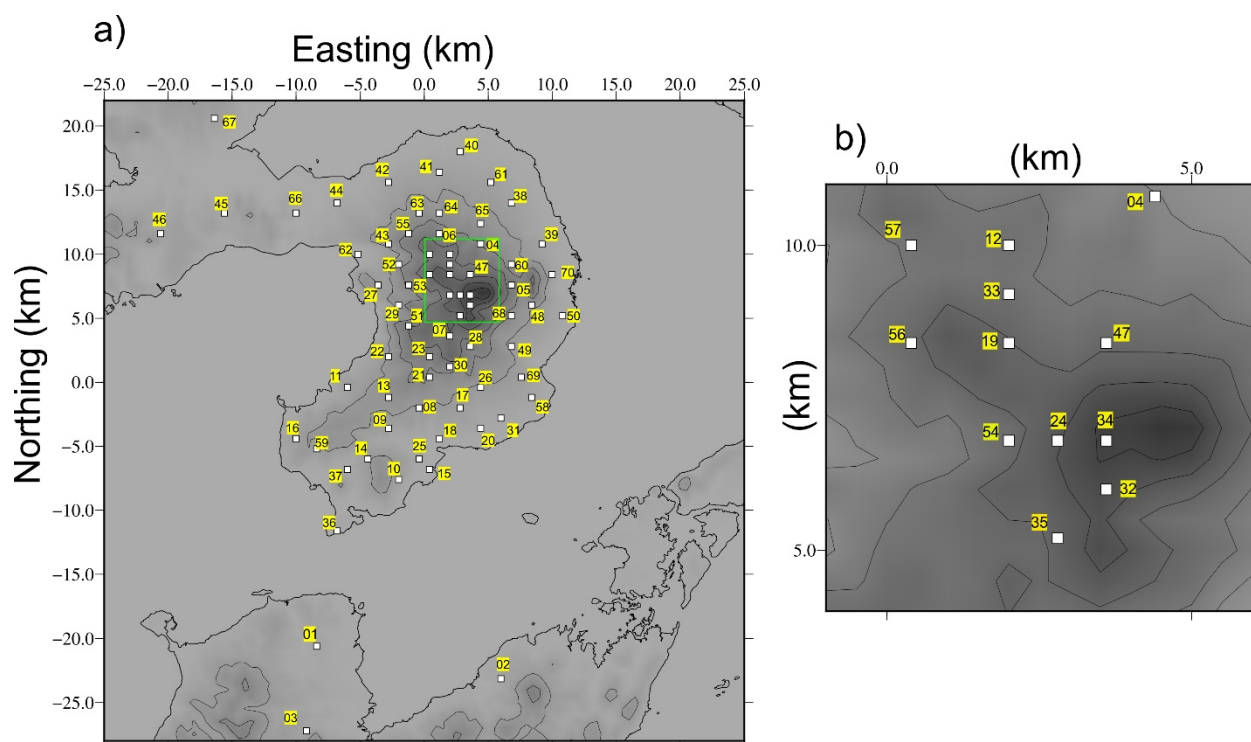
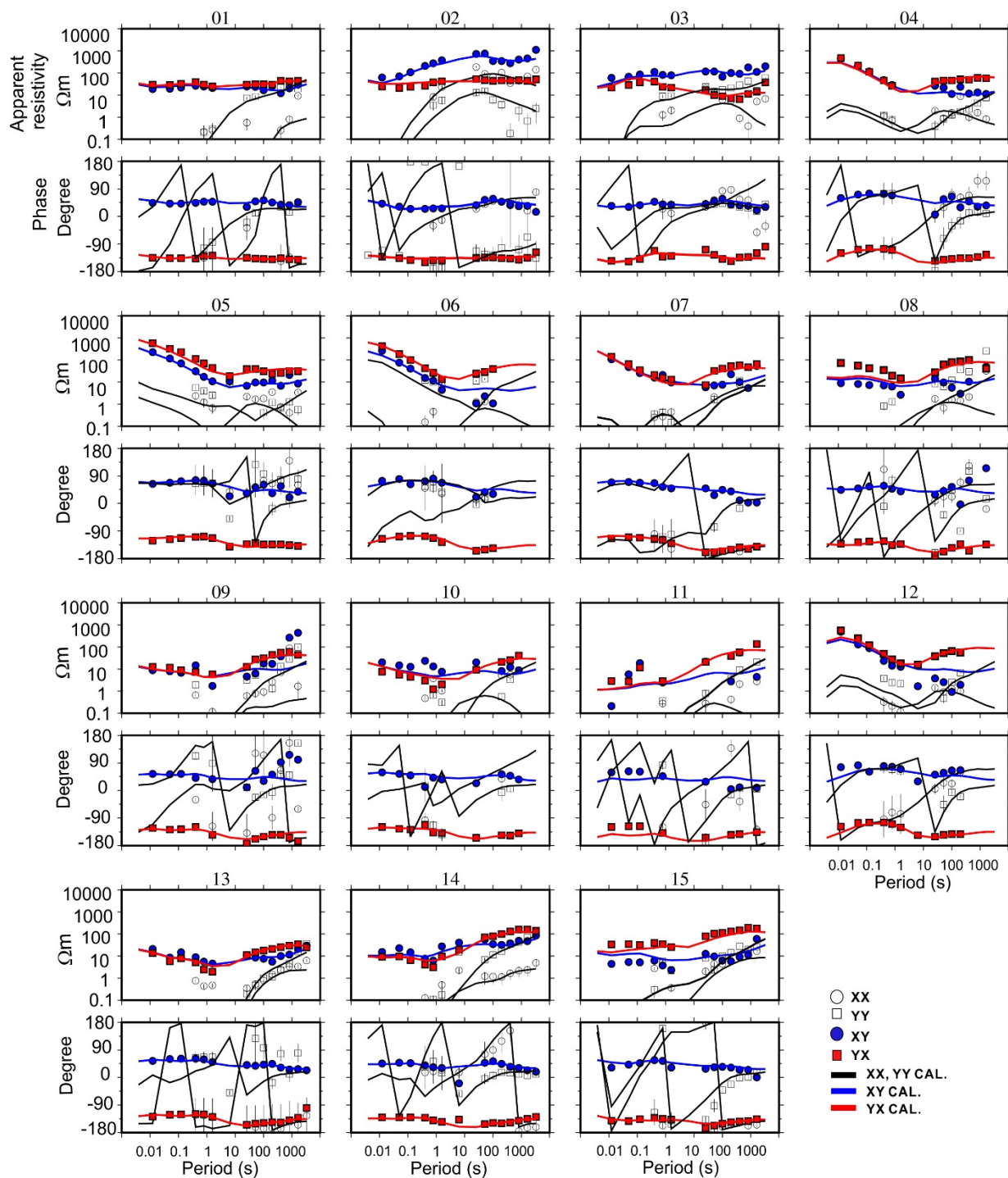
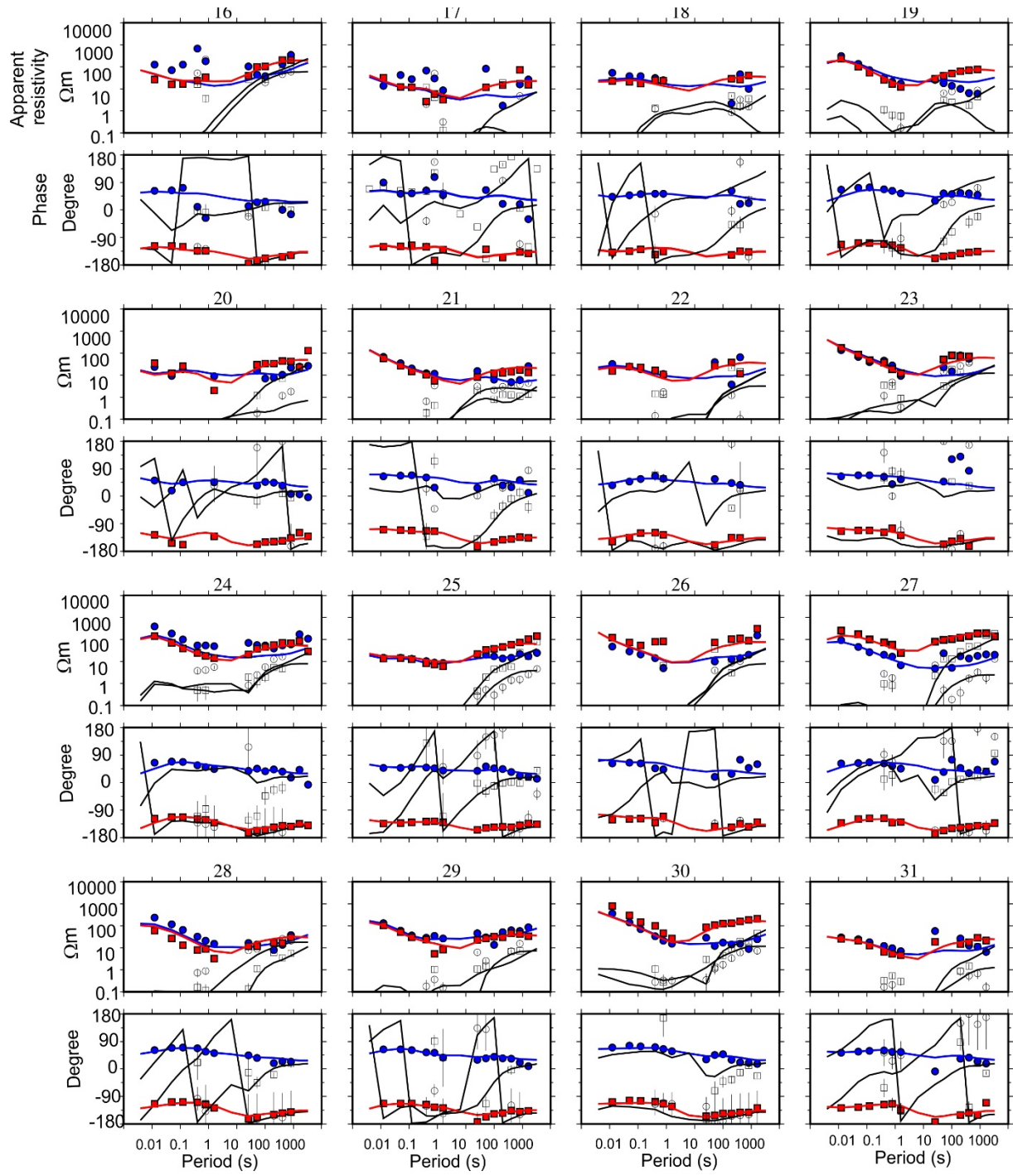
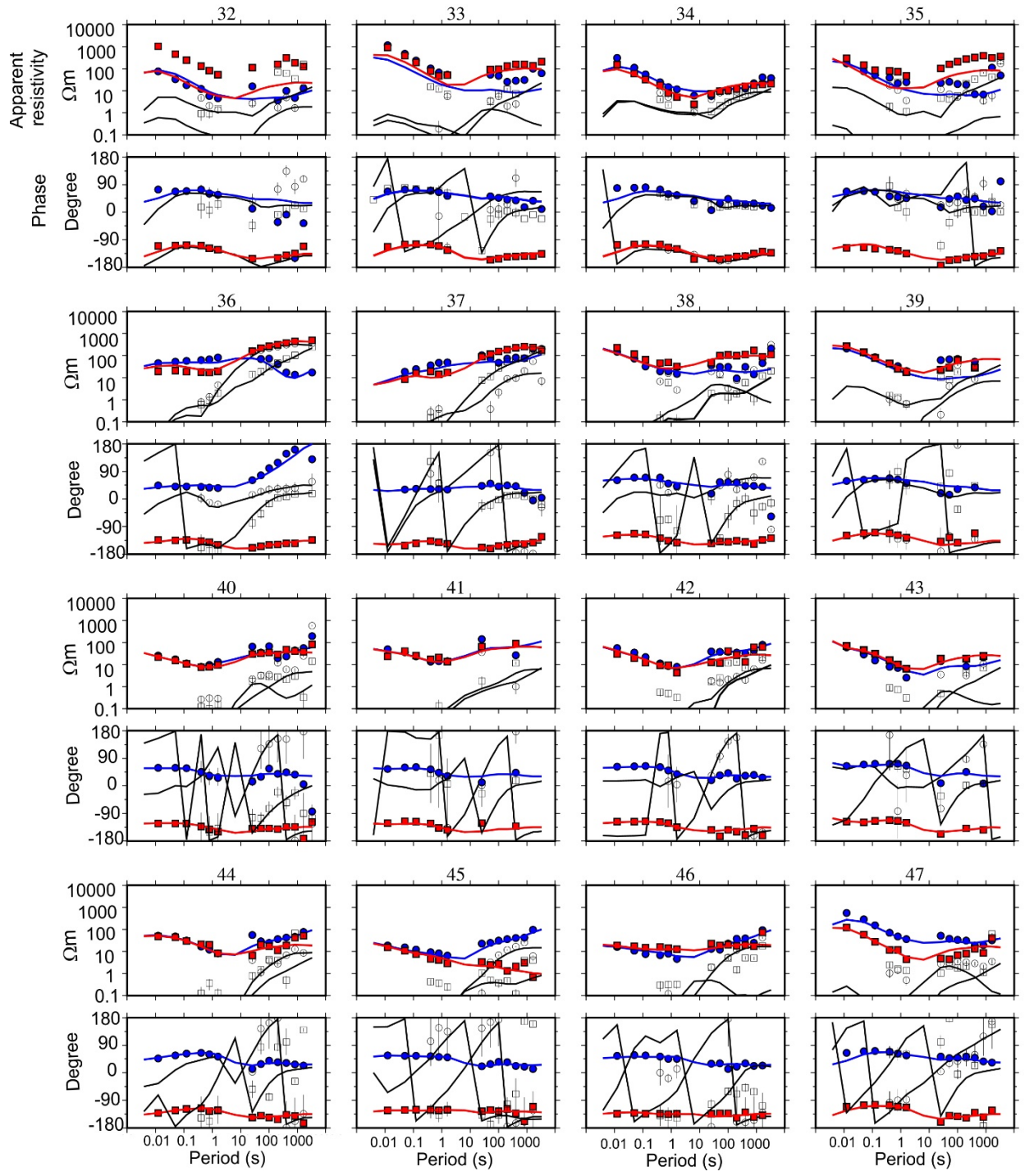
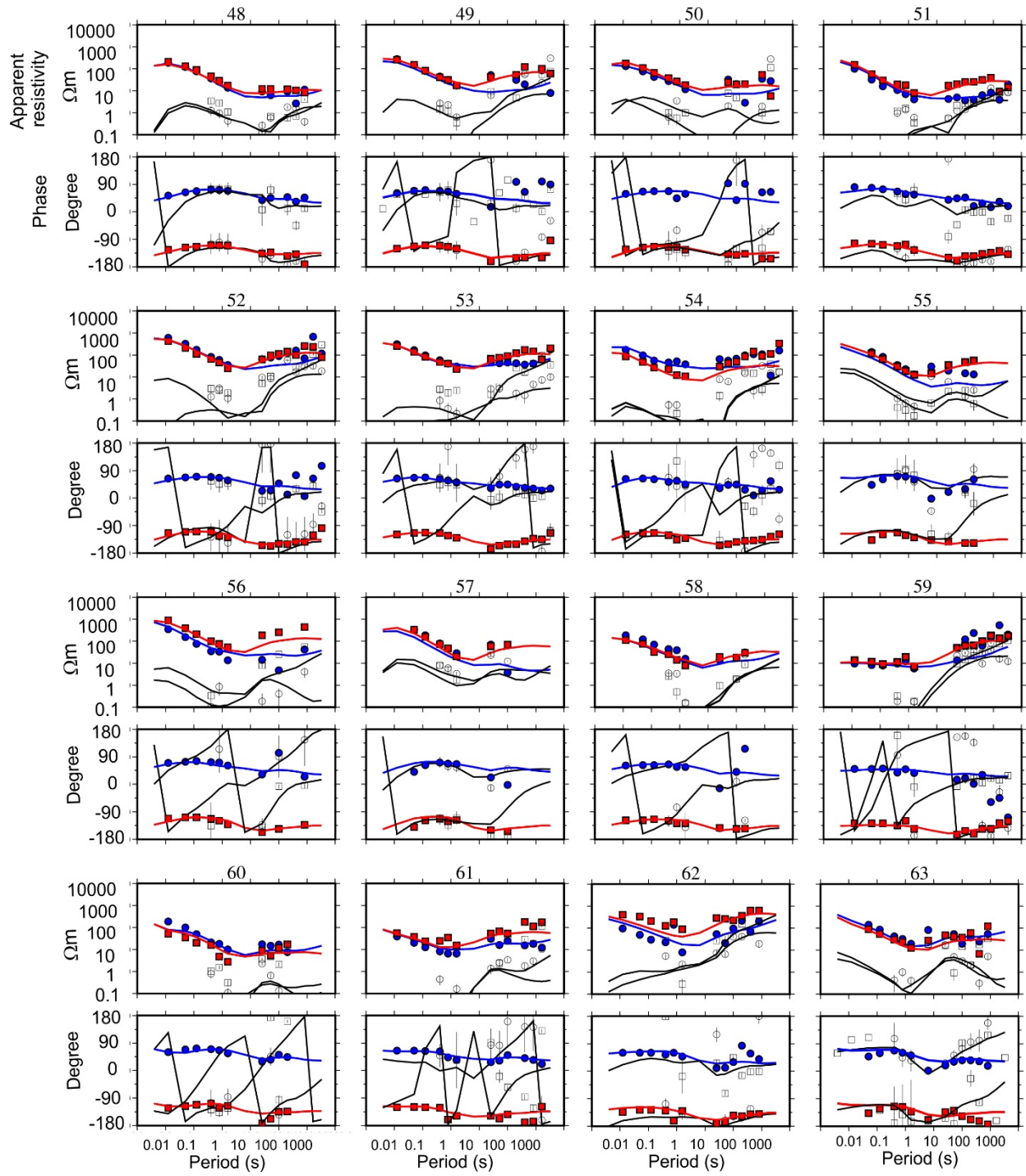


Figure S1. a) Sites location and names in Shimabara Peninsula and Amakusa area that were used in the calculation. b) Sites that are located in the summit of Unzen and the flank area and are enclosed by green rectangle in a).









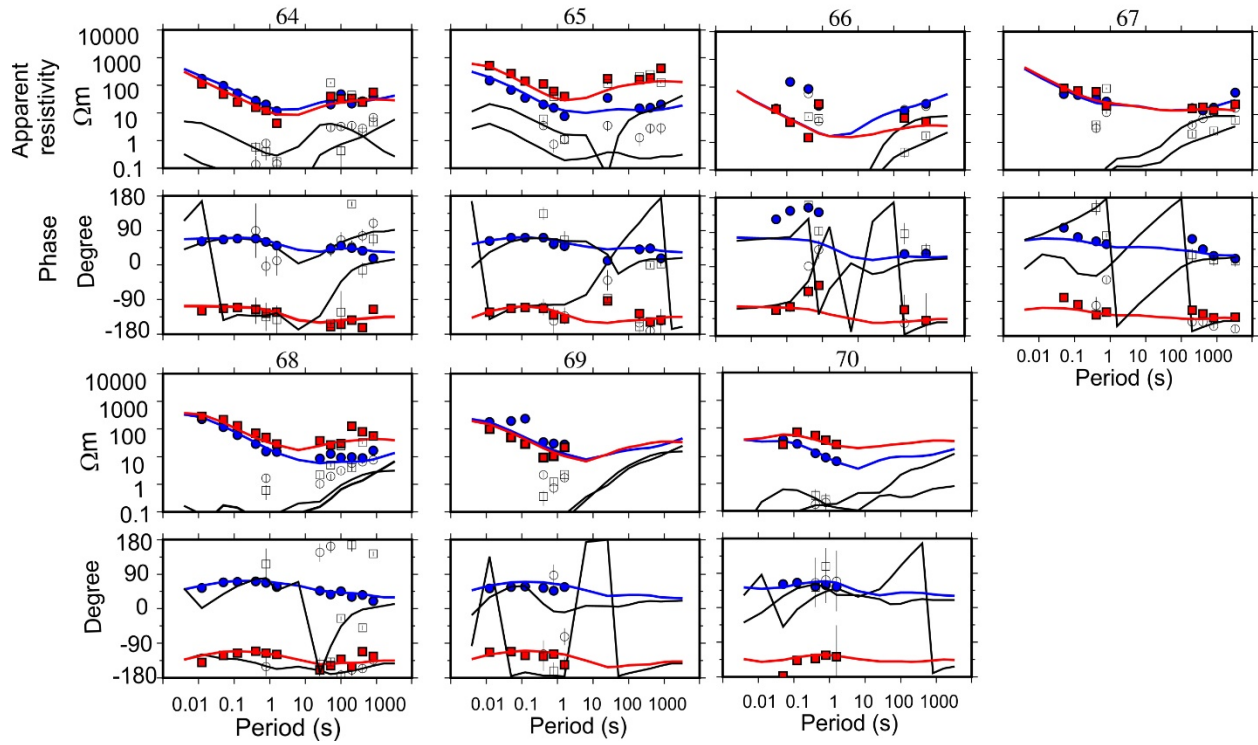
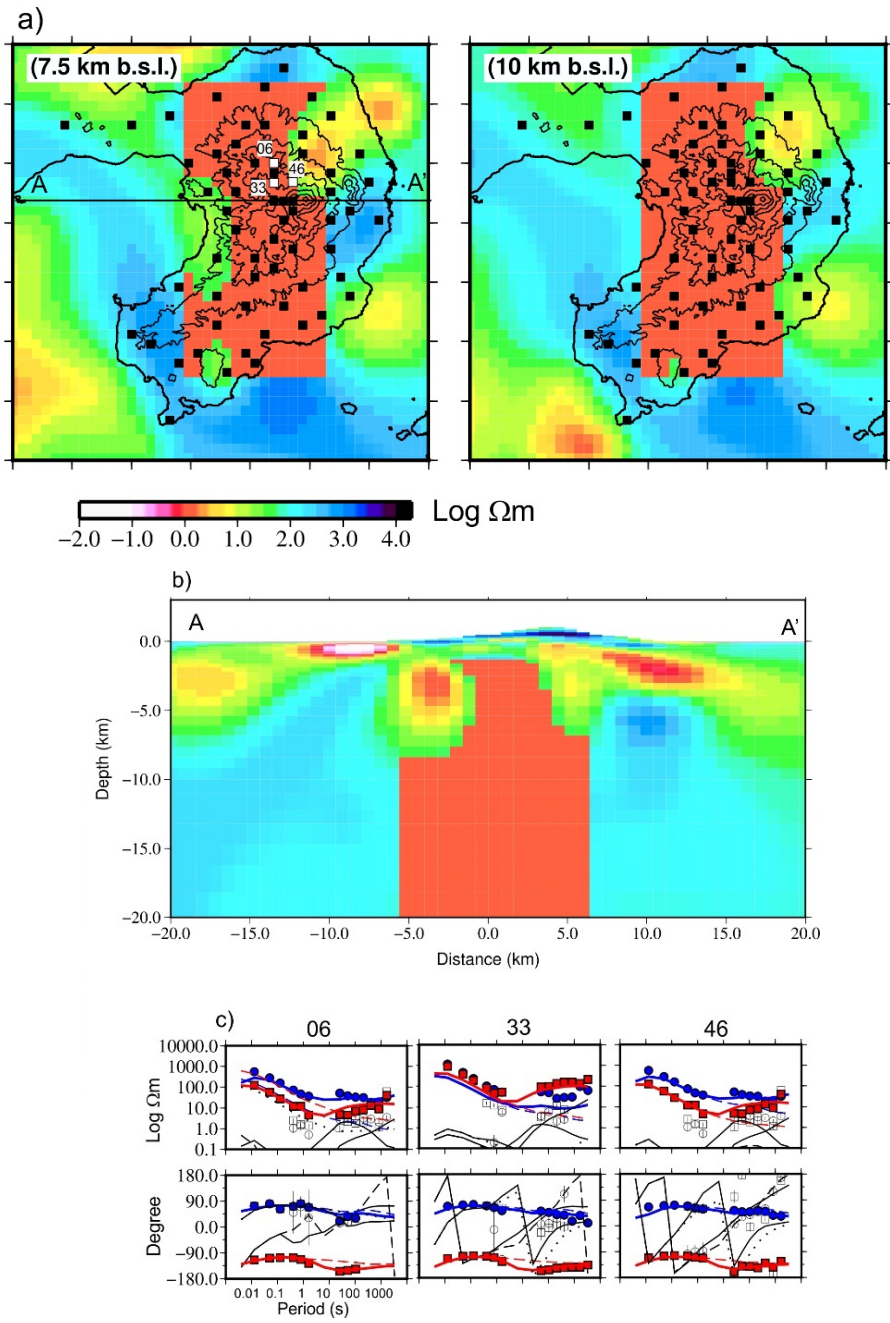


Figure S2. Sounding curves of all inverted MT stations in Shimabara Peninsula. Apparent resistivity and phase from four impedances components are plotted. In the corresponding periods used in the inversion, the poor quality data are excluded in the calculation. The legend of the symbols are written in the figure.

B. Sensitivity test of the anomalies



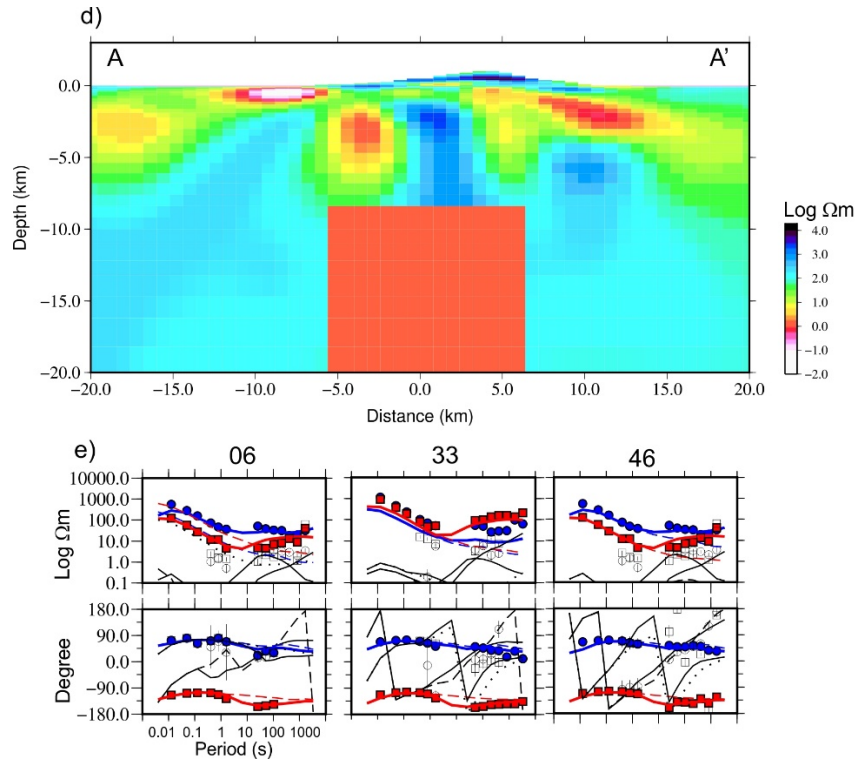


Figure S3. Sensitivity test for resistivity anomaly R1. In the area R1, the resistivity value larger than 55 Ωm was modified by lower resistivities, such as 1 Ωm and forward model was run. a) The modified area in horizontal view, b) The modified area in A-A' vertical profile, c) Sounding curves from selected sites (the sites location are presented as white rectangle in a), with the apparent resistivity and phase from modified model are as dashed lines. The legend for the symbols and lines in sounding curves refer to FS1. Modification R1 to 1 Ωm increased the RMS to 2.07 from the original model 1.50. d) The A-A' profile with area below 8 km to 20 km bsl was modified by low resistivity. For this case, the RMS increased to 1.57. Replacing the same area by 50 Ωm also increased the RMS to 1.53 that shows lower constraint in those depth than in the shallower depth. e) Sounding curves of same sites as part c). The sensitivity test result indicates that R1 is needed by the original model.

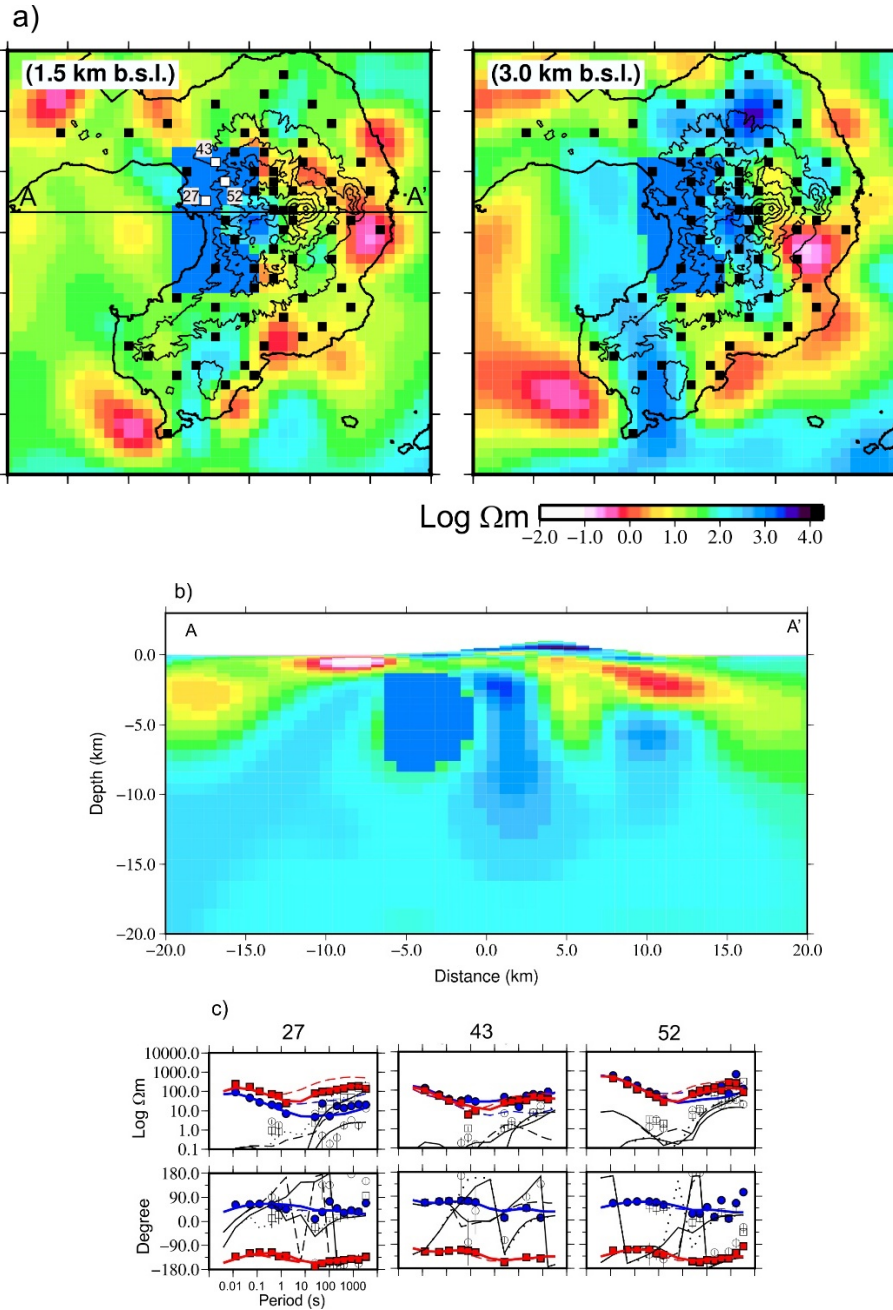


Figure S4. Sensitivity test for resistivity anomaly C1. In the area C1, the resistivity value smaller than 50 Ωm was modified by higher resistivities, such as 1000 Ωm and forward model was run. a) The modified area in horizontal view, b) The modified area in A-A' vertical profile, c) Sounding curves from selected sites (the sites location are presented as white rectangle in a), with the apparent resistivity and phase from modified model are as dashed lines. The legend for the symbols and lines in sounding curves refer to FS1. From modification of C1 to 1000 Ωm , the RMS is increased to 1.65 from the original model 1.50. Replacing C1 by 100 Ωm also increased the RMS to 1.61. The sensitivity test result indicates that C1 is needed by the original model.

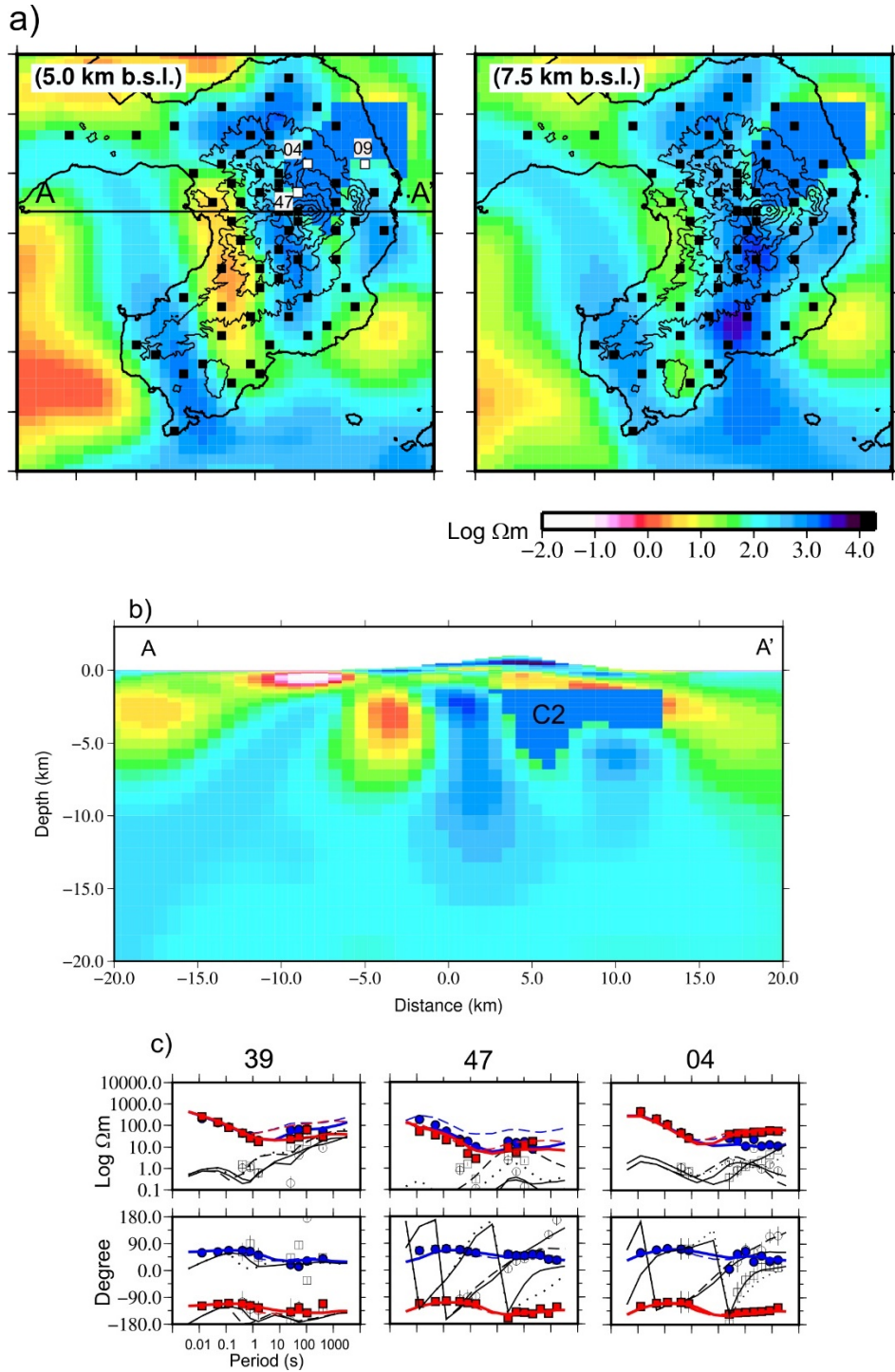


Figure S5. Sensitivity test for resistivity anomaly C2. In the area C2, the resistivity value smaller than 50 Ωm was modified by high resistivity, such as 1000 Ωm and forward model was run. a) The modified area in horizontal view, b) The modified area in A-A' (E-W direction) vertical profile, c) Sounding curves from selected sites (the sites location are presented as white rectangle in a), with the apparent resistivity and phase from modified model are as dashed lines. The legend for the symbols and lines in sounding curves refer to FS1. From modification of C2 to 1000 Ωm , the RMS is increased to 1.68 from original model 1.50. Replacing C2 by 100 Ωm also increased the RMS to 1.74. The sensitivity test result indicates that C2 is needed by the original model.

C. Inversion with varying parameters

Table S1. Varying inversion parameter
(Model 1 is the final model that are discussed in this study)

Model/Figure Number	Smoothing parameter	Intital half space resistivity Ωm	Error floor %	Final RMS
Model 1/ FS6/	τ 10, δx 0.1, δy 0.1, δz 0.1	100	10	1.50
Model 2/FS7	τ 10, δx 0.1, δy 0.1, δz 0.1	100	5	2.01
Model 3/FS8	τ 10, δx 0.1, δy 0.1, δz 0.1	100	15	1.27
Model 4/FS9	τ 5, δx 0.1, δy 0.1, δz 0.1	100	10	1.46
Model 5/ FS10	τ 15, δx 0.1, δy 0.1, δz 0.1	100	10	1.71
Model 6/F11	τ 10, δx 0.1, δy 0.1, δz 0.1	10	10	1.63
Model 7/F12	τ 10, δx 0.1, δy 0.1, δz 0.1	500	10	1,70

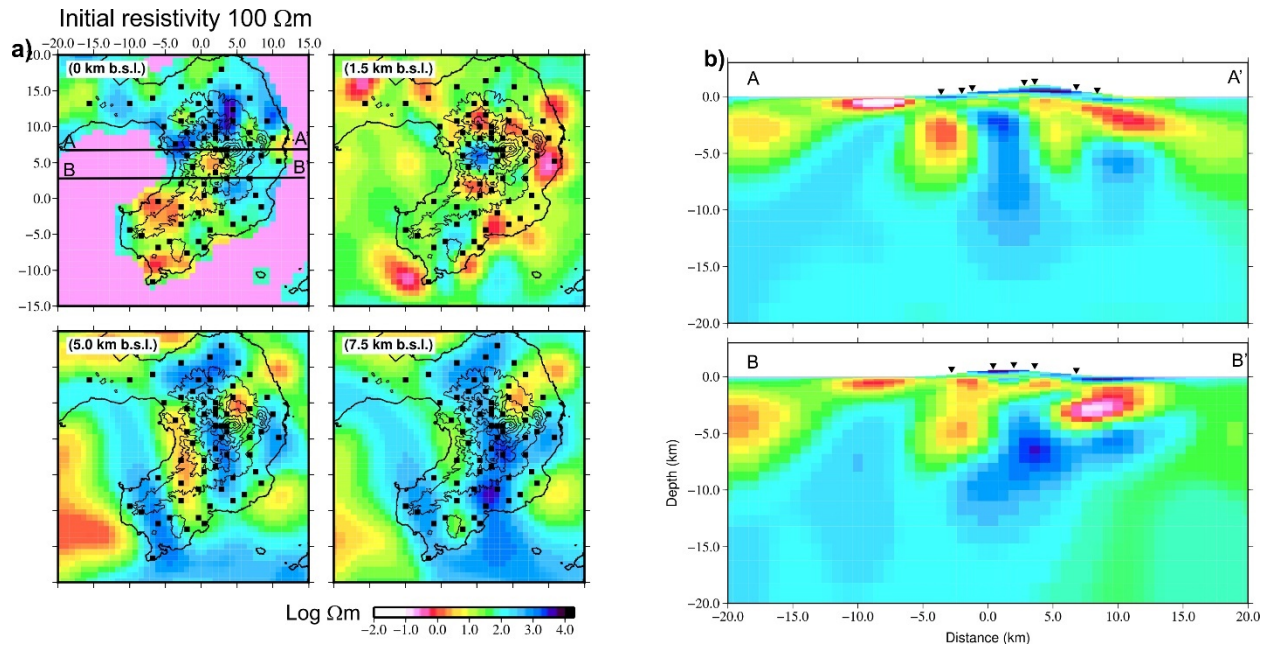
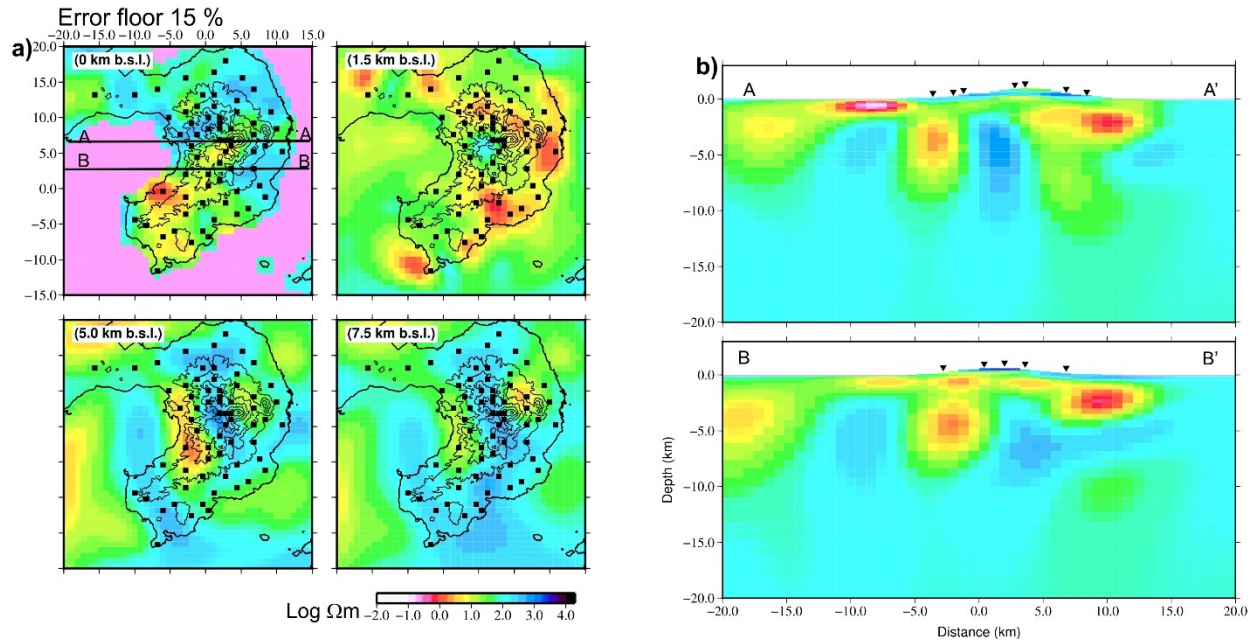
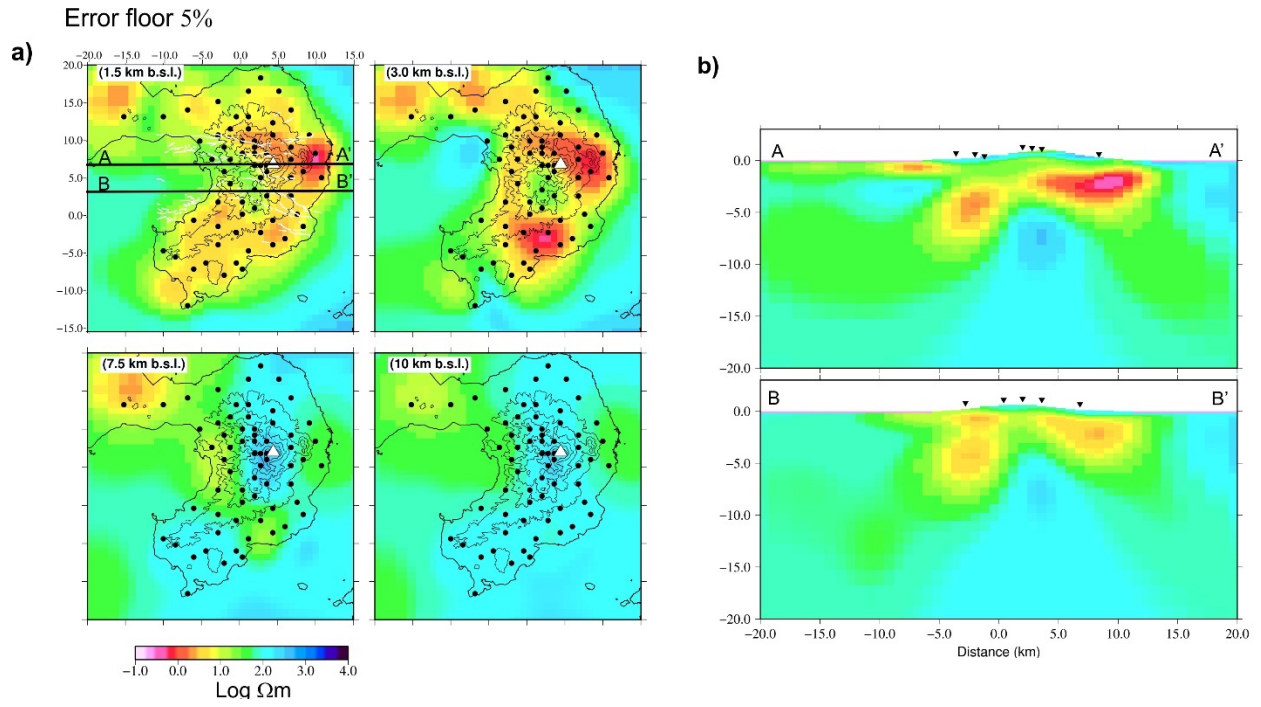


Figure S6. Inversion result using Model 1 parameters as explained in the table S1 (Final model used in this study). a) Resistivity structure in horizontal view., b) resistivity structures in vertical view



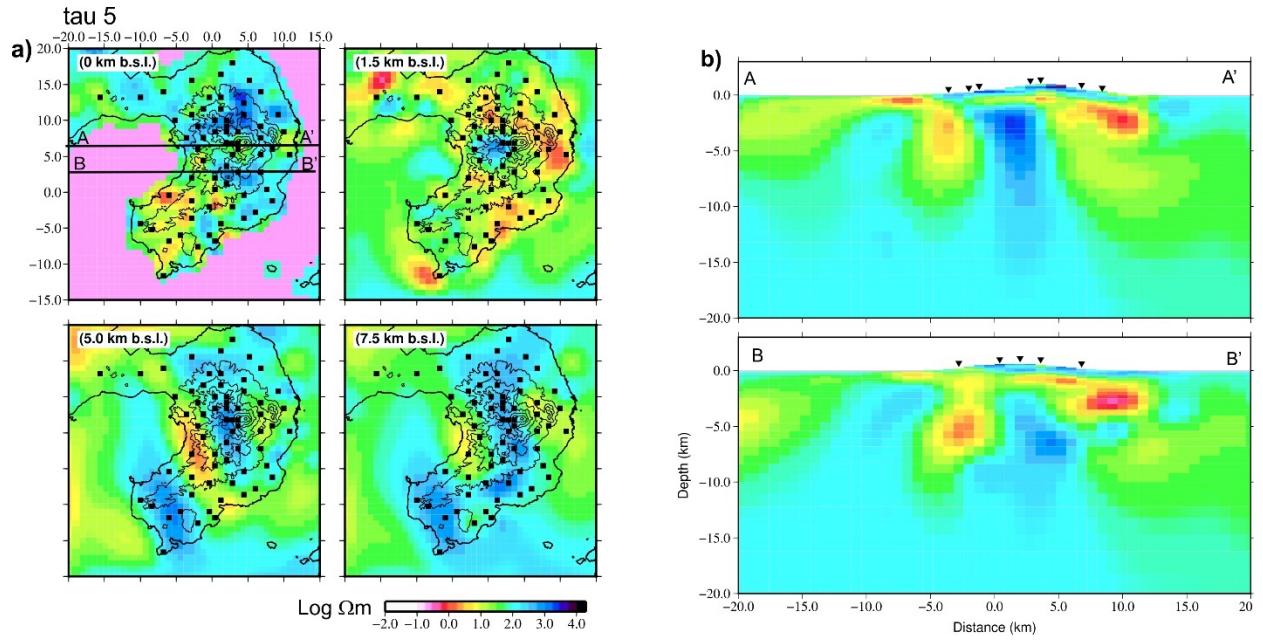


Figure S9. Inversion result using Model 4 parameters as explained in the table S1. a) Resistivity structure in horizontal view., b) resistivity structures in vertical view

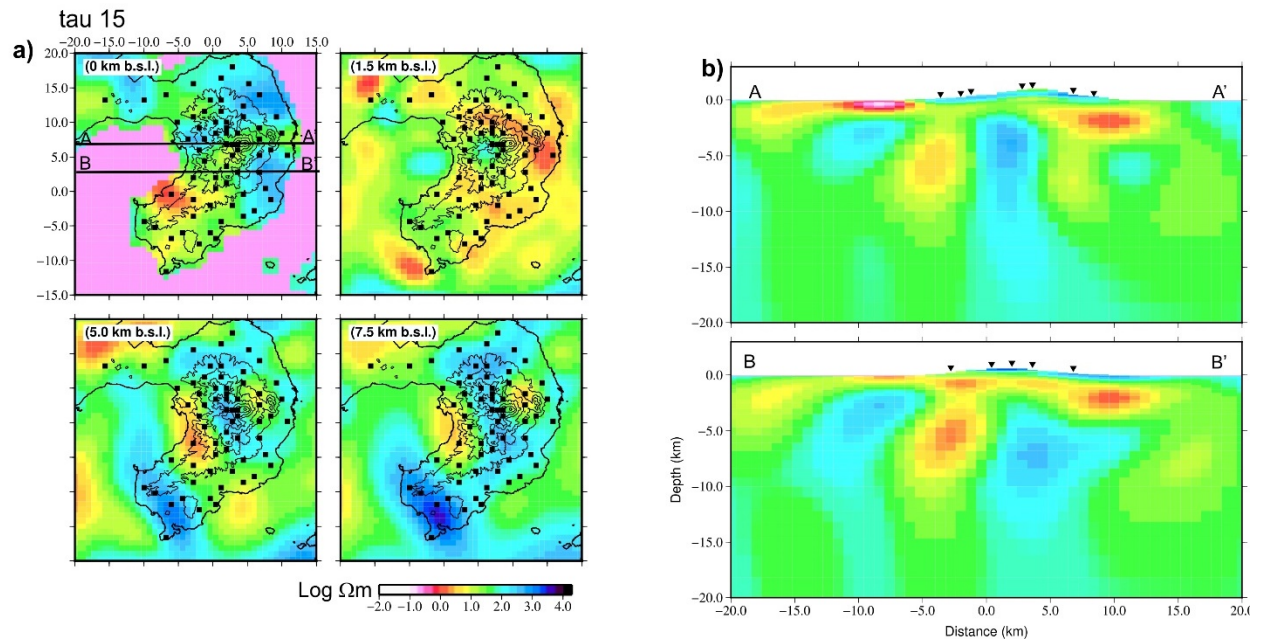


Figure S10. Inversion result using Model 5 parameters as explained in the table S1. a) Resistivity structure in horizontal view., b) resistivity structures in vertical view

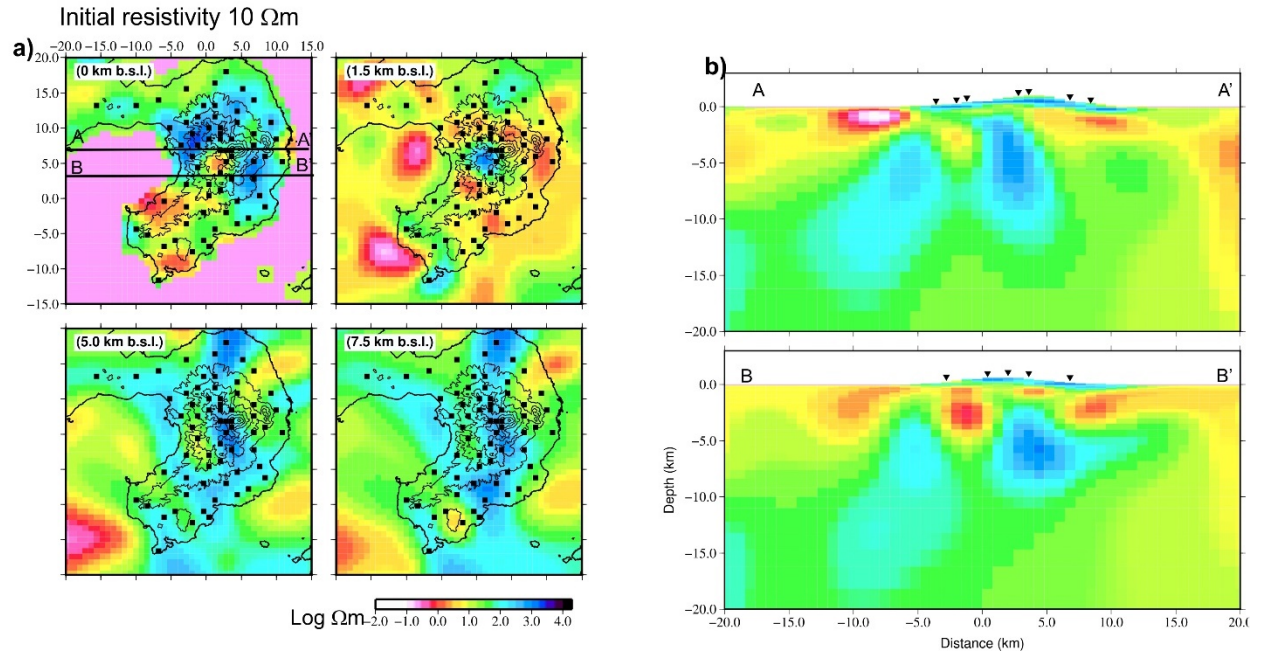


Figure S11. Inversion result using Model 6 parameters as explained in the table S1. a) Resistivity structure in horizontal view., b) resistivity structures in vertical view

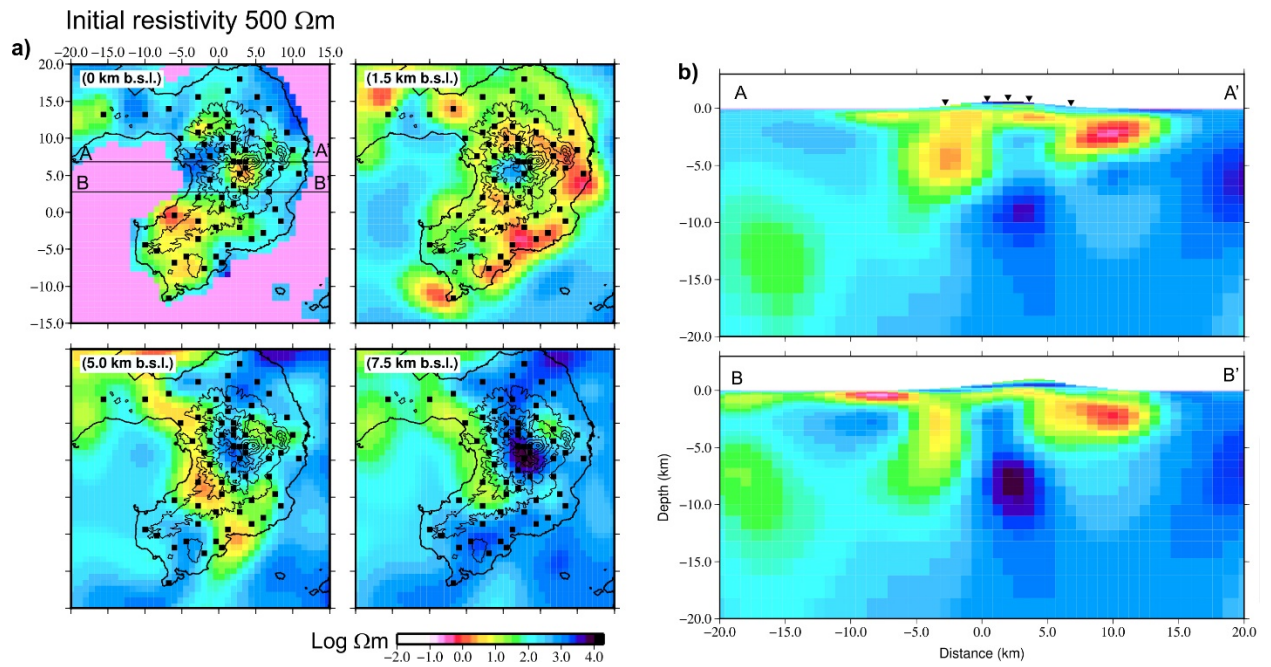


Figure S12. Inversion result using Model 7 parameters as explained in the table S1. a) Resistivity structure in horizontal view., b) resistivity structures in vertical view

D. Calculation of melt fraction using seismic tomography result of Miyano et al.

(Submitted)

Using equation of Dvorkin (2008) (equation 5.2), I tried to calculate melt fraction from Vs structure of Miyano et al. (submitted). The bulk S-wave velocity is influenced by the densities of fluids and the host rock and fluid percentage.

$$V_s = (1 - \phi)^2 V_{Srock} \sqrt{\frac{(1-\phi)\rho_{rock}}{(1-\phi)\rho_{rock} + \phi\rho_{fluid}}} \quad (5.2)$$

V_{Srock} is the Vs for the host rock, ρ_{rock} is the density of the rock, ρ_{fluid} is density of fluid (kg/m^3). I used the slowest absolute Vs from tomography in the area >6 km bsl, that 3.25 km/s. I also used 3.5 km/s for V_{Srock} , 2400 and 2300 kg/m^3 for ρ_{fluid} (andesitic and dacitic melt respectively) and 2750 kg/m^3 for ρ_{rock} (e.g. Comeau et al., 2016; Ichiki et al., 2021). The possible melt fraction if derived from Vs result is $\leq 3\%$, yield very low melt percentage and under similar melt percentage range calculated from R1. However, this result is a very rough estimation since the uncertainties of observed Vs and other parameters of Miyano et al. (submitted).

Liquid compressibility and pore geometry affect Vp/Vs. According to Takei (2002), volume fraction of liquid and the aspect ratio can be deduced from the reduction rate of Vp and Vs resulted from seismic tomography. Yukutake et al (2021) implemented the method of Takei (2002) to estimate the melt fraction of low velocity zone beneath Hakone volcano and yield $\sim 3-4\%$ of melt volume in the Hakone volcano. I use this same approach to calculate melt fraction based on tomography result. The reduction rate of velocity as written in Takei (2002) is

$$\frac{d \ln V_s}{d \ln V_p} = \frac{1 - V_s/V_s^0}{1 - V_p/V_p^0} \quad (5.3)$$

According to the result of Miyano et al (submitted) the region that has low Vp, Vs and higher Vp/Vs is located at the depth ~ 15 km. Using slowest absolute velocity for the same depth level,


gave the velocity values : $V_s = 3.25$ km/s, $V_p = 5.75$ km/s. The reference velocities at the depth V_p^0 and V_s^0 are 95 % of the upper limit velocity at the same depth (Yukutake et al., 2021) and resulted $V_p^0 = 6.17$ km/s and $V_s^0 = 3.56$ km/s. The reduction rate of velocity calculated from equation (5.3) is 1.275. By using figure 5 of Takei (2002) the reduction rate of can be explained by water filled pores or melt filled pores with aspect ratio 0.02-0.04. In the relationship between aspect ratio and liquid volume fraction that is explained in Figure 5 a (Takei 2002), aspect ratio of 0.03 and 0.04 for melt correlates with ~2% and ~4% of melt respectively. Hence, this calculation implies small amount of melt fraction in the low velocity region and support the interpretation of highly crystallized mush zone.

FULL PAPER

Open Access

Magnetotelluric transect of Unzen graben, Japan: conductors associated with normal faults



Agnis Triahadini^{1*} , Koki Aizawa² , Yoshiko Teguri^{2,3}, Takao Koyama⁴ , Kaori Tsukamoto¹ ,
Dan Muramatsu¹ , Keita Chiba²  and Makoto Uyeshima⁴ 

Abstract

We conducted a broadband magnetotelluric (MT) survey along a north–south transect across Unzen graben, Japan. The MT survey line is located ~2 km west of the most recent lava dome and consisted of 27 stations along a 9-km profile. We estimated the 3-D resistivity structure and correlated it with the seismic reflection structure obtained by the same survey line as in the present study. The best-fit resistivity structure shows an upper resistive layer underlain by a moderately conductive layer. The resistive layer, which is interpreted as a cold groundwater zone, is cut by four faults marked by their relatively high conductivity. The underlying layer, which is interpreted as a hydrothermal-water-rich layer, also shows relatively conductive values near the faults. By assuming that the faults are imaged as relatively conductive zones, we infer the dip and depth extent of fracture zones around the faults. Beneath the Chijiwa Fault, which is the longest and most active fault of Unzen graben, the dominant conductor (C1) has a width of 2 km and extends down to below 4 km depth. C1 corresponds to a zone of strong seismic reflection and is located close to one of the pressure sources causing surface deformation. In this study, we interpret C1 as a network of fractures generated by the Chijiwa Fault to which magmatic volatiles are supplied from a deeper pressure source. Given that C1 extends to a greater depth and its resistivity is lower than other conductive zones, it is possible that earthquakes have occurred repeatedly on the Chijiwa Fault. In the center of the study area, we identify a vertically oriented body of high resistivity (R1) that corresponds to a zone of low seismic reflectivity. We interpret R1 as a cooled dyke complex that may have acted as a volcanic conduit.

Keywords: Magnetotellurics, Resistivity structure, Unzen volcano, Normal fault, Chijiwa Fault

Introduction

Unzen volcano, which is located on Shimabara Peninsula, Kyushu, Japan, is known for its remarkable 1991–1995 eruptions that repeatedly generated pyroclastic flows via the collapse of gravitationally unstable, growing lava domes. Before these eruptions, the volcano had been dormant for 198 years (Hoshizumi et al. 1999; Nakada et al. 1999). Seismic and geodetic measurements detected signs of unrest and associated movement of magma (Nishi et al. 1999; Umakoshi et al. 2001; Kohno et al. 2008). The hypocenters of tectonic earthquakes gradually shifted to shallower depths beneath Chijiwa

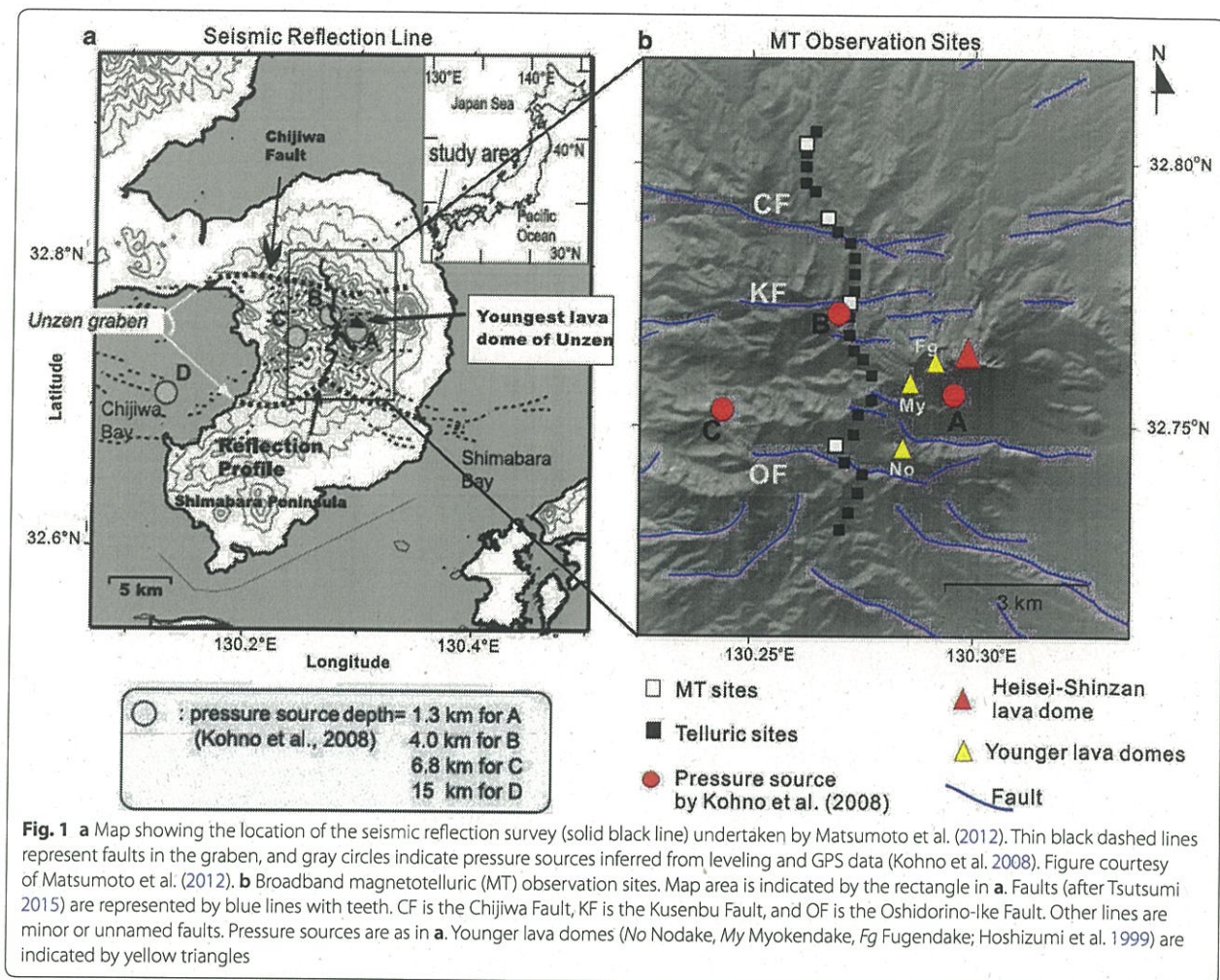
Bay to beneath the summit (Umakoshi et al. 2001) that was interpreted as magma migrating obliquely westward at an angle of ~45° to the horizontal plane from beneath Chijiwa Bay to the summit. Based on GPS and leveling measurements, Kohno et al. (2008) identified four pressure sources, located just beneath the inclined zone of earthquake hypocenters (sources A–D in Fig. 1).

This magmatic pathway was investigated by conducting a seismic survey. A north–south seismic reflection survey across Unzen graben revealed strong reflectors at a depth of 3 km below sea level, which corresponds to 1 km above pressure source B (Fig. 1a and Fig. 8a; Matsumoto et al. 2012). The reflectors are interpreted as the top of the magmatic chamber. However, this interpretation is based solely on reflector geometry. To better understand and estimate

*Correspondence: agnis@sevo.kyushu-u.ac.jp

¹ Department of Earth and Planetary Sciences, Graduate School of Science, Kyushu University, Fukuoka, Japan

Full list of author information is available at the end of the article



the physical properties of the subsurface structure, other types of geophysical analysis are required.

Electrical resistivity structure provides useful information on volcanoes, because it is highly sensitive to magma, hydrothermal fluids, and hydrothermally altered clay minerals (e.g., Nurhasan et al. 2006; Aizawa et al. 2009a, b; Bertrand et al. 2012; Hata et al. 2016; Seki et al. 2016). The resistivity structure of Unzen volcano has been previously estimated using magnetotelluric (MT) analysis and time-domain electromagnetic (TDEM) methods (Kagiyama et al. 1999; Komori et al. 2013; Srigutomo et al. 2008). Using 1-D analysis, Kagiyama et al. (1999) suggested the presence of shallow groundwater and deep magma and assessed magma–groundwater interaction during the 1990–1995 eruptions. Srigutomo et al. (2008) used 1-D analysis to suggest that volcanic gases are being supplied to a water-rich layer through a system of faults. Using 2-D modeling, Komori et al.

(2013) imaged a relatively resistive region beneath the younger lava domes and surrounding conductive zones. By comparing the model with scientific drilling data, they concluded that the conductive hydrothermal zone played an important role in heat and mass transfer within the Unzen magmatic system. These previous studies highlighted the importance of the shallow conductive hydrothermal zone in terms of volcanic activity. However, data from these surveys were processed using 1-D and 2-D inversions and were not sensitive to deeper structure beneath the hydrothermal zone. Furthermore, the site distribution in these studies was too sparse to investigate finer structures such as faults and conduits. To address these shortcomings, we performed a broadband MT survey along the same line as the seismic reflection survey by Matsumoto et al. (2012). Although the MT data were obtained along a single profile, we performed 3-D inversion and considered topography because of strong 3-D

features in the MT data and steep topography. Then, we compared the resistivity profile with the seismic reflection profile of Matsumoto et al. (2012). Although MT and seismic reflections have been jointly interpreted in tectonically active or volcanic regions (e.g., Unsworth et al. 1997; Brasse et al. 2002; Comeau et al. 2016), correlating resistivity structure with a seismic reflection profile at fine spatial resolution is rare, especially at shallow levels beneath a volcano. We show how these two physical properties correlate with each other and discuss the relationships between magma, faults, and hydrothermal systems.

Geological setting

In Unzen graben, many east–west normal faults have developed under north–south tensile stress (Fig. 1). Our MT survey line intersects the Chijiwa Fault (CF), the Kusenbu Fault (KF), and the Oshidorino-Ike Fault (OF), as well as three minor unnamed faults (Matsuoka et al. 2005; Tsutsumi 1987, 2015). The CF, located near the northern boundary of the graben, is the longest (19 km at the surface) and the most active fault in this region. The average displacement rate at the surface is estimated to range from 2.8 m/ka in the east to 8.8 m/ka in the west, with total surface displacement ranging from 38 m (east) to 180 m (west). Two other major faults (KF and OF) are located in the graben, with respective surface lengths of 5.0–8.5 km and average surface displacement rates of 0.5–4.0 m/ka, respectively (Matsuoka et al. 2005; Tsutsumi 1987). The graben is thought to extend to a depth of 1 km b.s.l. and is filled with volcanic products (Hoshizumi et al. 1999). The basement of the graben is mainly high-density rock, interpreted as Paleogene sediments. Approximately 2 km to the east of the profile, lava domes associated with the younger stages of the Unzen complex (Nodake and Myokendake) and currently active regions (Fugendake and Heisei Shinzan) are exposed (Fig. 1b). The line of the MT profile spans relatively old (300–150 ka) volcanic products.

Broadband MT survey

Magnetotellurics is a passive electromagnetic geophysical method that measures temporal variations in induced natural electromagnetic fields on the Earth's surface to derive the subsurface resistivity structure. We conducted an MT survey along an approximately 9-km-long north–south profile (Fig. 1b, Additional file 1: Figure S1). Measurement sites were located along the same profile as the seismic reflection survey by Matsumoto et al. (2012). To image detailed structures, our stations were closely spaced at 300–400-m intervals. The survey consisted of 23 telluric sites recording only electric field variations and 4 MT sites recording both electric and magnetic field

variations. At each MT site, a Metronix ADU07e logger was connected to three induction coils and five electrodes (one of which was used as a common ground) to measure the magnetic and electric fields, respectively. At telluric sites, electric fields (E_x and E_y) were recorded using ELOG1 K loggers (NT System Design). Observations were conducted between April 25 and May 8, 2018. The typical recording duration at a given site was 7–10 days. The sampling frequencies were 32 Hz (00:00–23:50 UT) and 1024 Hz (17:00–18:00 UT).

Data processing

After data collection, the binary time series data were converted to text format time series data with physical units (mV/km and nT) using the frequency responses of induction coils and data loggers, and the dipole length of the electric field. Because the time series data were affected by cultural noise from a 60 Hz power line, we performed notch filtering to eliminate 60 Hz noise and its associated odd-order overtones (Aizawa et al. 2013). Next, we calculated the MT response function over a 0.003–3276.8-s period range using a bounded influence remote reference code (Chave and Thomson 2004). At sites where only telluric measurements were undertaken, we used the magnetic data of the nearest MT site (e.g., Munoz and Ritter 2013; Comeau et al. 2018; Tsukamoto et al. 2018). We confirmed that the use of different magnetic sites did not cause significant differences in the response functions. To obtain unbiased impedance, remote reference processing was performed by canceling incoherent noise between an observation site and a reference site (Gamble et al. 1979). As a reference magnetic site, we used data from the MT monitoring station at Iwo-Yama, located in the Kirishima Volcanic Complex (Aizawa et al. 2013). Although data quality over shorter periods was successfully improved, the data show significant scatter at periods greater than 10 s. By visual inspection, we excluded outliers from the smoothed sounding curve. We also discarded a site located near a metal fence, as its impedance curves show unrealistic values. Phase tensor analysis (Caldwell et al. 2004) shows the variable orientations of the major axes of ellipses and large $|\beta|$ (Fig. 2), and the diagonal components of impedances dominate the off-diagonal components for longer periods (Additional file 2: Figure S2), all indicating 3-D structure in this region.

2-D and 3-D inversions

Before 3-D inversion, we conducted 2-D inversion using the code of Ogawa and Uchida (1996), employing only the Z_{xy} impedances. The regional strike of the area has roughly E–W orientation according to geological evidence (i.e., graben and surface fault traces, such

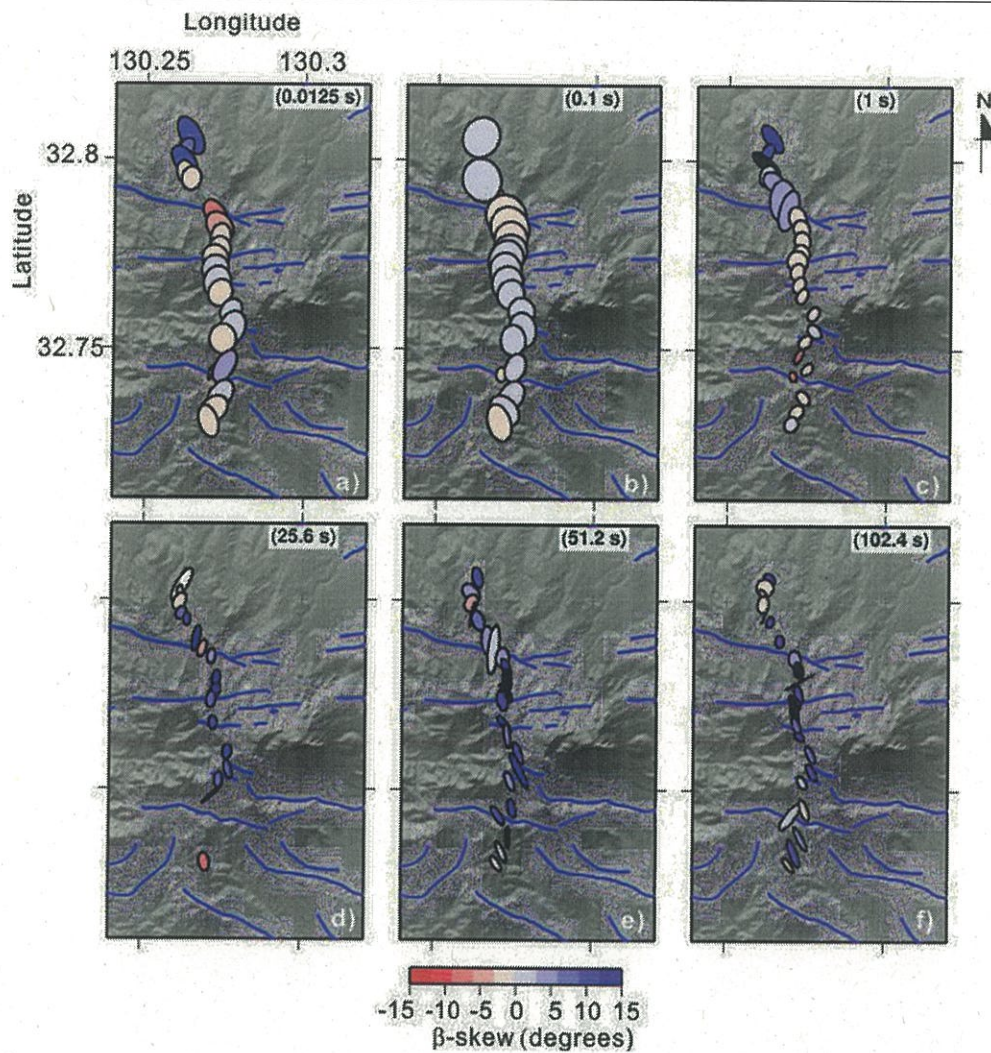


Fig. 2 Phase tensor ellipse (Caldwell et al. 2004) maps for different sounding periods (0.00125 s, 0.1 s, 1 s, 25.6 s, 51.2 s, 102.4 s). Color-filled ellipses represent the phase tensor ellipse with its orientation derived from azimuth $\alpha - \beta$. The color indicates β skew angle. The sites having very large error bars (outliers) at the corresponding periods are removed. Site dependent of orientation strongly indicate 3-D behavior

as Chijiwa Fault) (i.e., Hoshizumi et al. 1999). On the assumption that the 2-D strike is the same as the surface traces of faults, Z_{xy} corresponds to the transverse magnetic (TM) mode (electric current crosses the strike), while Z_{yx} corresponds to the transverse electric (TE) mode (electric current flows along the strike). In this study, we used TM mode data, which is sensitive to lateral discontinuities of the structure and is relatively insensitive to the 3-D structure (e.g., Siripunvaraporn et al. 2005a).

We selected TM mode data of 20 periods (0.004–204.8 s) and manually eliminated several outliers, particularly at periods > 12.8 s. In the 2-D inversion, we

take into account that the Z_{xy} at telluric sites are calculated using magnetic fields at different sites. The apparent resistivity of the initial model is 100 Ω m with an error floor of 10%. Then, the final model was arrived at after 17 iterations. The RMS was 0.75. Figure 5a shows the best-fit 2-D structure.

In the case of strong 3-D features, 3-D inversion usually produces more reliable resistivity structures than 2-D inversion. The merits of applying 3-D inversion to single MT profile were first demonstrated by Siripunvaraporn et al. (2005a) using synthetic data. This procedure was consequently applied to real field data by Patro and Egbert (2011), Bertrand et al. (2013), Brasse et al. (2015),

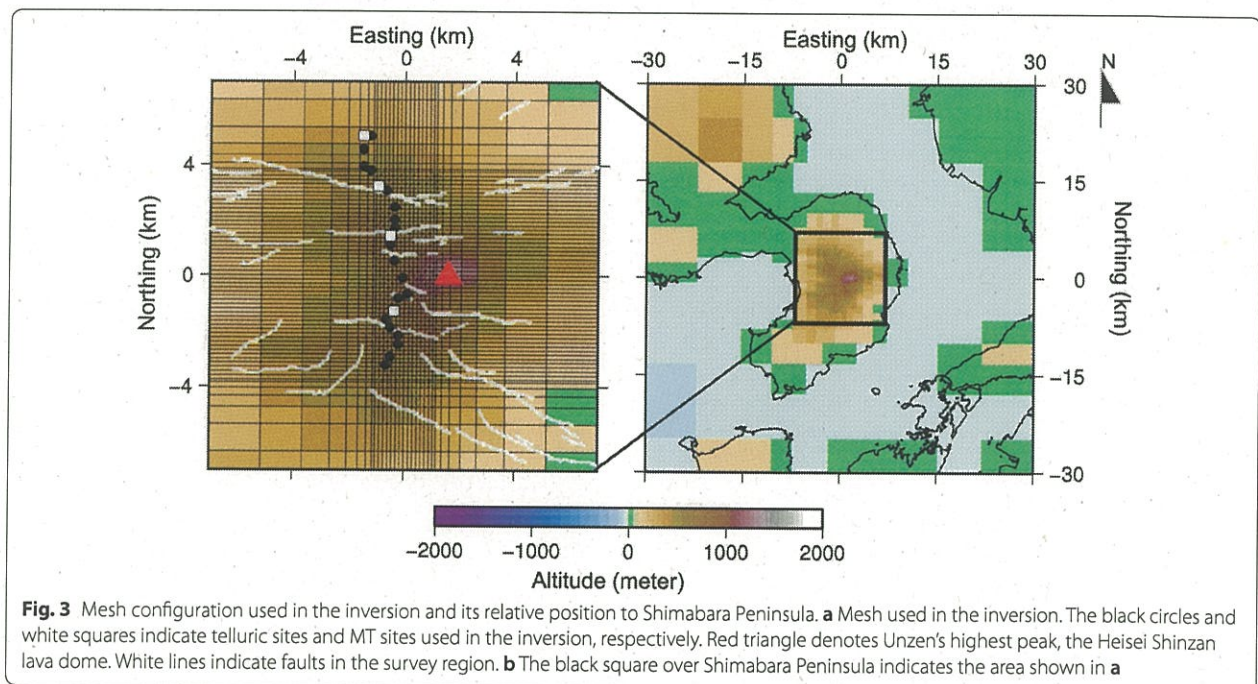
and Beka et al. (2016), and artifact structure produced in 2-D inversion can be eliminated in 3-D scheme. We performed 3-D inversion using the WSINV3DMT code, which is based on the data-space variant of Occam's 3-D inversion scheme (Siripunvaraporn et al. 2005a, b; Siripunvaraporn and Egbert 2009).

We inverted both the impedance tensor (Z_{xx} , Z_{xy} , Z_{yx} , and Z_{yy}) and the geomagnetic transfer function (T_{zx} and T_{zy}). Initially, we picked data from a total of 16 periods between 0.004 and 3277 s at all stations. However, for several sites, considering data quality at the shortest and longest periods, we used the data from 0.0125 to 1638.4 s. In the initial model, the horizontal mesh size was 150 m close to the profile, increasing logarithmically with increasing distance from the profile. Topographic effects can interrupt the MT transfer function, driven by charge accumulation on slopes, especially in the case of a mountainous survey region (e.g., Usui 2015; Käufel et al. 2018). To reduce this effect, we included topography in the inversion by adding 100-m vertical mesh data from sea level to the highest point at 1700 m above sea level. The model consisted of 47 layers in the z direction (including seven air layers), and 76 and 42 blocks in the x and y directions, respectively (Fig. 3). The half-space resistivity was initially set to 100 Ωm , and the resistivity of air and sea was fixed at $10^7 \Omega\text{m}$ and 0.25 Ωm , respectively. We tested a starting model with values of 1000 Ωm and 10 Ωm ; however, the RMS of each iteration always exceeded the 100 Ωm resistivity.

Errors in impedance and geomagnetic transfer functions were set to 10%. Initially, 10 iterations were performed. After checking the RMS of each model, we re-inverted the data using the model with lowest RMS as the initial model for the second inversion. Previous MT 3-D studies (e.g., Patro and Egbert 2011; Comeau et al. 2016; Azeez et al. 2018) have also employed a similar approach to achieve better fitting result. As a result, RMS decreased significantly from 6.13 in the initial model of the first inversion to 1.60 in the final model of the second inversion. Figures 4 and 5 show horizontal and vertical slices of the final 3-D resistivity structure, respectively. Figure 6 shows the comparison of the observed data with the calculated data from the final resistivity structure.

The 2-D and 3-D models along the survey line are moderately similar (Fig. 5a, b). Both models show the first resistive layer is on top of the conductive layer, and the third layer displays high resistivity. However, significant differences are found at a depth of the third layer. Two conductive bodies in the 2-D model (black dashed lines in Fig. 5a) are not apparent in the 3-D model. The discrepancy between the models probably arose because of the 2-D modeling that was applied to a natural 3-D structure (Siripunvaraporn et al. 2005a; Brasse et al. 2015), especially for longer-period data. Thus, in this study, we focus on the 3-D structure.

The 3-D final resistivity structure essentially consists of three layers: a highly resistive layer (RL1) at the surface, a moderately conductive zone (CL1) beneath RL1 to a



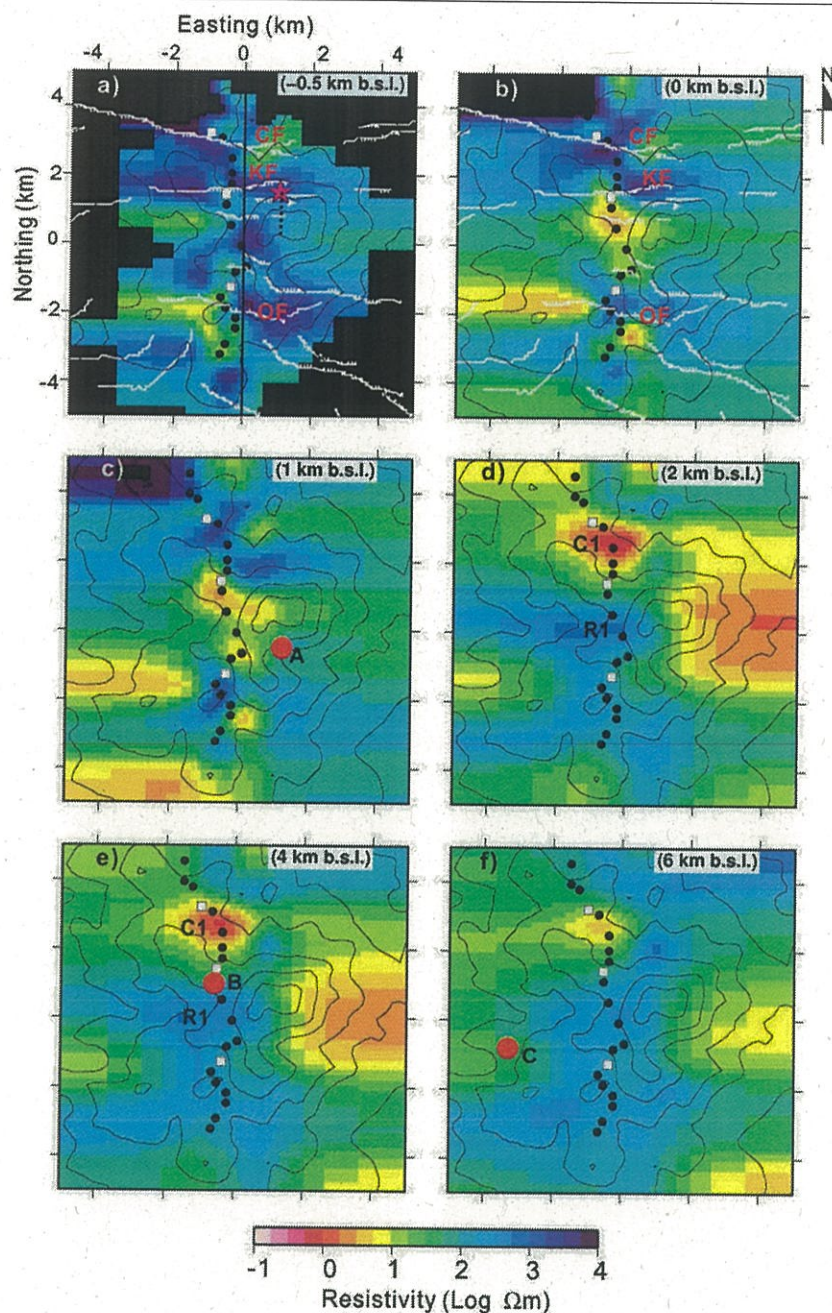
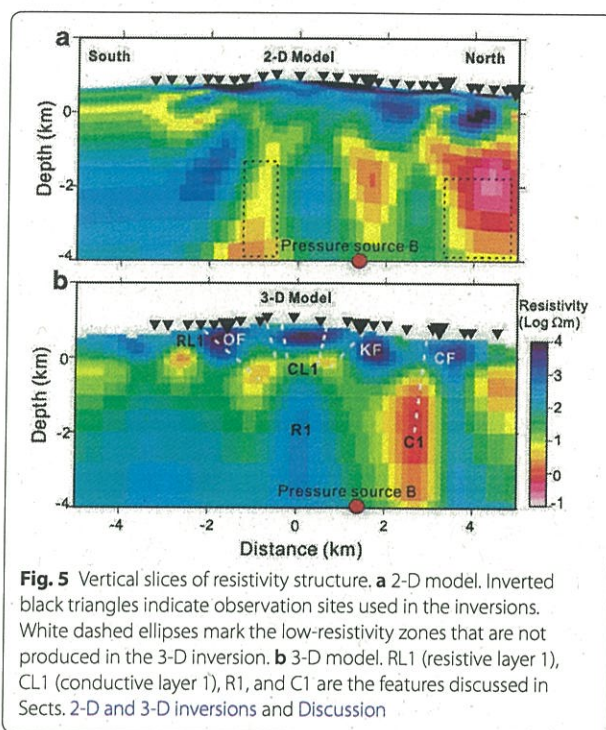


Fig. 4 Horizontal slices of the final 3-D resistivity structure at various depths below sea level (b.s.l.). Topographic contour interval is 200 m. Details are as in Fig. 2. The distinctive structures C1 and R1 are labeled. White lines show faults in the survey region (CF Chijiwa Fault, KF Kusenbu Fault, OF Oshidoro-Ike Fault), while red dots represent pressure sources identified by Kohno et al. (2008). The black line in the center of the top left panel marks the north-south cross section shown in Fig. 5b and 8b. The purple star and dashed black line indicate the USDP-4 drilling location and its subsurface trajectory. Note that the structure away from the profile is not constrained (for example, the sensitivity tests around pressure sources A and C show the small difference in RMS)

depth of ~1 km, and an underlying resistive zone. Within this structure, we noted two anomalies: a distinctive conductive body (C1) in the northern part of the survey

area, below sea level; and a vertically oriented resistive body (R1) in the center of transect. Before interpreting these structures, we conducted sensitivity tests to assess



the robustness of C1 and R1 within the model. Figure 7 shows the sounding curves of selected sites after sensitivity testing. After replacing C1 with a zone of 100 Ωm resistivity and performing a forward calculation, model RMS increased from 1.60 to 3.20. Replacing R1 with a 10 Ωm resistivity zone resulted in an RMS increase from 1.60 to 1.70. These RMS changes indicate that C1 is better constrained than R1. We did the replacement also in the southern extension of C1, the result of which is shown in Additional file 3: Figure S3. It raised the RMS to 1.67. The weaker constraint on R1 arose because the MT method is more sensitive to a conductive zone than a resistive zone. However, the small RMS increase observed in the sensitivity test of R1 suggests that this body is not a ghost structure.

Discussion

Upper resistive layer (RL1)

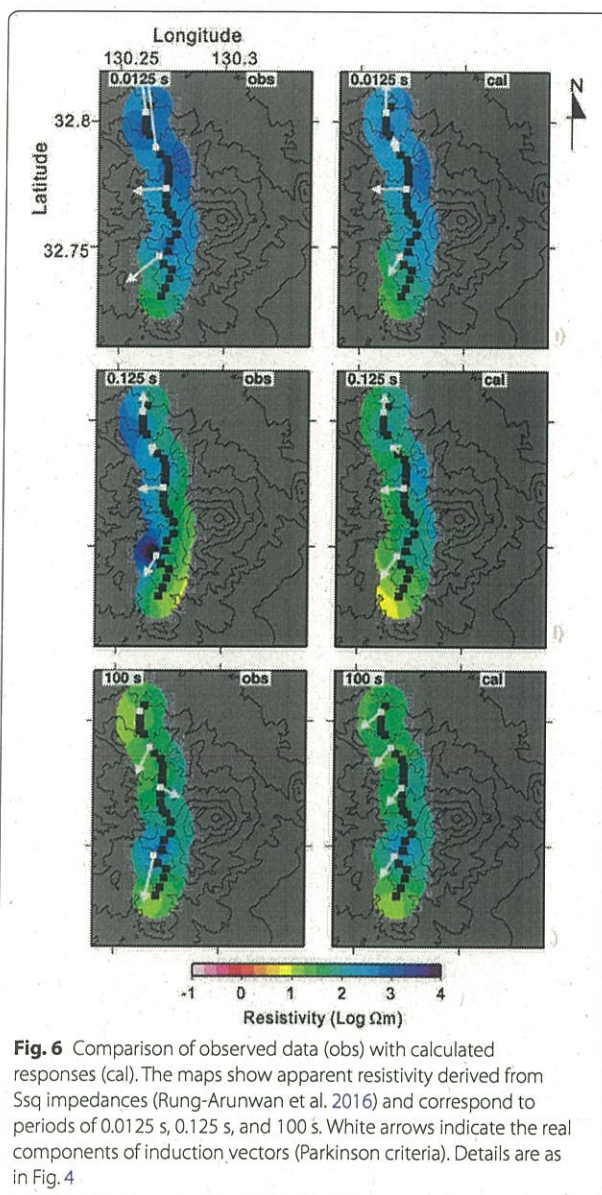
The upper resistive layer (RL1) extends from the surface to several hundred meters beneath sea level, corresponding to the estimated depth of high-density and highly magnetized formations that fill the graben (Inoue 2013; Okubo et al. 2006). The present survey line is largely covered by older Unzen lava and pyroclastic products from eruptions during the period 300–150 ka, which appear to be highly resistive (Matsumoto et al. 2012, after Hoshizumi et al. 2003). We interpret RL1 as a cold groundwater zone (meteoric water). Although the sampling points

are limited in the area east of the Unzen volcano, the resistivity of cold groundwater at the mid-flank shows the resistivity of approximately 50–100 Ωm (Shimano 1999). The high resistivity of value RL1 is likely due to the water, considering the realistic porosity and Archie's law. In particular, the shallowest part is interpreted as an unsaturated groundwater zone, beneath which a cold aquifer occurs. A dominant feature of RL1 is that this high-resistivity zone (several 1000 Ωm) is dissected by faults characterized by relatively conductive regions (several 100 Ωm ; Fig. 4b, 5b, 8b). Note that the faults might be inclined rather than vertical. Previous MT studies attributed the high conductivity of shallow fault-related zones to the presence of clay minerals, high fracture density, and well-developed fluid networks (e.g., Karas et al. 2017; Unsworth and Bedrosian 2004; Yamaguchi et al. 2010). It should be noted that because faults are usually characterized by thin planes, they are difficult to image using MT. The previous studies suggested that instead of imaging the actual fault planes, the MT technique images the relatively thick fractured or altered zones surrounding the faults. We suggest that relatively conductive zone around faults in RL1 represents a dense fracture network in which cold meteoric groundwater accumulates before flowing downward.

Middle conductive layer (CL1)

Beneath RL1, at ~0–2 km beneath sea level, a conductive layer (<50 Ωm CL1) is identified. We interpret CL1 as a hot, groundwater-rich layer characterized by hydrothermal alteration, as also indicated by previous studies. Density and magnetization distributions show that CL1 is correlated with hydrothermally altered Neogene rock characterized by low magnetization (1 A/m) and high density (Inoue 2013; Okubo et al. 2006).

CL1 contains a relatively low-resistivity zone; in particular, beneath the CF, a zone of low resistivity (<10 Ωm) extends to greater depth. This conductor is separately referred to as C1 and discussed below. Conductive zones underlying faults have been reported previously and are interpreted as fractured regions that are rich in crustal fluids (Becken and Ritter 2012; Karas et al. 2017; Kaya et al. 2013; Xiao et al. 2017; Azeez et al. 2018). Considering the relatively conductive zone found beneath the faults at the same depth as RL1, as well as identification of fault planes in the seismic reflection profile (Fig. 8b), we interpret this region as a deeper extension of the fracture zone, given that fault zones are relatively conductive. In Figs. 5b and 8b, the white dashed line indicates the fractured zones associated with the fault inferred from the location of relatively conductive zones at the depth of RL1 and CL1.



Broad, highly conductive body (C1)

C1 is the dominant feature of the resistivity structure. The upper part of C1, approximately at the depth 500–700 m below sea level, corresponds to CL1. Although we could not examine the off-profile extension of C1, it is located near the CF (Chijiwa Fault) and pressure source B by Kohno et al. (2008). Some MT studies have suggested that a dominant conductive body can be interpreted as a magmatic body (e.g., Diaz et al. 2015; Hill et al. 2015; Hata et al. 2016; Brasse et al. 2015; Comeau et al. 2016; Cordell et al. 2018), but C1 is too large and shallow to represent a magma reservoir. C1 occupies a

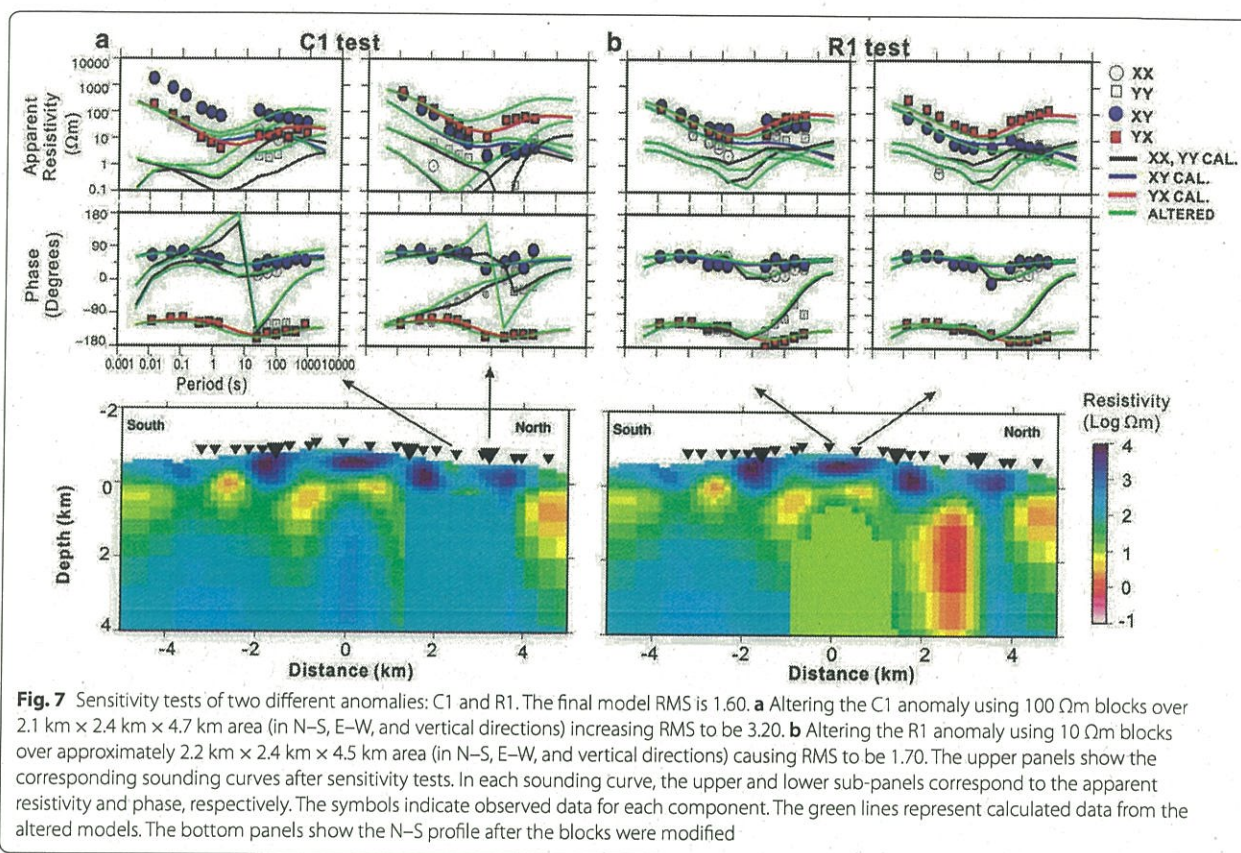
volume of $\sim 10 \text{ km}^3$, compared with 0.2 km^3 of magma erupted during the period 1991–1995 (Nakada and Motomura 1999). The lack of geothermal activity above C1 is also inconsistent with the interpretation of C1 as a magma reservoir. According to Kohno et al. (2008), pressure source B is located $\sim 4 \text{ km}$ beneath sea level. If C1 represents a volume of interconnected melt, the pressure source would be observed at the top of C1, as a result of its buoyancy, rather than far beneath the top of C1. In this study, we interpret C1 as an interconnected fracture network around the CF, to which volatiles are supplied from pressure source B.

It is commonly thought that faults act as pathways for volatiles (e.g., Becken et al. 2011; Becken and Ritter 2012; Ichihara et al. 2011; Aizawa et al. 2016). The eruptions of Unzen volcano during 1991–1995 were effusive (i.e., mild) and were considered to have resulted from effective degassing during magma ascent. The degassing might have been maintained by volcanic gas discharge along many E–W trending faults (e.g., Komori et al. 2014), especially along the Chijiwa Fault, which is the longest and most active fault in Unzen graben. Indeed, ground-water gas analysis around Unzen volcano suggests that the CF provides a surface escape route for magmatic CO_2 (Ohsawa et al. 2002).

C1 extends to a greater depth than the conductive zones beneath other faults, and the resistivity of C1 is lower than that of the zones beneath other faults. Given that C1 is interpreted to have originated by fracturing related to fault activity, it is possible that earthquakes have occurred repeatedly on the Chijiwa Fault.

Vertical resistive body (R1)

A comparison of the seismic reflection profile and the resistivity structure reveals a correlation between the sub-vertical high-resistivity zone (R1) and a narrow vertical zone of low reflectivity in the center of the survey line (Fig. 8). We interpret R1 as a cooled conduit through which dykes intruded to approach the summit. This interpretation is consistent with that of Matsumoto et al. (2012). The scientific drilling at site USDP4 (1.5 km east of the MT profile) revealed relatively high resistivity ($\sim 100 \Omega\text{m}$), low porosity (< 0.25), and high density (2.5 g/cm^3) within the conduit due to the presence of solidified dykes related to eruptions of various ages (Ikeda et al. 2008; Sakuma et al. 2008). The presence of consolidated magma, low porosity, and/or high-density rocks are all plausible explanations of the high resistivity. Many MT studies have made similar interpretations of high-resistivity zones (e.g., Aizawa et al. 2008, 2009b, 2014; Diaz et al. 2015; Bedrosian et al. 2018). The result of the scientific drilling supports our interpretation of R1.

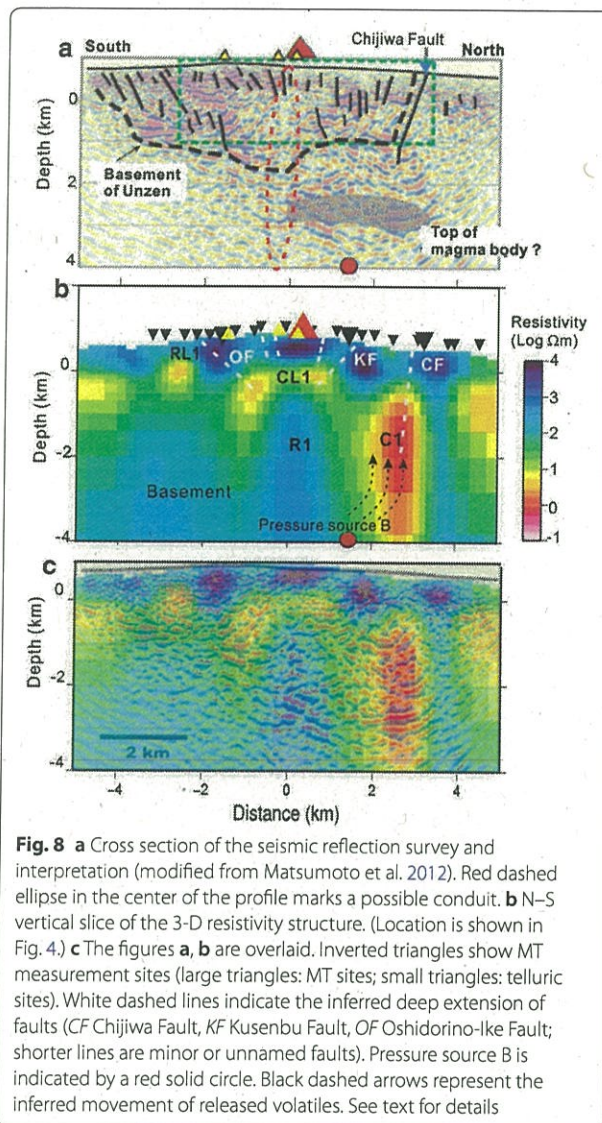


Although it is not confirmed that R1 is related to the latest (1990–1995) eruptions, the 500-m horizontal width of dykes confirmed by the drilling study is consistent with the horizontal extent of R1. The drilled conduit consists of multiple dykes and veins from various eruption stages, and the widths of individual dikes are up to 40 m. The dikes in the deepest part of the drill hole (~ 100 m below sea level) are believed to represent the most recent conduit, as inferred from petrological analysis, and these rocks cooled to < 200 $^{\circ}\text{C}$ within nine years after the eruptions (Nakada et al. 2005; Ikeda et al. 2008). Hydrothermal fluid circulation was determined to be the most likely cause of cooling (Fujimitsu et al. 2008). The moderately conductive layer CL1 and highly conductive body C1 in this study, interpreted as hydrothermal-water-rich layers, may be responsible for cooling the conduit (R1).

Relationship between resistivity and seismic reflection

A comparison of the resistivity structure with the seismic reflection profile of Matsumoto et al. (2012) revealed that RL1, CL1, and C1 correlate with areas of strong seismic reflectivity (Fig. 8). On the other hand, the resistive zone beneath CL1 is imaged as zones of weak reflectivity. On the basis of these spatial

correlations and the interpretations in Sects. Upper resistive layer (RL1)–Vertical resistive body (R1), we suggest that an interconnected pore network controls the relationship between electric resistivity and seismic reflectivity. Several qualitative interpretations have been made. Joint interpretation of MT and seismic data suggests that fluid-rich zones are indicative of high porosity with good connectivity and are electrically conductive (Hyndman and Shearer 1989; Jones 1987; Unsworth et al. 1997; Yan et al. 2016). Differences in porosity may create large contrasts in elastic properties, thus enhancing reflectivity in areas of high porosity. The multilayered structures characteristics of volcanic deposits may also contribute to high seismic reflectivity since it has high porosity, such as found in RL1. CL1 and C1 are also interpreted as hydrothermal-water-rich zones marked by high porosity and maintained interconnectivity. Consequently, both of these areas show strong reflectivity. In contrast, the resistive zone beneath CL1, which might correspond to the basement of Unzen volcano, is interpreted as a zone of low porosity and consequently shows weak reflectivity. Similar relationships between resistivity data and seismic profiles, and comparable interpretations, have been



reported for paleo-magmatism in Sweden (Hubert et al. 2013; Yan et al. 2016).

The estimated dip, depth extent, and the number of faults detected in this study differ slightly from those estimated by Matsumoto et al. (2012). For example, the KF is imaged as sub-vertical in the seismic reflection profile, whereas the MT model suggests it dips toward the south. Seismic profiles show offsets in reflection patterns, allowing fault planes to be identified by their displacement (e.g., Matsumoto et al. 2012). In contrast, MT cannot image fault planes but can identify voluminous fracture zones (e.g., Unsworth and Bedrosian 2004; Yamaguchi et al. 2010; Karas et al. 2017). It is

possible that fault planes and their associated fractured zones have different dip angles.

Conclusion

The resistivity structure beneath our survey line basically shows three-layer structure. The first layer is near-surface high-resistivity zone that corresponds to a zone of cold groundwater with old Unzen deposits. This layer is cut by four faults. The second layer is the mid-conductive layer associated with hydrothermal zone which shows relatively conductive values near the faults. The third layer is a bottom resistive zone related to the basement of the Unzen graben. At the same depth as the third layer, we found two distinctive anomalies. One is a highly conductive zone (C1) beneath Chijiwa Fault. Another is highly resistive zone R1 in the center of profile. C1 is interpreted as zone of interconnected fracture network around Chijiwa Fault, to which volcanic fluids are supplied from deeper pressure source (B). Given that C1 extends to a greater depth than the conductive zones beneath other faults, and its resistivity is lower than that of other zones, it is possible that earthquakes have occurred repeatedly on the Chijiwa Fault. R1 is interpreted as the cooled conduit of Unzen volcanism and consists of lava dykes and veins related to eruptions of various ages. Based on the correlation between the resistivity and seismic reflection structures, we conclude that the interconnected pore network controls the relationship between resistivity and reflections.

Additional files

Additional file 1. Figure S1. MT station and corresponding names. The subsequent sounding curves are shown in Additional file 2: Figure S2. MT station and Telluric station are denoted as white rectangle and black rectangle respectively. The 'SITE X' is the site being excluded in the inversion. The red triangle shows Heisei Shinzan lava dome.

Additional file 2. Figure S2. Sounding curve of apparent resistivity (upper part, in Ωm) and phase (lower part, in degree) to the corresponding periods (in second) from all stations used in the 3-D inversion. (a) Sites numbered 1 to 12 and (b) sites numbered 13 to 25. The location of each station is explained in Additional file 1: Figure S1. Symbols and lines are detailed in the legend.

Additional file 3. Figure S3. Sensitivity test of the southern extension of C1 anomaly by changing the resistivity of the area with 100 Ωm blocks. The altered zone extends to 2.4 km in E-W direction and 4.7 km in vertical direction. The RMS of modified model is 1.67 from initially 1.60. Small increase in the RMS indicates that the width of C1 is less constrained. The upper and bottom panel as well as symbols and legends are same as Fig. 7.

Authors' contributions

AT, KA, and YT designed the field survey. AT carried out the analysis and drafted the manuscript. All authors contributed to MT data acquisition and discussion. All authors read and approved the final manuscript.

Author details

¹ Department of Earth and Planetary Sciences, Graduate School of Science, Kyushu University, Fukuoka, Japan. ² Institute of Seismology and Volcanology, Faculty of Science, Kyushu University, 744 Motoooka, Nishi-ku, Fukuoka 819-0395, Japan. ³ Japan Meteorological Agency, 4-1 Korimoto, Kagoshima 890-0068, Japan. ⁴ Earthquake Research Institute, University of Tokyo, Yayoi 1-1-1, Bunkyo-ku, Tokyo 113-0032, Japan.

Acknowledgements

We thank forestry officers for granting access to conduct field campaigns. We appreciate S. Matsumoto and H. Shimizu for extensive discussions and suggestions while interpreting the results. We appreciate H. Tsutsumi, M. Ueda, and Geospatial Information Authority of Japan for supplying the fault data. SEVO students Y. Hayashida, K. Takeishi, Y. Yuasa, S. Watanabe, and Y. Odasaki are thanked for their help with the MT survey. Our gratitude goes to Y. Ogawa for supplying 2-D inversion code and W. Siripunvaraporn for supplying his 3-D inversion code. We used the computer systems of the Earthquake and Volcano Information Center of the Earthquake Research Institute, the University of Tokyo. Comments from two anonymous reviewers were helpful in improving the manuscript. This study was supported by the Ministry of Education, Culture, Sports, Science and Technology (MEXT) of Japan, under its Earthquake and Volcano Hazards Observation and Research Program, and funded by JSPS KAKENHI (JP15K17751). AT sincerely thanks the LPDP Scholarship (Indonesian Education Scholarship) for funding her education at Kyushu University.

Competing interests

The authors declare that they have no competing interests.

Availability of data and materials

The datasets are available from the corresponding author AT on reasonable request.

Consent for publication

Not applicable.

Ethics approval and consent to participate

Not applicable.

Funding

This study was supported by the Ministry of Education, Culture, Sports, Science and Technology (MEXT) of Japan, under its Earthquake and Volcano Hazards Observation and Research Program and KAKENHI (Grant No. 15K17751). AT sincerely thanks the LPDP Scholarship (Indonesian Education Scholarship) for funding her education at Kyushu University.

Publisher's Note

Springer Nature remains neutral with regard to jurisdictional claims in published maps and institutional affiliations.

Received: 13 October 2018 Accepted: 18 February 2019

Published online: 04 March 2019

References

- Aizawa K, Ogawa Y, Hashimoto T, Koyama T, Kanda W, Yamaya Y, Mishina M, Kagiyama T (2008) Shallow resistivity structure of Asama Volcano and its implications for magma ascent process in the 2004 eruption. *J Volcanol Geotherm Res* 173(3–4):165–177. <https://doi.org/10.1016/j.jvolgeores.2008.01.016>
- Aizawa K, Ogawa Y, Ishido T (2009a) Groundwater flow and hydrothermal systems within volcanic edifices: delineation by electric self-potential and magnetotellurics. *J Geophys Res Solid Earth*. <https://doi.org/10.1029/2008jb005910>
- Aizawa K, Ogawa Y, Mishina M, Takahashi K, Nagaoka S, Takagi N, Sakanaka S, Miura T (2009b) Structural controls on the 1998 volcanic unrest at Iwate volcano: relationship between a shallow, electrically resistive body and the possible ascent route of magmatic fluid. *J Volcanol Geotherm Res* 187(1–2):131–139. <https://doi.org/10.1016/j.jvolgeores.2009.08.009>
- Aizawa K, Koyama T, Uyeshima M, Hase H, Hashimoto T, Kanda W, Yoshimura R, Utsugi M, Ogawa Y, Yamazaki K (2013) Magnetotelluric and temperature monitoring after the 2011 sub-Plinian eruptions of Shinmoe-dake volcano. *Earth Planets Space* 65:539–550. <https://doi.org/10.5047/eps.2013.05.008>
- Aizawa K, Koyama T, Hase H, Uyeshima M, Knada W, Utsugi M, Yoshimura R, Yamaya Y, Hashimoto T, Yamazaki K, Komatsu S, Watanabe A, Miyakawa K, Ogawa Y (2014) Three-dimensional resistivity structure and magma plumbing system of the Kirishima Volcanoes as inferred from broadband magnetotelluric data. *J Geophys Res Solid Earth* 119:198–215. <https://doi.org/10.1002/2013JB010682>
- Aizawa K, Sumini H, Uyeshima M, Yamaya Y, Hase H, Takahashi HA, Takahashi M, Kazahaya K, Ohno M, Rung-Arunwan T, Ogawa Y (2016) Gas pathways and remotely triggered earthquakes beneath Mt. Fuji, Japan. *Geology* 44:127–130. <https://doi.org/10.1130/g37313.1>
- Azeez KKA, Mohanb K, Veeraswamy K, Rastogib BK, Gupta AK, Harinarayana T (2018) 3D crustal resistivity structure beneath the Wagad aftershock zone of the 2001 Bhuj earthquake, Kutch, India: heterogeneous resistivity structure controlled by widespread fluid infiltration and clues to aftershocks pattern. *Tectonophysics* 747–748:54–67. <https://doi.org/10.1016/j.tecto.2018.09.014>
- Becken M, Ritter O (2012) Magnetotelluric studies at the San Andreas fault zone: implications for the role of fluids. *Surv Geophys* 33(1):65–105. <https://doi.org/10.1007/s10712-011-9144-0>
- Becken M, Ritter O, Bedrosian PA, Weckmann U (2011) Correlation between deep fluids, tremor and creep along the central San Andreas fault. *Nature* 480(7375):87–U248. <https://doi.org/10.1038/nature10609>
- Bedrosian PA, Peacock JR, Bowles-Martinez Schultz A, Hill GJ (2018) Crustal inheritance and top-down control on arc magmatism at Mount St Helens. *Nat Geosci* 11:865–870. <https://doi.org/10.1038/s41561-018-0217-2>
- Beka TI, Smirnov M, Birkelund Y, Senger K, Bergh SG (2016) Analysis and 3D inversion of magnetotelluric crooked profile data from central Svalbard for geothermal application. *Tectonophysics* 686:98–115. <https://doi.org/10.1016/j.tecto.2016.07.024>
- Bertrand EA et al (2012) Magnetotelluric imaging of upper-crustal convection plumes beneath the Taupo Volcanic Zone, New Zealand. *Geophys Res Lett* 39:L02304. <https://doi.org/10.1029/2011gl005017>
- Bertrand EA, Caldwell TG, Hill GJ, Bennie SL, Soengkono S (2013) Magnetotelluric imaging of the Ohaaki geothermal system New Zealand: implications for locating basement permeability. *J Volcanol Geotherm Res* 268:36–45
- Brasse H, Lezaeta P, Rath V, Schwabenberg K, Soyer W, Haak V (2002) The Bolivian Altiplano conductivity anomaly. *J Geophys Res* 107:2096. <https://doi.org/10.1029/2001JB000391>
- Brasse H, Schäfer A, Díaz D, Alvarado GE, Muñoz A, Mütschard L (2015) Deep-crustal magma reservoirs beneath the Nicaraguan volcanic arc, revealed by 2-D and semi 3-D inversion of magnetotelluric data. *Phys Earth Planet Inter* 248:55–62. <https://doi.org/10.1016/j.pepi.2015.08.004>
- Caldwell TG, Bibby HM, Brown C (2004) The magnetotelluric phase tensor. *Geophys J Int*. <https://doi.org/10.1111/j.1365-246X.2004.02281.x>
- Chave AD, Thomson DJ (2004) Bounded influence magnetotelluric response function estimation. *Geophys J Int* 157(3):988–1006. <https://doi.org/10.1111/j.1365-246X.2004.02203.x>
- Comeau MJ, Unsworth MJ, Cordell D (2016) New constraints on the magma distribution and composition beneath Volcan Uturuncu and the southern Bolivian Altiplano from magnetotelluric data. *Geosphere*. <https://doi.org/10.1130/ges01277.1>
- Comeau MJ, Kauf J, Becken M, Kuvshinov A, Grayver AV, Kamm J, Demberel S, Sukhbaatar U, Batmagnai E (2018) Evidence for fluid and melt generation in response to an asthenospheric upwelling beneath the Hangai Dome, Mongolia. *Earth Planet Sci Lett* 487:201–209. <https://doi.org/10.1016/j.epsl.2018.02.007>
- Cordell D, Unsworth MJ, Diaz D (2018) Imaging the Laguna del Maule Volcanic Field, central Chile using magnetotellurics: evidence for crustal melt regions laterally-offset from surface vents and lava flows. *Earth Planet Sci Lett* 488:168–180. <https://doi.org/10.1016/j.epsl.2018.01.007>

- Diaz D, Heise W, Zamudio F (2015) Three-dimensional resistivity image of the magmatic system beneath Lastarria volcano and evidence for magmatic intrusion in the back arc (northern Chile). *Geophys Res Lett* 42(13):5212–5218. <https://doi.org/10.1002/2015gl064426>
- Fujimitsu Y, Ehara S, Oki R, Kanou R (2008) Numerical model of the hydrothermal system beneath Unzen Volcano, Japan. *J Volcanol Geotherm Res* 175(1–2):35–44. <https://doi.org/10.1016/j.jvolgeores.2008.03.032>
- Gamble TD, Clarke J, Goubau WM (1979) Magnetotellurics with a remote magnetic reference. *Geophysics* 44(1):53–68
- Hata M, Takakura S, Matsushima N, Hashimoto T, Utsugi M (2016) Crustal magma pathway beneath Aso caldera inferred from three-dimensional electrical resistivity structure. *Geophys Res Lett* 43:10720–10727. <https://doi.org/10.1002/2016gl070315>
- Hill GJ, Bibby HM, Ogawa Y, Wallin EL, Bennie SL, Caldwell TG, Keys H, Bertrand EA, Heise W (2015) Structure of the Tongariro volcanic system: insights from magnetotelluric imaging. *Earth Planet Sci Lett* 432:115–125. <https://doi.org/10.1016/j.epsl.2015.10.003>
- Hoshizumi H, Uto K, Watanabe K (1999) Geology and eruptive history of Unzen volcano, Shimabara Peninsula, Kyushu, SW Japan. *J Volcanol Geotherm Res* 89(1–4):81–94. [https://doi.org/10.1016/s0377-0273\(98\)00125-5](https://doi.org/10.1016/s0377-0273(98)00125-5)
- Hoshizumi H, Uto K, Matsumoto A (2003) Geology and petrology of unzen volcano, field guidebook, A3: unzen and aso volcanoes. XXIII general assembly of the international union on geodesy and geophysics, p 11
- Hubert J, Juanatey MDG, Malehmir A, Tryggvason A, Pedersen LB (2013) The upper crustal 3-D resistivity structure of the Kristineberg area, Skellefte district, northern Sweden revealed by magnetotelluric data. *Geophys J Int* 192(2):500–513. <https://doi.org/10.1093/gji/ggs044>
- Hyndman RD, Shearer PM (1989) Water in the lower continental crust: modeling magnetotelluric and seismic reflection results. *Geophys J Int* 98(2):343–365. <https://doi.org/10.1111/j.1365-246X.1989.tb03357.x>
- Ichihara H et al (2011) A fault-zone conductor beneath a compressional inversion zone, northeastern Honshu, Japan. *Geophys Res Lett*. <https://doi.org/10.1029/2011gl047382>
- Ikeda R, Kajiwaru T, Omura K, Hickman S (2008) Physical rock properties in and around a conduit zone by well-logging in the Unzen Scientific Drilling Project, Japan. *J Volcanol Geotherm Res* 175(1–2):13–19. <https://doi.org/10.1016/j.jvolgeores.2008.03.036>
- Inoue N (2013) Subsurface structure beneath the Unzen Volcano, Shimabara Peninsula, Kyushu, Japan, based on 2D joint inversion of gravity and magnetic data. In: *Proceedings of the 11th SEG international symposium*
- Jones AG (1987) MT and reflection—an essential combination. *Geophys J Roy Astron Soc* 89(1):7–17. <https://doi.org/10.1111/j.1365-246X.1987.tb04380.x>
- Kagiya T, Utada H, Yamamoto T (1999) Magma ascent beneath Unzen Volcano, SW Japan, deduced from the electrical resistivity structure. *J Volcanol Geotherm Res* 89(1–4):35–42
- Karas M, Tank SB, Ozaydin S (2017) Electrical conductivity of a locked fault: investigation of the Ganos segment of the North Anatolian Fault using three-dimensional magnetotellurics. *Earth Planets Space* 69:107. <https://doi.org/10.1186/s40623-017-0695-2>
- Käufel JS, Grayver AV, Kuvshinov AV (2018) Topographic distortions of magnetotelluric transfer functions: a high-resolution 3-D modelling study using real elevation data. *Geophys J Int* 215:1943–1961. <https://doi.org/10.1093/gji/ggy375>
- Kaya T, Kasaya T, Tank SB, Ogawa Y, Tuncer MK, Oshiman N, Honkura Y, Matsushima M (2013) Electrical characterization of the North Anatolian fault zone underneath the Marmara Sea, Turkey by ocean bottom magnetotellurics. *Geophys J Int* 193(2):664–677. <https://doi.org/10.1093/gji/ggt025>
- Kohn Y, Matsushima T, Shimizu H (2008) Pressure sources beneath Unzen Volcano inferred from leveling and GPS data. *J Volcanol Geotherm Res* 175(1–2):100–109. <https://doi.org/10.1016/j.jvolgeores.2008.03.022>
- Komori S, Kagiya T, Utsugi M, Inoue H, Azuhata I (2013) Two-dimensional resistivity structure of Unzen Volcano revealed by AMT and MT surveys. *Earth Planets Space* 65(7):759–766. <https://doi.org/10.5047/eps.2012.10.005>
- Komori S, Kagiya T, Fairley JP (2014) Possibility of effective magma degassing into groundwater flow systems beneath Unzen volcanic area, SW Japan, inferred from the evaluation of volcanic gas fluxes using electrical conductivity structures. *J Volcanol Geotherm Res* 283:73–81. <https://doi.org/10.1016/j.jvolgeores.2014.05.024>
- Matsumoto S, Shimizu H, Onishi M, Uehira K (2012) Seismic reflection survey of the crustal structure beneath Unzen volcano, Kyushu, Japan. *Earth Planets Space* 64(5):405–414. <https://doi.org/10.5047/eps.2011.11.006>
- Matsuoka A, Tsutsumi H, Takemura K, Hoshizumi H, Matsumoto A (2005) Slip rates and late Quaternary activity of the Unzen active faults in western Kyushu. *Acta Fault Res* 25:135–146. https://doi.org/10.11462/afr1985.2005.25_135
- Munoz G, Ritter O (2013) Pseudo-remote reference processing of magnetotelluric data: a fast and efficient data acquisition scheme for local arrays. *Geophys Prospect* 61:300–316. <https://doi.org/10.1111/1365-2478.12012>
- Nakada S, Motomura Y (1999) Petrology of the 1991–1995 eruption at Unzen: effusion pulsation and groundmass crystallization. *J Volcanol Geotherm Res* 89(1–4):173–196. [https://doi.org/10.1016/s0377-0273\(98\)00131-0](https://doi.org/10.1016/s0377-0273(98)00131-0)
- Nakada S, Shimizu H, Ohta K (1999) Overview of the 1990–1995 eruption at Unzen Volcano. *J Volcanol Geotherm Res* 89(1–4):1–22
- Nakada S, Uto K, Sakuma S, Eichelberger JC, Shimizu H (2005) Scientific results of conduit drilling in the Unzen Scientific Drilling Project (USDP). *Sci Drill* 1(5):18–22. <https://doi.org/10.2204/iodp.sd.1.03.2005>
- Nishi K, Ono H, Mori H (1999) Global positioning system measurements of ground deformation caused by magma intrusion and lava discharge: the 1990–1995 eruption at Unzendake volcano, Kyushu, Japan. *J Volcanol Geotherm Res* 89(1–4):23–34. [https://doi.org/10.1016/s0377-0273\(98\)00119-x](https://doi.org/10.1016/s0377-0273(98)00119-x)
- Nurhasan Ogawa Y, Ujihara N, Tank SB, Honkura Y, Onizawa S, Mori T, Makino M (2006) Two electrical conductors beneath Kusatsu-Shirane volcano, Japan, imaged by audiomagnetotellurics, and their implications for the hydrothermal system. *Earth Planets Space* 58(8):1053–1059. <https://doi.org/10.1186/BF03352610>
- Ogawa Y, Uchida T (1996) A two-dimensional magnetotelluric inversion assuming Gaussian static shift. *Geophys J Int* 126(1):69–76. <https://doi.org/10.1111/j.1365-246X.1996.tb05267.x>
- Ohsawa S, Kazahaya K, Yasuhara M, Kono T, Kitaoka K, Yusa Y, Yamaguchi K (2002) Escape of volcanic gas into shallow groundwater systems at Unzen Volcano (Japan): evidence from chemical and stable carbon isotope compositions of dissolved inorganic carbon. *Limnology* 3:169–173. <https://doi.org/10.1007/s102010200>
- Okubo A, Nakatsuka T, Tanaka Y, Kagiya T, Utsugi M (2006) Aeromagnetic constraints on the subsurface structure of the Unzen Graben, Kyushu, Japan. *Earth Planets Space* 58(1):23–31. <https://doi.org/10.1186/BF03351909>
- Patro PK, Egbert GD (2011) Application of 3D inversion to magnetotelluric profile data from the Deccan Volcanic Province of Western India. *Phys Earth Planet Inter* 187(1–2):33–46. <https://doi.org/10.1016/j.pepi.2011.04.005>
- Rung-Arunwan T, Siripunvaraporn W, Utada H (2016) On the Berdichevsky average. *Phys Earth Planet Inter* 253:1–4
- Sakuma S, Kagiya T, Nakada S, Uto K, Shimizu H (2008) Drilling and logging results of USDP-4—penetration into the volcanic conduit of Unzen Volcano, Japan. *J Volcanol Geotherm Res* 175(1–2):1–12. <https://doi.org/10.1016/j.jvolgeores.2008.03.039>
- Seki K et al (2016) Resistivity structure and geochemistry of the Jigokudani Valley hydrothermal system, Mt. Tateyama, Japan. *J Volcanol Geotherm Res* 325:15–26. <https://doi.org/10.1016/j.jvolgeores.2016.06.010>
- Shimano Y (1999) Hydro-chemical study of spring waters at eastern foot of the Unzen volcano, Shimabara peninsula, western Kyushu (in Japanese). *Bunsei Bulletin* 11:3–39
- Siripunvaraporn W, Egbert G (2009) WSNV3DMT: vertical magnetic field transfer function inversion and parallel implementation. *Phys Earth Planet Inter* 173(3–4):317–329. <https://doi.org/10.1016/j.pepi.2009.01.013>
- Siripunvaraporn W, Egbert G, Uyeshima M (2005a) Interpretation of two-dimensional magnetotelluric profile data with three-dimensional inversion: synthetic examples. *Geophys J Int* 160(3):804–814. <https://doi.org/10.1111/j.1365-246X.2005.02527.x>
- Siripunvaraporn W, Egbert G, Lenbury Y, Uyeshima M (2005b) Three-dimensional magnetotelluric inversion: data-space method. *Phys Earth Planet Inter* 150(1–3):3–14. <https://doi.org/10.1016/j.pepi.2004.08.023>
- Srigutomo W, Kagiya T, Kanda W, Munekane H, Hashimoto T, Tanaka Y, Utada H, Utsugi M (2008) Resistivity structure of Unzen Volcano derived from time domain electromagnetic (TDEM) survey. *J Volcanol Geotherm Res* 175(1–2):231–240. <https://doi.org/10.1016/j.jvolgeores.2008.03.033>
- Tsukamoto K, Aizawa K, Chiba K, Kanda W, Uyeshima M, Koyama T, Utsugi M, Seki K, Kishita T (2018) Three-dimensional resistivity structure of

- Iwo-yama volcano, Kirishima Volcanic Complex, Japan: relationship to shallow seismicity, surface uplift, and a small phreatic. *Geophys Res Lett.* <https://doi.org/10.1029/2018gl080202>
- Tsutsumi H (1987) Active faults in Unzen Volcanic Region, Central Kyushu. *Act Fault Res* 4:55–64
- Tsutsumi H. (2015) 1:25,000 active fault map in Unzen faults and its vicinity. Technical report of the Geospatial Information Authority of Japan (D1-No. 739), 13 p
- Umakoshi K, Shimizu H, Matsuwo N (2001) Volcano-tectonic seismicity at Unzen Volcano, Japan 1985–1999. *J Volcanol Geotherm Res* 112(1–4):117–131. [https://doi.org/10.1016/s0377-0273\(01\)00238-4](https://doi.org/10.1016/s0377-0273(01)00238-4)
- Unsworth M, Bedrosian PA (2004) Electrical resistivity structure at the SAFOD site from magnetotelluric exploration. *Geophys Res Lett.* <https://doi.org/10.1029/2003gl019405>
- Unsworth MJ, Malin PE, Egbert GD, Booker JR (1997) Internal structure of the San Andreas fault at Parkfield. *Calif Geol* 25(4):359–362. [https://doi.org/10.1130/0091-7613\(1997\)025%3C0359:SOTSA%3E2.3.CO;2](https://doi.org/10.1130/0091-7613(1997)025%3C0359:SOTSA%3E2.3.CO;2)
- Usui Y (2015) 3-D inversion of magnetotelluric data using unstructured tetrahedral elements: applicability to data affected by topography. *Geophys J Int* 202(2):828–849. <https://doi.org/10.1093/gji/ggv186>
- Xiao QB, Yu G, Jing LZ, Oskin ME, Shao GH (2017) Structure and geometry of the Aksay restraining double bend along the Altyn Tagh Fault, northern Tibet, imaged using magnetotelluric method. *Geophys Res Lett* 44(9):4090–4097. <https://doi.org/10.1002/2017gl072581>
- Yamaguchi S, Ogawa Y, Fuji-ta K, Ujihara N, Inokuchi H, Oshiman N (2010) Audio-frequency magnetotelluric imaging of the Hijima fault, Yamasaki fault system, southwest Japan. *Earth Planets Space* 62(4):401–411. <https://doi.org/10.5047/eps.2009.12.007>
- Yan P, Andersson M, Kalscheuer T, Juanatey MAG, Malehmir A, Shan CL, Pedersen LB, Almqvist BSG (2016) 3D magnetotelluric modelling of the Alno alkaline and carbonatite ring complex, central Sweden. *Tectonophysics* 679:218–234. <https://doi.org/10.1016/j.tecto.2016.05.002>

Submit your manuscript to a SpringerOpen[®] journal and benefit from:

- Convenient online submission
- Rigorous peer review
- Open access: articles freely available online
- High visibility within the field
- Retaining the copyright to your article

Submit your next manuscript at ► [springeropen.com](https://www.springeropen.com)